# The *REQUIEM* Survey I: A Search for Extended Ly–Alpha Nebular Emission Around 31 $z > 5.7$ Quasars.

EMANUELE PAOLO FARINA,[1,2] FABRIZIO ARRIGONI–BATTAIA,[2] TIAGO COSTA,[2] FABIAN WALTER,[1] JOSEPH F. HENNAWI,[1,3]
ANNA–CHRISTINA EILERS,[1] ALYSSA B. DRAKE,[1] ROBERTO DECARLI,[4] THALES A. GUTCKE,[5] CHIARA MAZZUCCHELLI,[6]
MARCEL NEELEMAN,[1] ISKREN GEORGIEV,[1] EDUARDO BAÑADOS,[1] FREDERICK B. DAVIES,[3] XIAOHUI FAN,[7] MASAFUSA ONOUE,[1]
JAN–TORGE SCHINDLER,[1] BRAM P. VENEMANS,[1] FEIGE WANG,[3] JINYI YANG,[7] SEBASTIAN RABIEN,[8] AND LORENZO BUSONI[9]

[1]*Max Planck Institut für Astronomie, Königstuhl 17, D-69117, Heidelberg, Germany*
[2]*Max Planck Institut für Astrophysik, Karl-Schwarzschild-Straße 1, D-85748, Garching bei München, Germany*
[3]*Department of Physics, University of California, Santa Barbara, CA 93106-9530, USA*
[4]*INAF — Osservatorio di Astrofisica e Scienza dello Spazio di Bologna, via Gobetti 93/3, I-40129, Bologna, Italy*
[5]*Max Planck Institut für Astrophysik, Karl–Schwarzschild–Straße 1, D-85748, Garching bei München, Germany*
[6]*European Southern Observatory, Alonso de Córdova 3107, Vitacura, Región Metropolitana, Chile*
[7]*Steward Observatory, University of Arizona, 933 N Cherry Ave, Tucson, AZ 85719, USA*
[8]*Max Planck Institut für Extraterrestrische Physik Gießenbachstraße 1, D-85748, Garching bei München, Germany*
[9]*INAF — Osservatorio Astronomico di Arcetri, Largo Enrico Fermi 5, I-50125, Firenze, Italy*

## ABSTRACT

The discovery of supermassive black holes few hundred megayears after the Big Bang represents a major challenge to our understanding of black holes and galaxy formation and evolution. Their luminosity is produced by extreme gas accretion onto their central black holes, which already reached masses of $M_{\mathrm{BH}} > 10^9 \, \mathrm{M}_\odot$ by $z \sim 6$. Simultaneously, their host galaxies form hundreds of stars per year, using up gas in the process. To understand which environments are able to sustain the rapid formation of these extreme sources we started a *VLT*/MUSE effort aimed at characterizing the surroundings of a sample of $5.7 < z < 6.6$ quasars dubbed: the Reionization Epoch QUasars InvEstigation with MUSE (*REQUIEM*) survey. We here present results of searches for extended Ly$\alpha$ halos around the first 31 targets observed as part of this program. Reaching 5–$\sigma$ surface brightness limits of $0.1 - 1.1 \times 10^{17} \mathrm{erg\,s^{-1}\,cm^{-2}\,arcsec^{-2}}$ over a $1\,\mathrm{arcsec}^2$ aperture we were able to unveil the presence of 12 Ly$\alpha$ nebulae, 8 of which are newly discovered. The detected nebulae show a variety of emission properties and morphologies with luminosities ranging from $8 \times 10^{42}$ to $2 \times 10^{44} \, \mathrm{erg\,s^{-1}}$, FWHMs between 300 and $1700 \, \mathrm{km\,s^{-1}}$, sizes $< 30 \, \mathrm{pkpc}$, and redshifts consistent with those of the quasar host galaxies. As the first statistical and homogeneous investigation of the circum–galactic medium of massive galaxies at the end of the reionization epoch, the *REQUIEM* survey enables the study of the evolution of the cool gas surrounding quasars with cosmic time. A comparison with the extended Ly$\alpha$ emission observed around $z \sim 3$ quasars indicates little variations on the properties of the cool gas surrounding quasars in the first $2 \, \mathrm{Gyr}$ of the Universe.

*Keywords:* cosmology: observations, early universe – quasars: general

## 1. INTRODUCTION

*Where do the first quasars form?* Two decades after the discovery of the first quasar at $z > 6$ (i.e., J1030+0524 at $z = 6.3$, Fan et al. 2001), this question still puzzles astronomers. Assuming a simple model where a massive black hole grows at the Eddington limit starting at a certain time $t_0$ from a seed with mass $M_{\mathrm{BH}}(t_0) = M_{\mathrm{seed}}$, the evolution of

emanuele.paolo.farina@gmail.com

the mass with time can be expressed as:

$$M_{\mathrm{BH}}(t) = M_{\mathrm{seed}} \times \exp \left( f_{\mathrm{Duty}} \frac{1-\eta}{\epsilon} \frac{t - t_0}{t_{\mathrm{Edd}}} \right) \quad (1)$$

where $f_{\mathrm{Duty}}$ is the duty cycle, $\epsilon$ is the radiation efficiency, $\eta$ is the fraction of rest mass energy released during the accretion. The time scale of the mass growth is set by the Eddington time: $t_{\mathrm{Edd}} = \sigma_{\mathrm{T}} c / (4\pi G m_{\mathrm{p}}) = 450 \, \mathrm{Myr}$[1] (Salpeter 1964). In standard radiatively efficient accretion

---

[1] The presence of helium, with a mass of $\sim 4 \times m_{\mathrm{p}}$ and 2 free electrons, allows a faster growth of the black holes. Considering a plasma with abun-

disks, all the energy is radiated away and it is typically assumed that $\epsilon = \eta = 0.1$ (Soltan 1982; Tanaka, & Haiman 2009; Davis & Laor 2011; Davies et al. 2019a). Equation 1 implies that, for instance, a $10^2 \, \mathrm{M_\odot}$ remnant of a PoP III star at $z = 30$ needs to accrete at the Eddington limit for its entire life ($f_{\mathrm{Duty}} = 1$) to reach a black hole mass $> 10^9 \, \mathrm{M_\odot}$ at $z \sim 6$, as observed in quasars (e.g., Mortlock et al. 2011; De Rosa et al. 2011, 2014; Wu et al. 2015; Mazzucchelli et al. 2017; Bañados et al. 2018; Shen et al. 2019; Reed et al. 2019; Pons et al. 2019). In addition, investigations at mm and sub–mm wavelengths revealed that also the host–galaxies of these first quasars are vigorously growing mass, with star formation rates SFR $\gg 100 \, \mathrm{M_\odot} \, \mathrm{yr}^{-1}$ (e.g., Walter et al. 2009; Wang et al. 2013; Willott et al. 2015, 2017; Decarli et al. 2018; Venemans et al. 2012, 2016, 2018; Kim, & Im 2019; Shao et al. 2019; Wang et al. 2019; Yang et al. 2019a).

To comprehend how these first quasars form and grow it is important to understand where they are hosted. Efstathiou, & Rees (1988) first proposed that, in the current ΛCDM paradigm of galaxy formation (e.g., White, & Rees 1978), only rare high peaks in the density field contain enough gas to build–up the black hole and star mass (taking into account mass losses due to supernova–driven winds) of high–redshift quasars. This scenario is supported by cosmological hydrodynamic simulations (e.g., Sijacki et al. 2009; Costa et al. 2014) and analytical arguments (e.g., Volonteri, & Rees 2006) showing that only the small fraction of black holes that, by $z \sim 6$, are hosted by $\gtrsim 10^{12} \, \mathrm{M_\odot}$ dark matter halos can grow efficiently into a population of quasars with masses and accretion rates matching current observational constraints (but see discussion in Fanidakis et al. 2013). To compensate for the rapid gas consumption, the host–galaxies need a continuous replenishment of fresh fuel provided by filamentary streams of $T = 10^4 - 10^5$ K pristine gas from the intergalactic medium (IGM) and/or by mergers with gas rich haloes (e.g., Kereš et al. 2005, 2009; Yoo & Miralda-Escudé 2004; Volonteri & Rees 2005; Volonteri 2010, 2012; Li et al. 2007; Kereš et al. 2009; Dekel, & Birnboim 2006; Dekel et al. 2009; Fumagalli et al. 2011; van de Voort et al. 2012; Di Matteo et al. 2012; Habouzit et al. 2018; Mayer, & Bonoli 2019). Observational validations of this framework can be set by the detection of gas reservoirs and satellites in the so–called circum–galactic medium (CGM, empirically defined as the regions within few hundreds of kiloparsecs from a galaxy) of high–redshift quasars.

Historically, information on the CGM of high–redshift galaxies has been provided by absorption signatures imprinted on background sightlines (e.g., Steidel et al. 1994; Bahcall, & Spitzer 1969; Chen, & Tinker 2008; Chen et

al. 2010a,b; Gauthier et al. 2010; Nielsen et al. 2013a,b; Churchill et al. 2013; Werk et al. 2016; Tumlinson et al. 2017). This technique have been successfully applied up to $z \sim 4$ (a limit set by the rapid drop of the number density of bright background sources) revealing that intermediate redshift quasars are surrounded by massive ($> 10^{10} \, \mathrm{M_\odot}$), metal rich ($Z \gtrsim 0.1 Z_\odot$), and cool ($T \sim 10^4$ K) gas reservoirs (e.g., Bowen et al. 2006; Hennawi et al. 2006; Hennawi, & Prochaska 2007; Decarli et al. 2009; Prochaska, & Hennawi 2009; Prochaska et al. 2013a,b; Farina et al. 2013, 2014; Johnson et al. 2015; Lau et al. 2016, 2018). A promising way to push investigation of the CGM of quasars up to the epoch of reionization is to probe the cool gas in emission. The strong flux of UV photons radiating from the AGN can be reprocessed in the Hydrogen Lyα line at 1215.7 Å (Lyman 1906; Millikan 1920) by the surrounding gas, giving rise to an extended "fuzz" of fluorescent Lyα emission (e.g., Rees 1988; Haiman & Rees 2001; Alam & Miralda-Escudé 2002). Several pioneering efforts have been performed to reveal such halos in the vicinity of $z \sim 2 - 4$ quasars (e.g., Heckman et al. 1991a,b; Christensen et al. 2006; North et al. 2012; Hennawi & Prochaska 2013; Roche et al. 2014; Herenz et al. 2015; Arrigoni Battaia et al. 2016, 2019a). This led to the general consensus that $10 - 50$ kpc nebulae are (almost) ubiquitous around intermediate redshift quasars, and that few objects (typically associated with galaxy overdensities) are surrounded by giant Lyα nebulae with sizes $> 300$ kpc, i.e. larger than the expected virial radius for such systems (e.g., Cantalupo et al. 2014; Martin et al. 2014; Hennawi et al. 2015; Cai et al. 2017).

A change of gear in these searches was driven by the recent development of the new generation of sensitive integral field spectrographs (IFS) on 10–m class telescopes, i.e. the Multi–Unit Spectroscopic Explorer (MUSE; Bacon et al. 2010) on the ESO/*VLT* and the Keck Cosmic Web Imager (KCWI; Morrissey et al. 2012, 2018) on the Keck II telescope. These instruments have been successfully exploited to map the diffuse gas in the CGM of hundreds of intermediate redshift galaxies (e.g., Wisotzki et al. 2016; Leclercq et al. 2017) and quasars (e.g., Husband et al. 2015; Borisova et al. 2016; Fumagalli et al. 2016; Arrigoni Battaia et al. 2018a, 2019a,b; Ginolfi et al. 2018; Lusso et al. 2019). The picture emerging is that the cool gas around $z \sim 2 - 4$ radio–quiet quasars has a quiescent kinematics and it is likely to be constituted of a population of compact (with sizes of $\lesssim 50$ pc) dense ($n_\mathrm{H} \gtrsim 1 \, \mathrm{cm}^{-3}$) clouds that are optically thin to the quasar radiation (e.g., Hennawi & Prochaska 2013; Hennawi et al. 2015; Arrigoni Battaia et al. 2015b; Cantalupo 2017; Cantalupo et al. 2019).

However, by $z = 4$ the Universe is already 1.5 Gyr old and a population of massive, quiescent galaxies is already in place (e.g., Straatman et al. 2014, 2016). To probe the first

___

dances $X = 0.75$ for hydrogen and $Y = 0.25$ for helium, the Eddington time becomes $t_{\mathrm{Edd}} = 390 \, \mathrm{Myr}$

stages of galaxy formation it is thus necessary to push these studies at $z \gtrsim 6$. To date, extended Ly$\alpha$ halos have been reported only for a handful of $z \sim 6$ quasars exploiting different techniques: narrow–band imaging (Goto et al. 2009; Decarli et al. 2012; Momose et al. 2018), long–slit spectroscopy (Willott et al. 2011; Goto et al. 2012; Roche et al. 2014), and IFS (Farina et al. 2017; Drake et al. 2019). This small sample showed that the first quasars can be surrounded by extended nebulae with luminosities up to L(Ly$\alpha$) $\sim 10^{44}$ erg s$^{-1}$ and sizes $\lesssim 40$ pkpc. However, a detailed interpretation of these results is hampered by the small number statistic and by the heterogeneity of the data.

To overcome these limitations, we started the Reionization Epoch QUasars InvEstigation with MUSE (*REQUIEM*) survey aimed at performing a statistical and homogeneous census of the close environment of the first quasars. In this Paper, we report results from the investigation of the first 31 $5.7 < z < 6.6$ quasars part of this ongoing program (including the re–analysis of MUSE data from Farina et al. 2017 and Drake et al. 2019), focusing our attention on the properties of the extended Ly$\alpha$ halos as a tracer of the gas reservoirs able to fuel the activity of the first quasars. We defer the analysis of the close galactic environment of these systems to a future paper.

To summarize, the analysis of the MUSE observations (see section 3) of the 31 targets presented in section 2 with the procedure described in section 4 led to the discovery of 12 extended Ly$\alpha$ nebulae above a surface brightness limit of SB$_{Ly\alpha} \sim$ few $\times 10^{18}$ erg s$^{-1}$ cm$^{-2}$ arcsec$^{-2}$ ($\sim 40\%$ of the cases, see section 5). In section 5 we report on the attributes of the detected halos, we compare them with the properties of the quasar host galaxies and of the central supermassive black holes, and we test for possible signature of evolution of the CGM of quasars down to $z \sim 3$. Finally, a summary is given in section 6.

Throughout this paper we assume a concordance cosmology with H$_0$=70 km s$^{-1}$ Mpc$^{-1}$, $\Omega_M$=0.3, and $\Omega_\Lambda$=1-$\Omega_M$=0.7. In this cosmology, at $z$=6.2 (the average redshift of our sample) the Universe is 0.877 Gyr old, and an angular scale of $\theta$=1$''$ corresponds a proper transverse separation of 5.6 kpc. We remind the reader that MUSE is able to cover the Ly$\alpha$ line up to redshift $z \sim 6.6$ at a spectral resolution of $R = \lambda/\Delta\lambda \sim 3500$ at $\lambda \sim 9000$ Å with a spatial sampling of $0''.2 \times 0''.2$ (corresponding to 1.1 pkpc$\times$1.1 pkpc at $z = 6$) over a $\sim 1$ arcmin$^2$ field–of–view.

## 2. SAMPLE SELECTION

Our sample consists of 31 quasars in the redshift range $5.77 < z < 6.62$ located in the southern sky (e.g., Fan et al. 2001, 2003, 2006; Willott et al. 2007, 2010; Venemans et al. 2013; Jiang et al. 2016; Bañados et al. 2016; Reed et al. 2017; Mazzucchelli et al. 2017; Matsuoka et al. 2018; Wang

et al. 2018; Yang et al. 2019b). This includes all available MUSE observations of $z > 5.7$ quasars present in the ESO Archive at the time of writing (Aug. 2019). These quasars have an average redshift of $\langle z \rangle = 6.22$ and an average absolute magnitude of $\langle M_{1450} \rangle = -26.9$ mag (see Table 1 and Figure 1). Among these, only J2228+0110 is a confirmed radio–loud quasar (considering radio–loud quasars as having $R = f_{\nu,\,5\,GHz}/f_{\nu,\,4400\,Ang.} > 10$, Kellermann et al. 1989; Bañados et al. 2015b, in prep.).

In the following we will refer to the entire dataset as our *full sample*, and to the subset of 23 quasars with $M_{1450} < -25.25$ mag and $5.95 < z < 6.62$ as our *core sample*. This well defined sub–sample is highly representative of the high–$z$ population of luminous quasars (see Figure 1) and largely overlaps with the survey of dust continuum and [C II] 158 $\mu$m fine–structure emission lines in $z > 6$ quasar host–galaxies using the Atacama Large Millimeter Array (ALMA) presented in Decarli et al. (2017, 2018) and Venemans et al. (2018).

### 2.1. *Notes on Individual Objects*

*J0305−3150*—Farina et al. (2017) reported the presence of a faint nebular emission extending $\sim 9$ pkpc toward the southwest of the quasar. In addition, the presence of a Ly$\alpha$ emitter (LAE) at a projected separation of 12.5 kpc suggests that J0305−3150 is tracing an overdensity of galaxies. This hypothesis is corroborated by recent high–resolution *ALMA* imaging that revealed the presence of three [C II] 158 $\mu$m emitters located within $\sim 40$ kpc and $\sim 1000$ km s$^{-1}$ from the quasar (Venemans et al. 2019). These observations also showed the complex morphology of the host–galaxy, possibly due to interactions with nearby galaxies (Venemans et al. 2019). Ota et al. (2018), using deep narrow–band imaging obtained with the Subaru Telescope Suprime–Cam, reported an LAE number density comparable with the background. However, the displacement between the location of the redshifted Ly$\alpha$ emission and wavelengths with high response of the NB921 filter used (see Fig. 2 in Ota et al. 2018) may have hindered the detection of galaxies associated with the quasar.

*P231−20*—*ALMA* observations of this quasar revealed the presence of a massive [C II] 158 $\mu$m bright galaxy in its immediate vicinity (with a projected separation of 13.8 kpc and a velocity difference of 591 km s$^{-1}$, Decarli et al. 2017). A sensitive search for the rest–frame UV emission from this companion galaxy is presented in Mazzucchelli et al. (2019). An additional weaker [C II] 158 $\mu$m emitter has been identified by Neeleman et al. (2019) 14 kpc south–southeast of the quasar. Deep MUSE observations already revealed the presence of a $\sim 18$ pkpc Ly$\alpha$ nebular emission around this quasar (Drake et al. 2019).

FARINA ET AL.

**Table 1.** Quasars observed with MUSE

| ID | RA | Dec. | Redshift | $M_{1450}$ | Prog. ID. | Exp. Time | Image Quality | $SB^1_{5\sigma}$ |
|---|---|---|---|---|---|---|---|---|
| | (J2000) | (J2000) | | (mag) | | (sec.) | ($''$) | (erg s$^{-1}$ cm$^{-2}$ arcsec$^{-2}$) |
| J0305−3150 | 03:05:16.916 | −31:50:55.90 | 6.6145±0.0001[a] | −26.12 | 094.B-0893 | 8640. | 0.53 | 0.29×10$^{-17}$ |
| P323+12 | 21:32:33.191 | +12:17:55.26 | 6.5881±0.0003[b] | −27.06 | 0101.A-0656 | 2964. | 0.85 | 0.48×10$^{-17}$ |
| P231−20 | 15:26:37.841 | −20:50:00.66 | 6.5864±0.0005 | −27.14 | 099.A-0682 | 11856. | 0.63 | 0.30×10$^{-17}$ |
| P036+03 | 02:26:01.876 | +03:02:59.39 | 6.5412±0.0018[c] | −27.28 | 0101.A-0656 | 2964. | 0.61 | 0.33×10$^{-17}$ |
| J2318−3113 | 23:18:18.351 | −31:13:46.35 | 6.4435±0.0004 | −26.06 | 0101.A-0656 | 2964. | 0.65 | 0.54×10$^{-17}$ |
| P183+05 | 12:12:26.981 | +05:05:33.49 | 6.4386±0.0004 | −26.98 | 099.A-0682 | 2964. | 0.62 | 0.92×10$^{-17}$ |
| J0210−0456 | 02:10:13.190 | −04:56:20.90 | 6.4323±0.0005[d] | −24.47 | 0103.A-0562 | 2964. | 1.24 | 0.26×10$^{-17}$ |
| J2329−0301 | 23:29:08.275 | −03:01:58.80 | 6.4164±0.0008[e] | −25.19 | 60.A-9321 | 7170. | 0.65 | 0.18×10$^{-17}$ |
| J1152+0055 | 11:52:21.269 | +00:55:36.69 | 6.3643±0.0005 | −25.30 | 0103.A-0562 | 2964. | 1.18 | 0.90×10$^{-17}$ |
| J2211−3206 | 22:11:12.391 | −32:06:12.94 | 6.3394±0.0010 | −26.66 | 0101.A-0656 | 2964. | 0.73 | 1.49×10$^{-17}$ |
| J0142−3327 | 01:42:43.727 | −33:27:45.47 | 6.3379±0.0004 | −27.76 | 0101.A-0656 | 2964. | 0.71 | 1.11×10$^{-17}$ |
| J0100+2802 | 01:00:13.027 | +28:02:25.84 | 6.3258±0.0010[f] | −29.09 | 0101.A-0656 | 2964. | 1.29 | 1.13×10$^{-17}$ |
| J1030+0524 | 10:30:27.098 | +05:24:55.00 | 6.3000±0.0002[g] | −26.93 | 095.A-0714 | 23152. | 0.51 | 0.08×10$^{-17}$ |
| P308−21 | 20:32:09.996 | −21:14:02.31 | 6.2341±0.0005 | −26.29 | 099.A-0682 | 17784. | 0.77 | 0.26×10$^{-17}$ |
| P065−26 | 04:21:38.052 | −26:57:15.60 | 6.1877±0.0005 | −27.21 | 0101.A-0656 | 2964. | 0.68 | 0.25×10$^{-17}$ |
| P359−06 | 23:56:32.455 | −06:22:59.26 | 6.1722±0.0004 | −26.74 | 0101.A-0656 | 2964. | 0.58 | 0.28×10$^{-17}$ |
| J2229+1457 | 22:29:01.649 | +14:57:08.99 | 6.1517±0.0005[h] | −24.72 | 0103.A-0562 | 2964. | 0.54 | 0.27×10$^{-17}$ |
| P217−16 | 14:28:21.394 | −16:02:43.29 | 6.1498±0.0011 | −26.89 | 0101.A-0656 | 2964. | 0.90 | 0.32×10$^{-17}$ |
| J2219+0102 | 22:19:17.217 | +01:02:48.90 | 6.1492±0.0002[e] | −22.54 | 0103.A-0562 | 2964. | 0.69 | 0.48×10$^{-17}$ |
| J2318−3029 | 23:18:33.100 | −30:29:33.37 | 6.1458±0.0005 | −26.16 | 0101.A-0656 | 2964. | 0.73 | 0.30×10$^{-17}$ |
| J1509−1749 | 15:09:41.778 | −17:49:26.80 | 6.1225±0.0007 | −27.09 | 0101.A-0656 | 2964. | 0.88 | 0.46×10$^{-17}$ |
| J2216−0016 | 22:16:44.473 | −00:16:50.10 | 6.0962±0.0003[i] | −23.82 | 0103.A-0562 | 2964. | 1.12 | 0.48×10$^{-17}$ |
| J2100−1715 | 21:00:54.616 | −17:15:22.50 | 6.0812±0.0005 | −25.50 | 297.A-5054 | 13338. | 0.67 | 0.23×10$^{-17}$ |
| J2054−0005 | 20:54:06.481 | −00:05:14.80 | 6.0391±0.0001[l] | −26.15 | 0101.A-0656 | 3869. | 0.81 | 0.24×10$^{-17}$ |
| P340−18 | 22:40:48.997 | −18:39:43.81 | 6.01±0.05[m] | −26.36 | 0101.A-0656 | 2964. | 0.55 | 0.26×10$^{-17}$ |
| J0055+0146 | 00:55:02.910 | +01:46:18.30 | 6.0060±0.0008[h] | −24.76 | 0103.A-0562 | 2964. | 0.75 | 0.27×10$^{-17}$ |
| P009−10 | 00:38:56.522 | −10:25:53.90 | 6.0039±0.0004 | −26.50 | 0101.A-0656 | 2964. | 0.67 | 0.27×10$^{-17}$ |
| P007+04 | 00:28:06.560 | +04:57:25.68 | 6.0008±0.0004 | −26.59 | 0101.A-0656 | 2964. | 1.19 | 0.35×10$^{-17}$ |
| J2228+0110 | 22:28:43.535 | +01:10:32.20 | 5.9030±0.0002[m] | −24.47 | 095.B-0419 | 40950. | 0.61 | 0.11×10$^{-17}$ |
| J1044−0125 | 10:44:33.042 | −01:25:02.20 | 5.7847±0.0007[i] | −27.32 | 0103.A-0562 | 2964. | 0.94 | 0.32×10$^{-17}$ |
| J0129−0035 | 01:29:58.510 | −00:35:39.70 | 5.7787±0.0001[l] | −23.83 | 0103.A-0562 | 2964. | 1.19 | 0.26×10$^{-17}$ |

**References**—Unless otherwise specified, we report systemic redshifts measured from the [C II] 158 $\mu$m emission lines by Decarli et al. (2018).

[a] [C II] 158 $\mu$m redshift from Venemans et al. (2013).

[b] [C II] 158 $\mu$m redshift from Mazzucchelli et al. (2017).

[c] [C II] 158 $\mu$m redshift from Bañados et al. (2015a).

[d] [C II] 158 $\mu$m redshift from Willott et al. (2013).

[e] [C II] 158 $\mu$m redshift from Willott et al. (2017).

[f] [C II] 158 $\mu$m redshift from Wang et al. (2016).

[g] Redshift derived by De Rosa et al. (2011) from the fit of the Mg II broad emission line.

[h] [C II] 158 $\mu$m redshift from Willott et al. (2015).

[i] [C II] 158 $\mu$m redshift from Izumi et al. (2018).

[l] [C II] 158 $\mu$m redshift from Wang et al. (2013).

[m] The [C II] 158 $\mu$m emission of P340−18 was not detected in 8 minutes ALMA integration by Decarli et al. (2018). We report the redshift inferred from the observed optical spectrum by Bañados et al. (2016).

[n] Redshift derived by Roche et al. (2014) from the measurement of the Ly$\alpha$ line.

NOTE— Seeing and 5–$\sigma$ surface brightness limits have been estimated on pseudo–narrow–band images obtained collapsing 5 wavelength channels (for a total of 6.25 Å) at the expected location of the Ly$\alpha$ emission of the quasars.
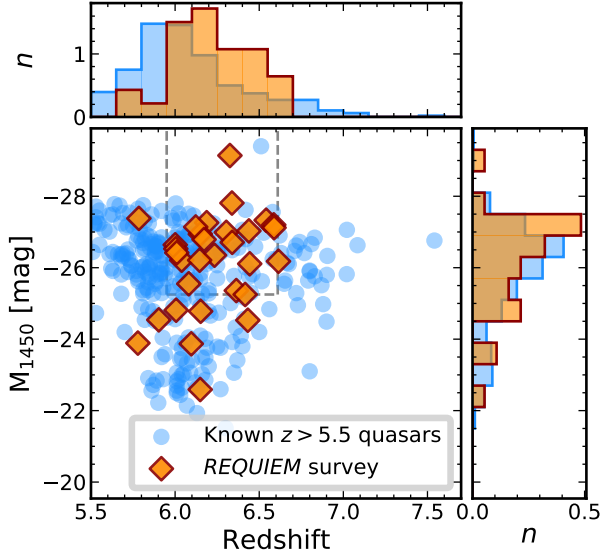
**Figure 1.** Distribution of all $z > 5.5$ quasars known to date in the redshift vs. absolute magnitude plane at 1450 Å (light blue circles and histograms). Orange diamonds and histograms mark targets from our survey. Histograms are normalized by the total number of targets and by the bin size (with steps 0.15 in redshift and of 0.6 mag in absolute magnitude). The limits in luminosity and redshift of our *core sample* (see section 2) are plotted as gray dashed lines. The five quasars outside these boundaries are: J0129−0035 at $z = 5.78$, J1044−0125 at $z = 5.78$, J2228+0110 at $z = 5.90$, J0055+0146 at $z = 6.01$, J2216−0016 at $z = 6.10$, J2219+0102 at $z = 6.15$, J2229+1457 at $z = 6.15$, and J2318−3113 at $z = 6.44$. A 2D Kolmogorov–Smirnov test (Fasano & Franceschini 1987) performed with bootstrap re–sampling of the parent dataset of the $5.95 < z < 6.62$ and $M_{1450} < -25.25$ mag quasars does not refute the null hypothesis that our *core sample* has a different distribution as the parent dataset distribution ($p - \text{value} \gtrsim 0.2$).

*P183+05* —For this quasar Bañados et al. (2019) reported the presence of a proximate damped Lyα absorption system (pDLA) located at $z=6.40$, making this system the highest redshift pDLA known to date. It shows an H I column density of $N_{HI}=10^{20.77\pm0.25}$ cm$^{-2}$ and relative chemical abundances typical of an high redshift low–mass galaxy. A deep search for emission arising from this absorption-selected galaxy will be presented in a future paper of this series (Farina et al., in prep.)

*J2329−0301* —The Lyα halo of this quasar has been the subject of several studies (Goto et al. 2009, 2012; Willott et al. 2011; Momose et al. 2018; Drake et al. 2019). Goto et al. (2017) reported the complete absence of LAEs down to a narrow–band magnitude of NB906=25.4 mag (at 50% completeness) in the entire field–of–view of the Subaru Telescope Suprime–Cam ($\sim 200$ cMpc$^2$).

*J0100+2802* —With $M_{1450} = -29.09$ mag, J0100+2802 is the brightest (unlensed) quasar known at $z > 6$ (Wu et al. 2015). Sub–arcsecond resolution observations of the [C II] 158 $\mu$m and CO emission lines suggest that the host galaxy has a dynamical mass of only $\sim 1.9 \times 10^{11}$ M$_\odot$ (Wang et al. 2019). Given this high luminosity, its proximity zone appears to be small [$R_p = (7.12 \pm 0.13)$ pMpc], implying that this quasar is relatively young, with a quasar age of $t_{QSO} \sim 10^5$ years (Eilers et al. 2017; Davies et al. 2019b).

*J1030+0524* —Deep broad band optical and near–IR investigation evidenced an overdensity of Lyman–Break galaxies in the field of this quasar (Morselli et al. 2014; Balmaverde et al. 2017). Searches for the presence of Lyα extended emission around this target has already been investigated with sensitive *HST* observations by Decarli et al. (2012) and with MUSE by Drake et al. (2019).

*P308−21* —The [C II] 158 $\mu$m emission line of this quasar host–galaxy is displaced by $\sim$25 kpc and shows an enormous velocity gradient extending across more than 1000 km s$^{-1}$ (Decarli et al. 2017). High–resolution *ALMA* and *HST* observations revealed that the host–galaxy emission is split into (at least) three distinct components. The observed gas morphology and kinematics is consistent with the close interaction of a single satellite with the quasar (Decarli et al. 2019). Deep *Chandra* observations the companion galaxy might contain a heavily–obscured AGN (Connor et al. 2019). A direct comparison of our new MUSE data with the *ALMA* [C II] 158 $\mu$m and dust maps will be presented in a forthcoming paper (Farina et al. in prep.).

*J2229+1457* —With a size of only $R_p = (0.45\pm0.14)$ pMpc, the proximity zone of this object is the smallest among the 31 $5.8 \lesssim z \lesssim 6.5$ quasars investigated by Eilers et al. (2017). This suggests a short quasar age ($t_{QSO} \lesssim 10^5$ years) for this object (Eilers et al. 2017; Davies et al. 2019b).

*J2219+0102* —This is the faintest target in our survey. Despite the low luminosity of the accretion disk, the host galaxy is undergoing a powerful starburst detected at mm–wavelengths (with an inferred star–formation rate of SFR $\sim 250$ M$_\odot$ yr$^{-1}$) and appears to be resolved with a size of 2–3 kpc (Willott et al. 2017).

*J2216−0016* —The rest–frame UV spectrum of this faint quasar shows a N V broad absorption line (Matsuoka et al. 2016). The structure of the [C II] 158 $\mu$m line appears to be complex, suggesting the presence of a companion galaxy merging with the quasar host–galaxy (Izumi et al. 2018)

*J2100−1715* —Decarli et al. (2017) reported the presence of a [C II] 158 $\mu$m bright companion located at a projected separation of 60.7 kpc and with a velocity difference of $-41$ km s$^{-1}$

from the quasar's host galaxy. The search for the Ly$\alpha$ emission arising from this companion in the MUSE data is presented in Mazzucchelli et al. (2019). Drake et al. (2019) reported the absence of extended Ly$\alpha$ emission around this quasar.

*P007+04* —The broad Ly$\alpha$ line of this quasar is truncated by the presence of a pDLA (see Figure 14 in Appendix A). The analysis of the absorbing gas generating this feature and the search for its rest–frame UV counterpart will be presented in a future paper of this series (Farina et al., in prep.).

*J2228+0110* —A faint, extended Ly$\alpha$ emission has been detected by Roche et al. (2014) in deep long–slit spectroscopic observations of this faint radio–loud quasar (with radio–loudness: $R\sim60$, Bañados et al. 2015b). The presence of the halo was confirmed by Drake et al. (2019) with MUSE observations.

*J1044−0125* —ALMA $0\rlap{.}''2$ resolution observations of the [C II] 158 $\mu$m fine structure line showed evidence of turbulent gas kinematics in the host galaxy and revealed the possible presence of a faint companion galaxy located at a separation of 4.9 kpc (Wang et al. 2019).

## 3. OBSERVATIONS AND DATA REDUCTION

Observations of the quasars in our sample have been collected with the MUSE instrument on the *VLT* telescope *YEPUN* as a part of the ESO programs: 60.A-9321(A, Science Verification), 094.B-0893(A, PI: Venemans), 095.B-0419(A, PI: Roche), 095.A-0714(A, PI: Karman), 099.A-0682(A, PI: Farina), 0101.A-0656(A, PI: Farina), 0103.A-0562(A, PI: Farina), and 297.A-5054(A, PI: Decarli). Typically, the total time on target was $\sim50$ min, divided into two exposures of 1482 s differentiated by a $<5''$ shift and a 90 degree rotation. For eight targets, longer integrations have been acquired and the shift and rotation pattern was repeated several times (see Table 1)

Data reduction was performed as in Farina et al. (2017) using the MUSE DATA REDUCTION SOFTWARE version 2.6 (Weilbacher et al. 2012, 2014) complemented by our own set of custom built routines. Basic steps are summarized in the following. Individual exposures were bias subtracted, corrected for flat field and illumination, and calibrated in wavelength and flux. We then subtracted the sky emission and re–sampled the data onto a $0\rlap{.}''2\times0\rlap{.}''2\times1.25$ Å grid[2]. White light images were then created and used to estimate the relative offsets between different exposures of a single target.

From these images we also determined the relative flux scaling between exposures by performing force photometry on sources in the field. Finally, we average–combined the exposures into a single cube. Residual illumination patterns were removed using the ZURICH ATMOSPHERE PURGE (ZAP) software (version 2.0 Soto et al. 2016), setting the number of eigenspectra (`nevals`) to 3 and masking sources detected in the white light images. This procedure, however, comes with the price of possibly removing some astronomical flux from the cubes. In the following, we will present results from the "cleaned" datacubes. However, we also double checked for extended emission in the data prior to the use of ZAP. To take voxel–to–voxel correlations into account, that can result in an underestimation of the noise calculated by the pipeline, we rescaled the variance datacube to match the measured variance of the background (see e.g., Bacon et al. 2015; Borisova et al. 2016; Farina et al. 2017; Arrigoni Battaia et al. 2019a). The astrometry solution was refined by matching sources with the Pan–STARRS1 (PS1) data archive (Chambers et al. 2016; Flewelling et al. 2016) or with other available surveys if the field was not covered by the PS1 footprint. We corrected for reddening towards the quasar location using $E(B-V)$ values from Schlafly & Finkbeiner (2011) and assuming $R_V$=3.1 (e.g., Cardelli et al. 1989; Fitzpatrick 1999). Absolute flux calibration was obtained matching the $z$–band photometry of sources in the field with PS1 and/or with the Dark Energy Camera Legacy Survey[3]. In Table 1 we report the 5–$\sigma$ surface brightness limits estimated over a 1 arcsec$^2$ aperture after collapsing 5 wavelength slices that were centered at the expected position of the Ly$\alpha$ line shifted to the systemic redshift of the quasar (SB$^1_{5\,\sigma,\mathrm{Ly}\alpha}$). These range from SB$^1_{5\,\sigma,\mathrm{Ly}\alpha}$=0.1 to $1.1\times10^{-17}$erg s$^{-1}$ cm$^{-2}$ arcsec$^{-2}$ depending on exposure times, sky conditions, and on the redshift of the quasar. Postage stamps of the quasar vicinities and quasar spectra are shown in Appendix A.

## 4. SEARCHING FOR EXTENDED EMISSION

An accurate PSF subtraction is necessary to recover the faint signal of the diffuse Ly$\alpha$ emission emerging from the PSF wings of the bright unresolved nuclear component. The steps we executed on each datacube to accomplish this goal are summarized in the following:

1. We removed possible foreground objects located in close proximity to the quasar. To perform this step, we first collapsed the datacube along wavelengths blueward of the redshifted Ly$\alpha$ line location. Due to the Gunn–Peterson effect, the resulting image is virtually free of any object with a redshift consistent with or larger than the quasar's one. For each source detected

---

[2] Cosmic rays could have an impact on the final quality of the cubes when only two exposures have been collected. Their rejection is performed by the pipeline in the post–processing of the data considering a sigma rejection factor of `crsigma=15`.

[3] http://legacysurvey.org/

in this image we extracted the emission over an aperture 3 times larger than the effective radius. We used this as an empirical model of the object's light profile. This model was then propagated through the datacube by rescaling it to the flux of source measured at each wavelength channel. Finally, all these models were combined together and subtracted from the datacube.

2. An empirical model of the PSF was created by summing up spectral regions virtually free of any extended emission, i.e. $> 2500 \, \mathrm{km \, s^{-1}}$ from the wavelength of the Ly$\alpha$ line redshifted to the systemic redshift of the quasar. For this procedure, we excluded all channels where the background noise was increased by the presence of bright sky emission lines.

3. In each wavelength layer, the PSF model was rescaled to match the quasar flux measured within a radius of 2 spatial pixels, assuming that the unresolved emission of the AGN dominates whitin this region.

4. Following a similar procedure as in, e.g., Hennawi & Prochaska (2013); Arrigoni Battaia et al. (2015a); Farina et al. (2017) we created a smoothed $\chi_{x,y,\lambda}$ cube defined as:

$$\mathrm{SMOOTH}\,[\chi_{x,y,\lambda}] =$$
$$= \frac{\mathrm{CONVOL}\,[\mathrm{DATA_{x,y,\lambda}} - \mathrm{MODEL_{x,y,\lambda}}]}{\sqrt{\mathrm{CONVOL}^2\,\left[\sigma_{x,y,\lambda}^2\right]}} \quad (2)$$

where $\mathrm{DATA_{x,y,\lambda}}$ is the datacube, $\mathrm{MODEL_{x,y,\lambda}}$ is the PSF model created in the step above, $\sigma_{x,y,\lambda}$ is the square root of the variance datacube, and the operation CONVOL is a convolution with a 3D Gaussian kernel with $\sigma_{\mathrm{spat}}{=}0\farcs2$ in each spatial direction and $\sigma_{\mathrm{spec}}{=}2.50\,\text{Å}$ in the spectral direction.

5. To identify significant extended emission, we then ran a friends–of–friends algorithm that connects voxels that have $S/N{>}2$ in the $\mathrm{SMOOTH}\,[\chi_{x,y,\lambda}]$ cube. We chose a linking length of 2 voxels (in both spatial and spectral directions). Voxels located within the effective radius of a removed foreground source were excluded[4]. Additionally, voxels contaminated by instrumental artifacts were also excluded. We consider a group identified by the FoF as a halo associated with the quasar if, at the same time: *(i)* there is at least one

voxel with $S/N > 2$ within a radius of 1 arcsec in the spatial direction and within $\pm 250 \, \mathrm{km \, s^{-1}}$ in the spectral direction from the expected location of the Ly$\alpha$ emission of the quasar; *(ii)* it contains more than 300 connected voxels (to avoid contaminations from cosmic rays and/or instrument artifacts not fully removed by the pipeline); and *(iii)* it spans more than two consecutive channels in the spectral direction.

6. If a halo is detected, we created a 3–dimensional mask containing all connected voxels ($\mathrm{MASK_{x,y,\lambda}}$) and used it to extract information from the $\mathrm{DATA_{x,y,\lambda}}$-$-\mathrm{MODEL_{x,y,\lambda}}$ cube.

In Figure 2 we show the results of this procedure applied to the *REQUIEM* survey dataset. For each object we plot a $11'' \times 11''$ (roughly $60 \, \mathrm{pkpc} \times 60 \, \mathrm{pkpc}$ at $z = 6$) pseudo–narrow–band image centered at the quasar location. The spectral region of the cube defining each narrow–band image was set by the minimum ($\lambda_{\mathrm{min}}^{\mathrm{mask}}$) and maximum ($\lambda_{\mathrm{Max}}^{\mathrm{mask}}$) wavelengths covered by $\mathrm{MASK_{x,y,\lambda}}$ (see Table 2). The black contours highlight regions where significant (as described above) extended emission was detected.

In summary, we report the presence of 12 Ly$\alpha$ nebulae around $z > 5.7$ quasars, 8 of which are newly discovered. In the following, we describe the procedure used to extract physical information about each detected nebula.

### 4.1. *Spectra of the Extended Emission*

We extract the nebular emission spectrum using a 2D mask obtained by collapsing $\mathrm{MASK_{x,y,\lambda}}$ along the spectral axis. The construction of a halo mask described in the previous section is instrumental in obtaining the highest signal–to–noise spectrum of a detected halo. However, given that this procedure is based on a fix cut in signal–to–noise per voxel, it inevitably results in a loss of information at larger radii. For each halo we thus also extract a spectrum from the circular aperture with radius equal to the distance between the quasar and the most distant significant voxel detected in the collapsed $\mathrm{MASK_{x,y,\lambda}}$ ($d_{\mathrm{QSO}}^{\mathrm{mask}}$, see Table 2). Spectra extracted over the collapsed mask and over the circular aperture (plotted in red and in yellow in Figure 3) have similar shapes, but the latter shows a systematically higher flux density at each wavelength.

We estimate the central wavelength ($\lambda_{\mathrm{c}}$) as a non–parametric flux–and–error–weighted mean of the emission between $\lambda_{\mathrm{min}}^{\mathrm{mask}}$ and $\lambda_{\mathrm{Max}}^{\mathrm{mask}}$ (see Table 2 and Figure 3), i.e. without assuming any particular shape for the Ly$\alpha$ line. While in Table 3 we only report measurements from the *masked* spectrum, we point out that the central wavelengths measured from the 2D masks and from the circular aperture extraction are consistent within the errors, with an average difference of only $(-15 \pm 37) \, \mathrm{km \, s^{-1}}$. In order to reduce

---

[4] The empirical procedure used to remove foreground sources intrinsically conceals information (possibly) present at their center. We thus decided to mask these regions to avoid false detections and/or bias estimates of the halo properties. However, this may result in an underestimate of the total halo emission.
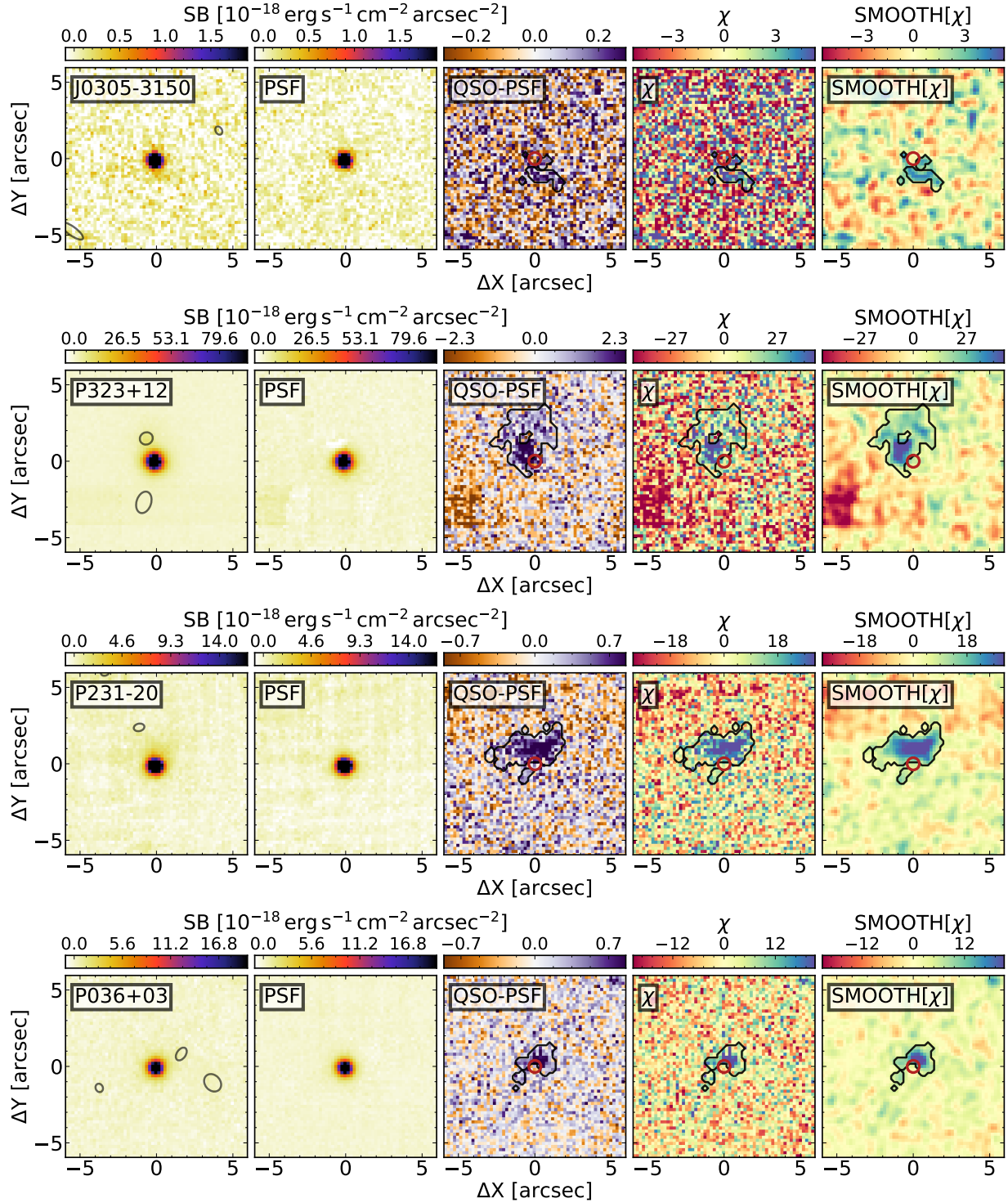
**Figure 2.** Results from the PSF–subtraction procedure described in section 4. The different panels show the pseudo–narrow–band images obtained by collapsing (from left to right) the $\mathrm{DATA_{x,y,\lambda}}$, $\mathrm{MODEL_{x,y,\lambda}}$, $\mathrm{DATA_{x,y,\lambda} - MODEL_{x,y,\lambda}}$, $\chi_{x,y,\lambda}$, and $\mathrm{SMOOTH}\,[\chi_{x,y,\lambda}]$ cubes in the wavelength range where extended emission was detected. If no significant nebular emission is present, the collapsed region is between $-500$ and $+500\,\mathrm{km\,s^{-1}}$. In the left–most panel, the location of the detected (and removed) foreground sources are marked as gray ellipses. Note that saturation spikes from nearby bright stars (e.g. in the bottom left corner of the quasar P323+12, or on the top of J1509$-$1749) and/or instrumental artifacts such as IFU–to–IFU edge effects (e.g. for the quasars P183+05 and P217$-$16) have been masked during the halo identification procedure but are still shown here.
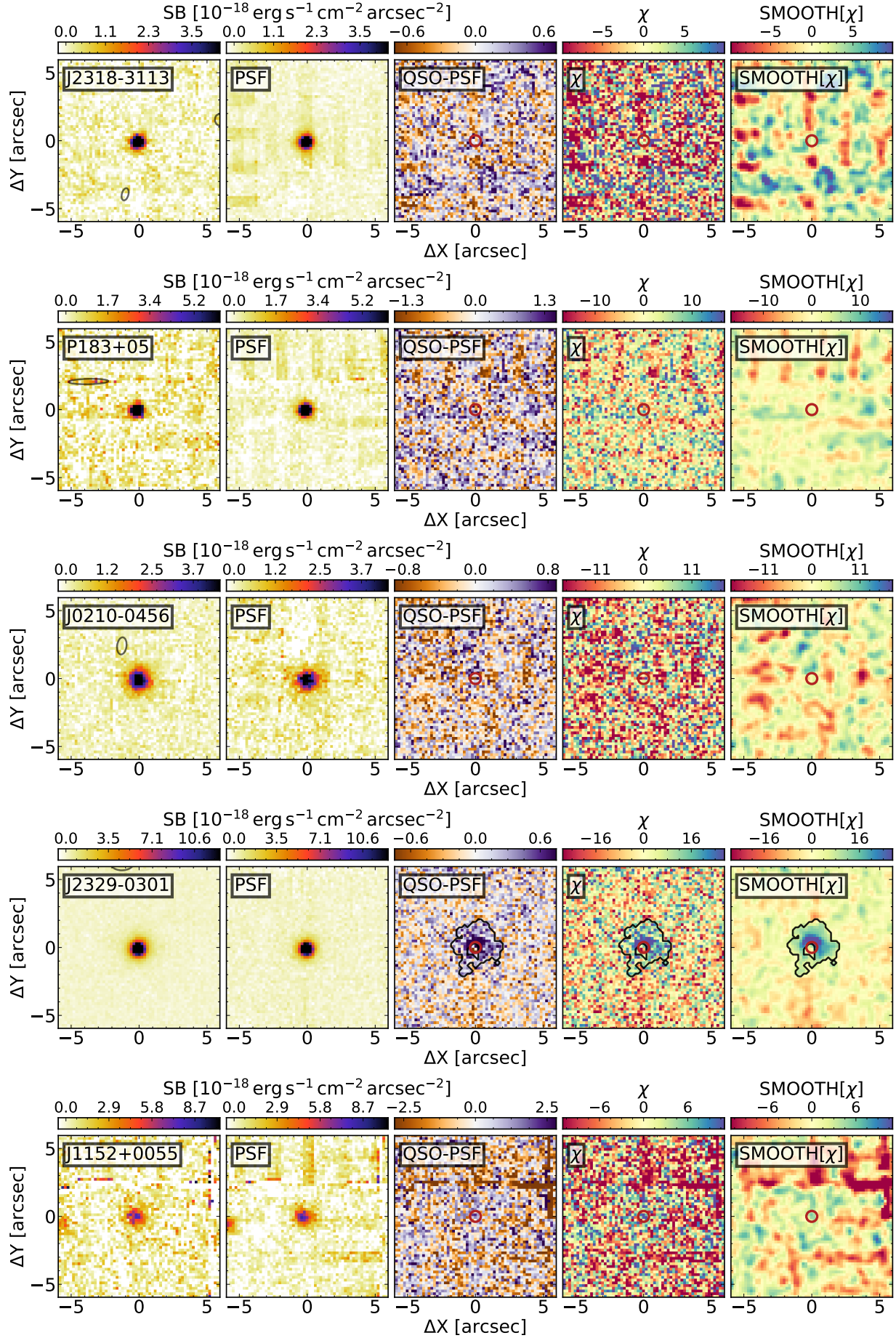
**Figure 2.** continued.
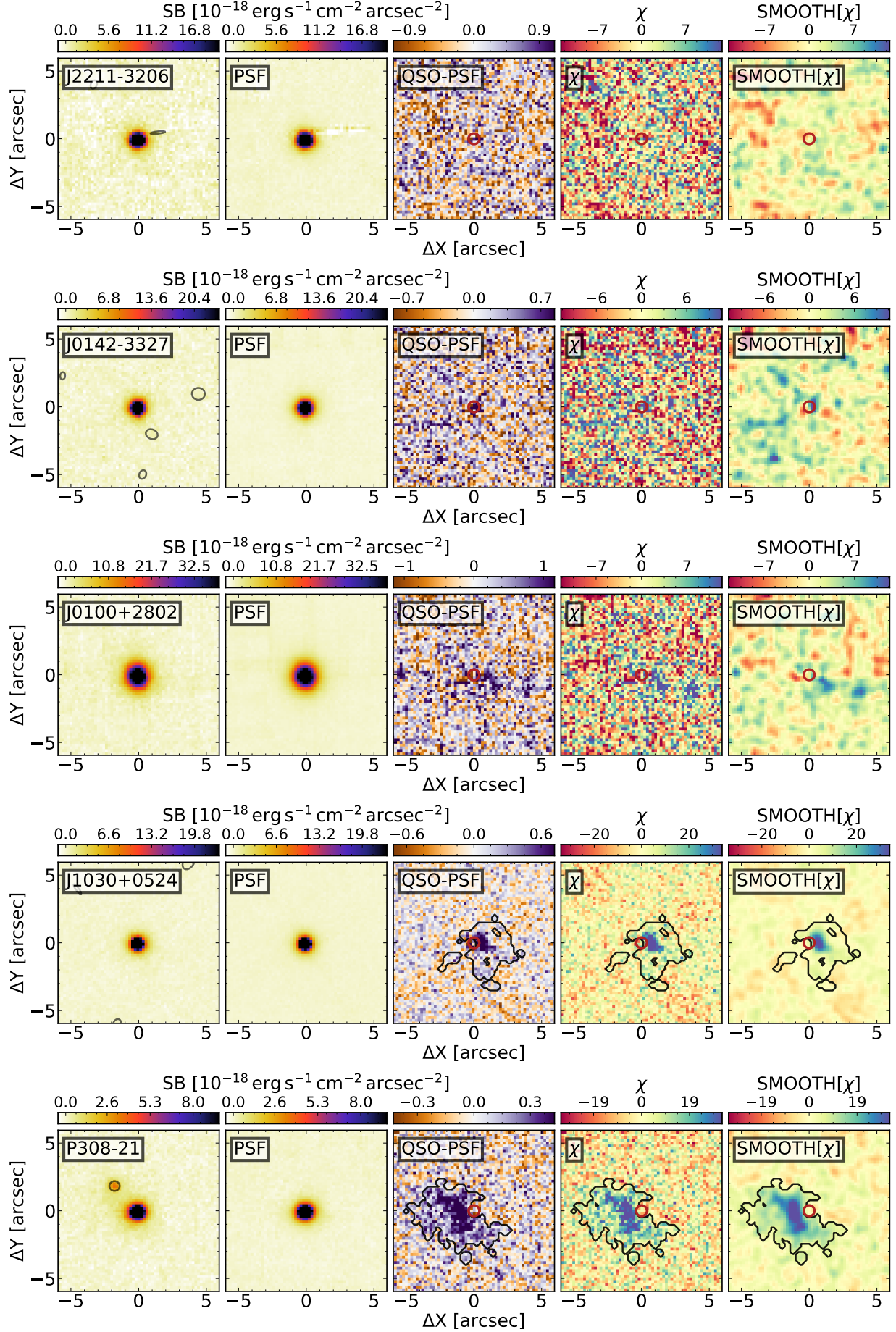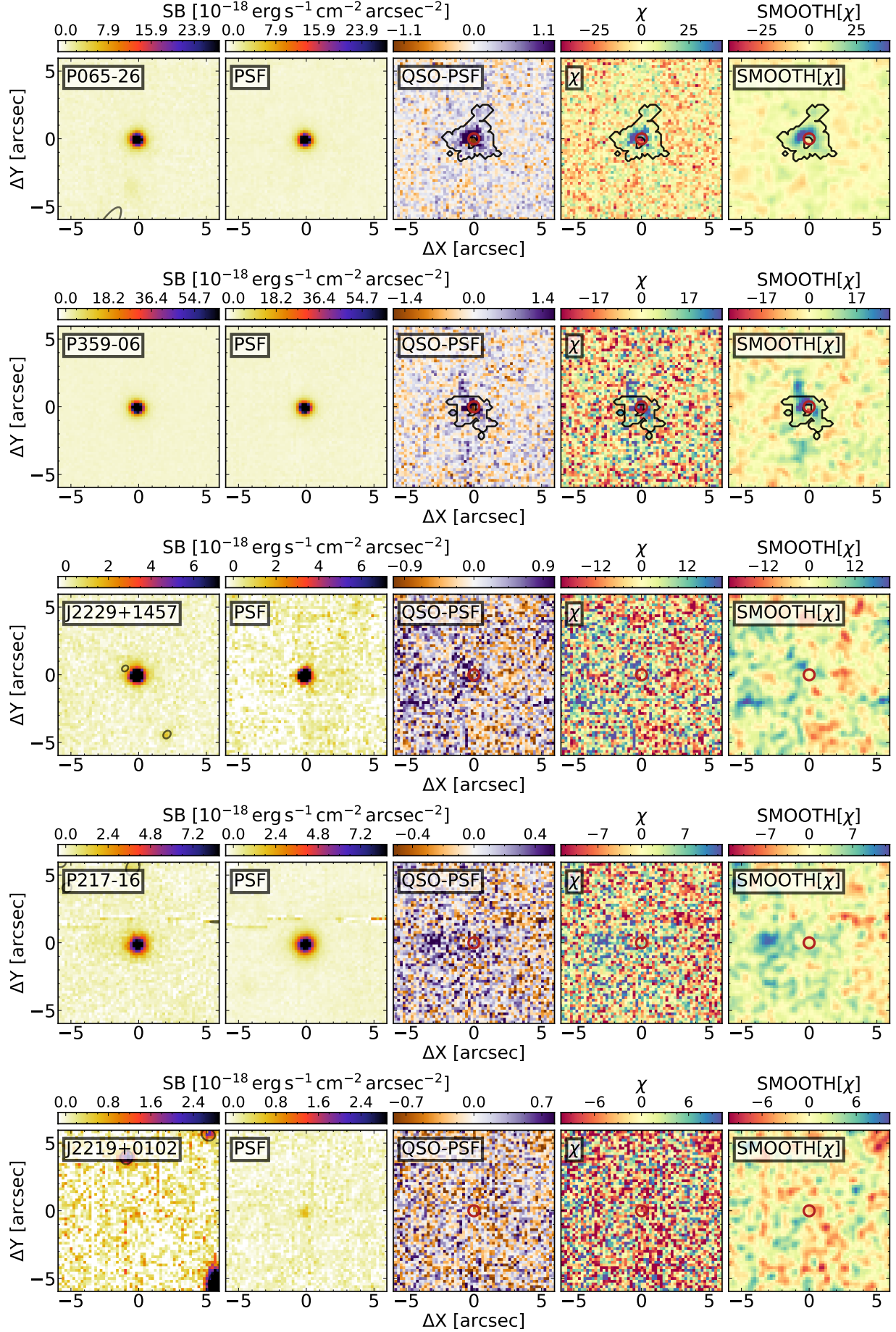
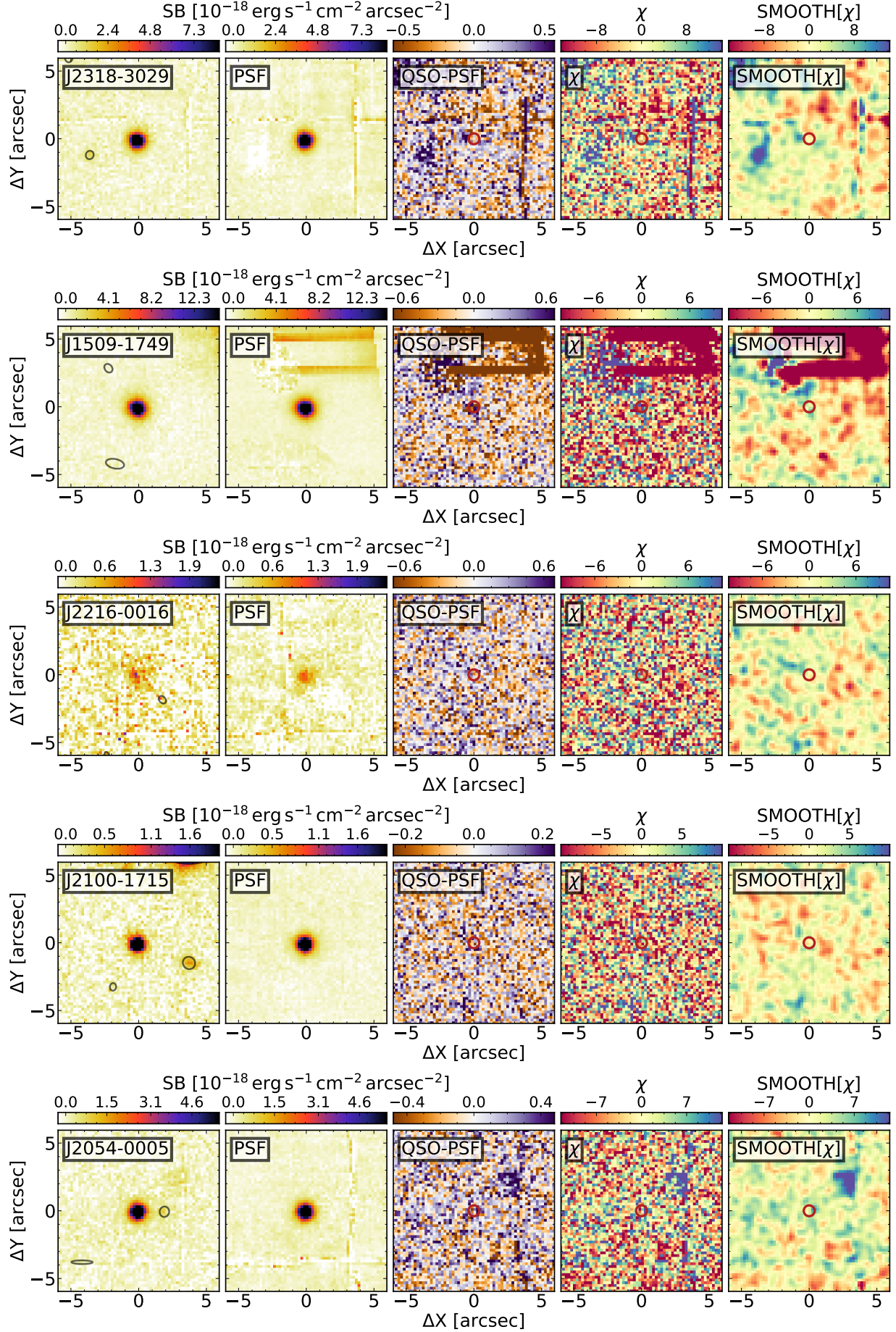**Figure 2.** continued.

**Figure 2.** continued.
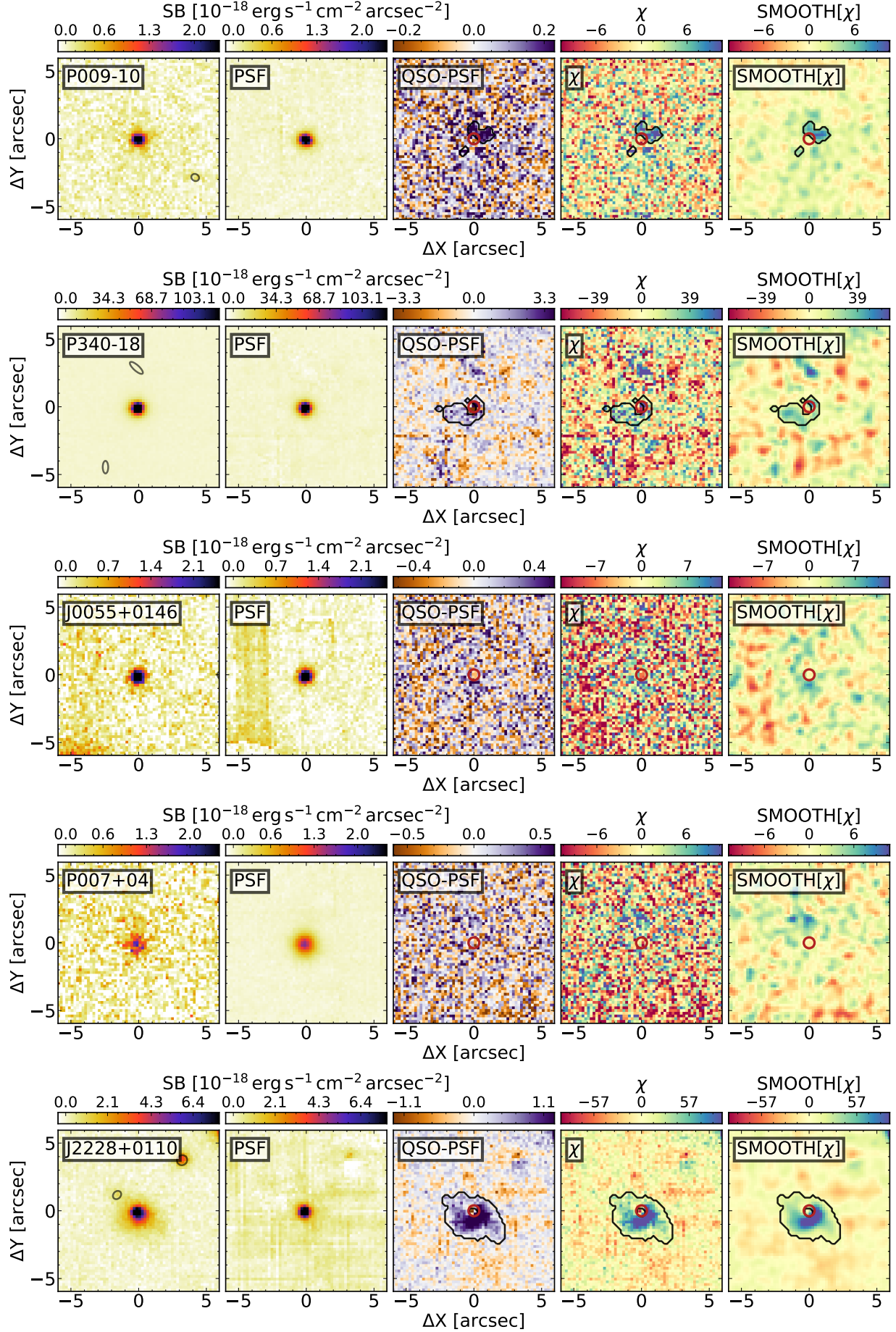
**Figure 2.** continued.
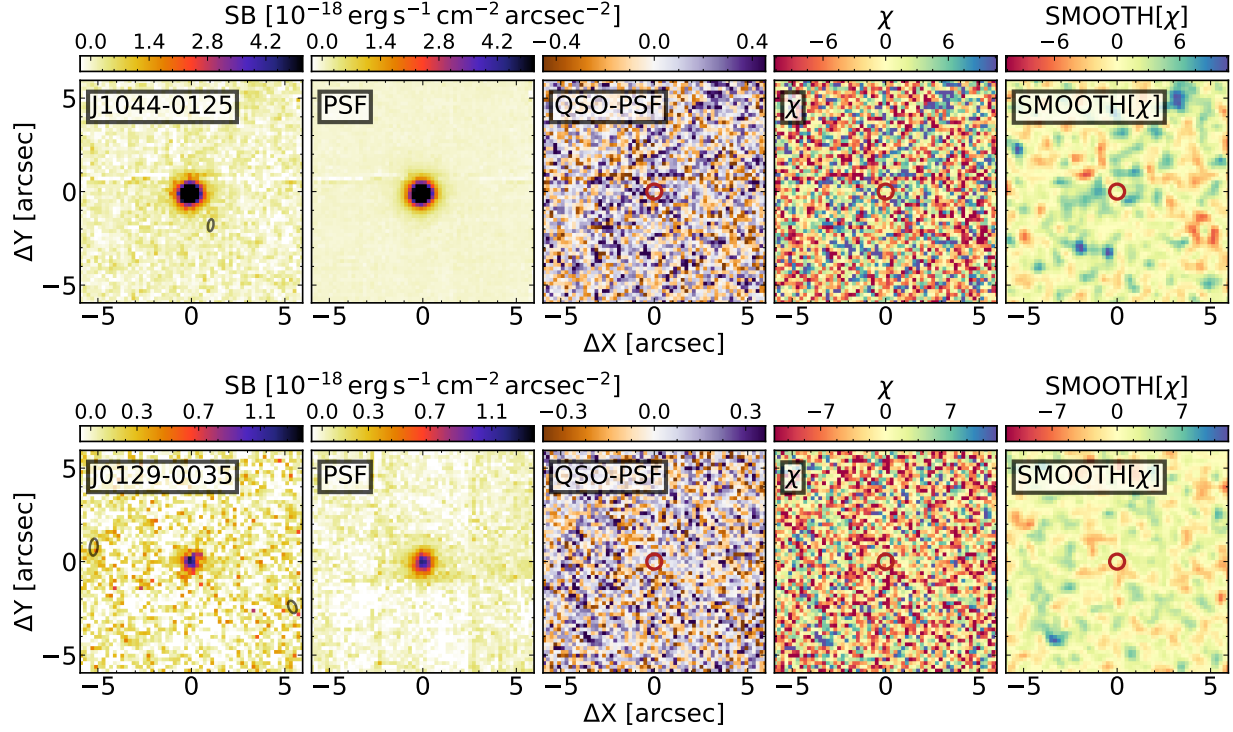
**Figure 2.** continued.

**Figure 2.** continued.

the effects of noise spikes, the FWHMs of the nebular emission were estimated after smoothing spectra extracted from the 2D masks with a Gaussian kernel of $\sigma = 2.5\,\text{Å}$. The derived FHWMs are shown as gray horizontal bars in Figure 3 and listed in Table 3. Finally, total fluxes were calculated by integrating the spectra extracted over the circular apertures between $\lambda_{\min}^{\text{mask}}$ and $\lambda_{\text{Max}}^{\text{mask}}$. If a nebula was not detected, we extracted the spectrum over a circular aperture with a fixed radius of 20 pkpc (corresponding to $3\rlap{.}''5$ at $z = 6$). From this, we derived the $1$–$\sigma$ detection limit as $\sigma_{\text{Lim}}^2 = \sum_{-500\,\text{km s}^{-1}}^{+500\,\text{km s}^{-1}} \sigma_\lambda^2 / N_\lambda$, where $\sigma_\lambda^2$ is the variance at each wavelength and $N_\lambda$ is the number of spectral pixels in the $\pm 500\,\text{km s}^{-1}$ stretch from the quasar's systemic redshift.

### 4.2. Surface Brightness Profiles

The right–hand panels of Figure 3 show circularly averaged surface brightness profiles of the extended emission around each quasar. These are extracted from pseudo–narrow band images constructed summing up spectral channels located between $-500$ and $+500\,\text{km s}^{-1}$ of the quasar's systemic redshift. The choice of a fixed width for the entire sample facilitates a uniform comparison of both detections and non–detections of nebular emission. In addition, this velocity range corresponds to $30\,\text{Å}$, matching the width of the pseudo–narrow–band images used to extract surface brightness profiles by Arrigoni Battaia et al. (2019a) for their sample of $z \sim 3$ quasars. However, the size of the bin selected by Arrigoni Battaia et al. is twice as large as ours in velocity

space. This is also much narrower than previous narrow–band studies targeting high–redshift quasars: e.g., $\sim 100\,\text{Å}$ in Decarli et al. (2012) or $\sim 160\,\text{Å}$ in Momose et al. (2018). While this choice may lead to the loss of some signal from the wings of the nebulae, it allows us to optimize the signal–to–noise ratio of the extended emission whilst being sensitive to faint emission that may be present at larger scales. Before extracting the profile binned in annuli with radii evenly spaced in logarithmic space, we masked regions where apparent instrumental artifacts were present and regions located within the effective radius of the removed foreground sources. Errors associated to each bin of the surface brightness profile were estimated from the collapsed variance datacube.

### 4.3. Moment Maps

In order to trace the kinematics of the detected extended emission we produced the zeroth, first, and second moment maps of the flux distribution in velocity space (see Figure 4). These maps encode information about the variation of the line centroid velocity and width at different spatial locations. To create the maps, we first smoothed each wavelength layer with a 2D Gaussian kernel with $\sigma = 1$ spatial pixel. Then we extracted the the different moments within the $\text{MASK}_{\text{x,y,}\lambda}$ region (i.e. only voxels significantly associated with the halo are included in the maps). Given the complex kinematics of the Ly$\alpha$ emission observed around high redshift quasars (e.g. Martin et al. 2015; Borisova et al. 2016; Ginolfi et al. 2018; Arrigoni Battaia et al. 2018a, 2019a; Drake et al. 2019) and
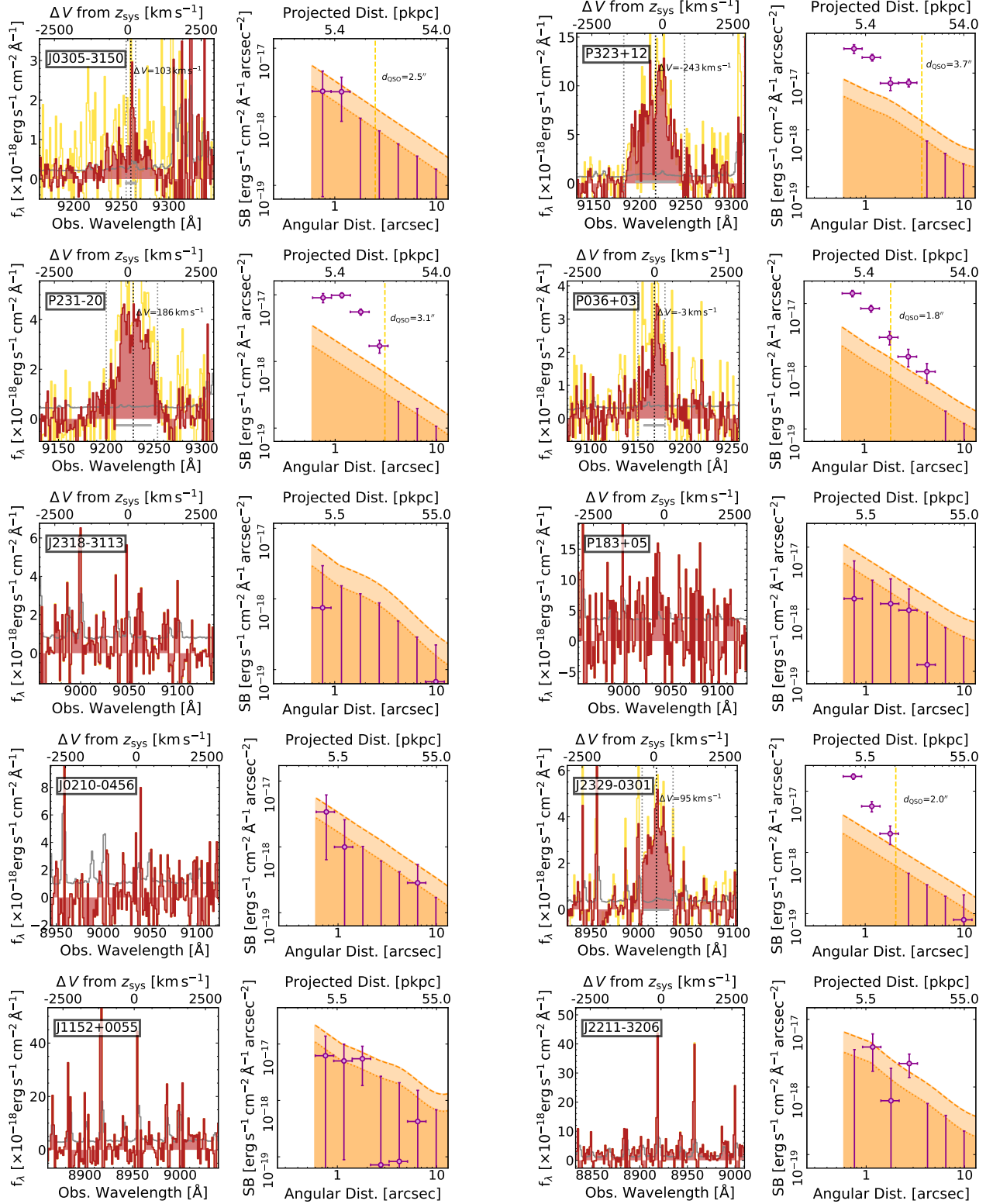
**Figure 3.** Atlas of spectra and surface brightness profiles of extended emission detected in the *REQUIEM* survey. *Left–hand panel* — Spectrum of the nebular emission extracted over the collapsed halo mask as described in subsection 4.1 (red shaded histogram) with corresponding 1−σ error (gray histogram). The spectrum extracted over a circular aperture of radius $d_{\rm QSO}$ is also shown as a yellow histogram. The vertical dotted lines mark the wavelength range where the extended emission was detected and the location of its flux–weighted centroid. In the cases where no halo was detected, the spectrum extracted from a circular aperture of radius 20 pkpc is plotted. *Right–hand panel* — Surface brightness profile extracted over circular annuli evenly spaced in logarithmic space (purple points). The formal 1− and 2−σ error in surface brightness are plotted as orange shaded regions (see subsection 4.2 for further details).

**Figure 3.** continued.
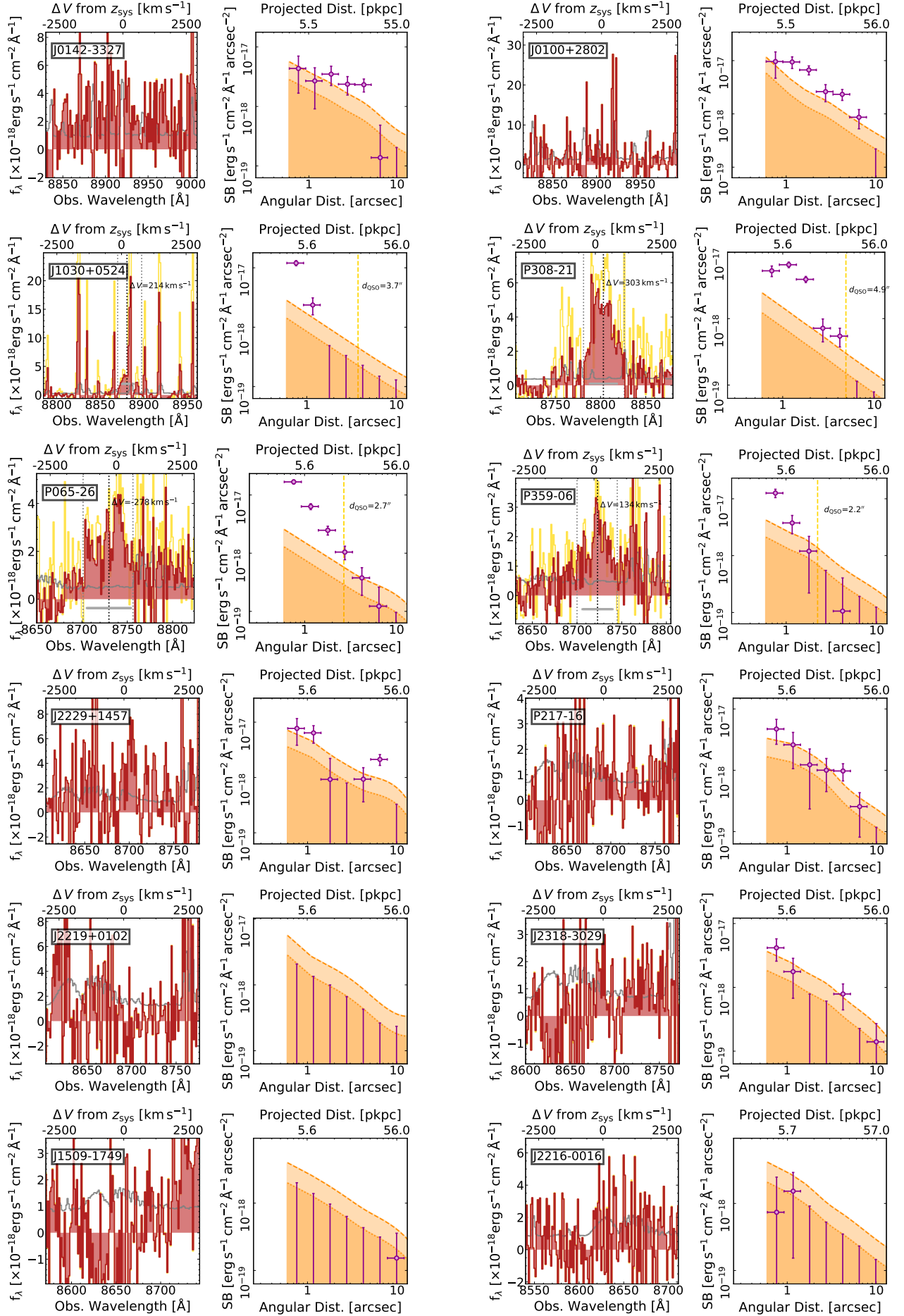
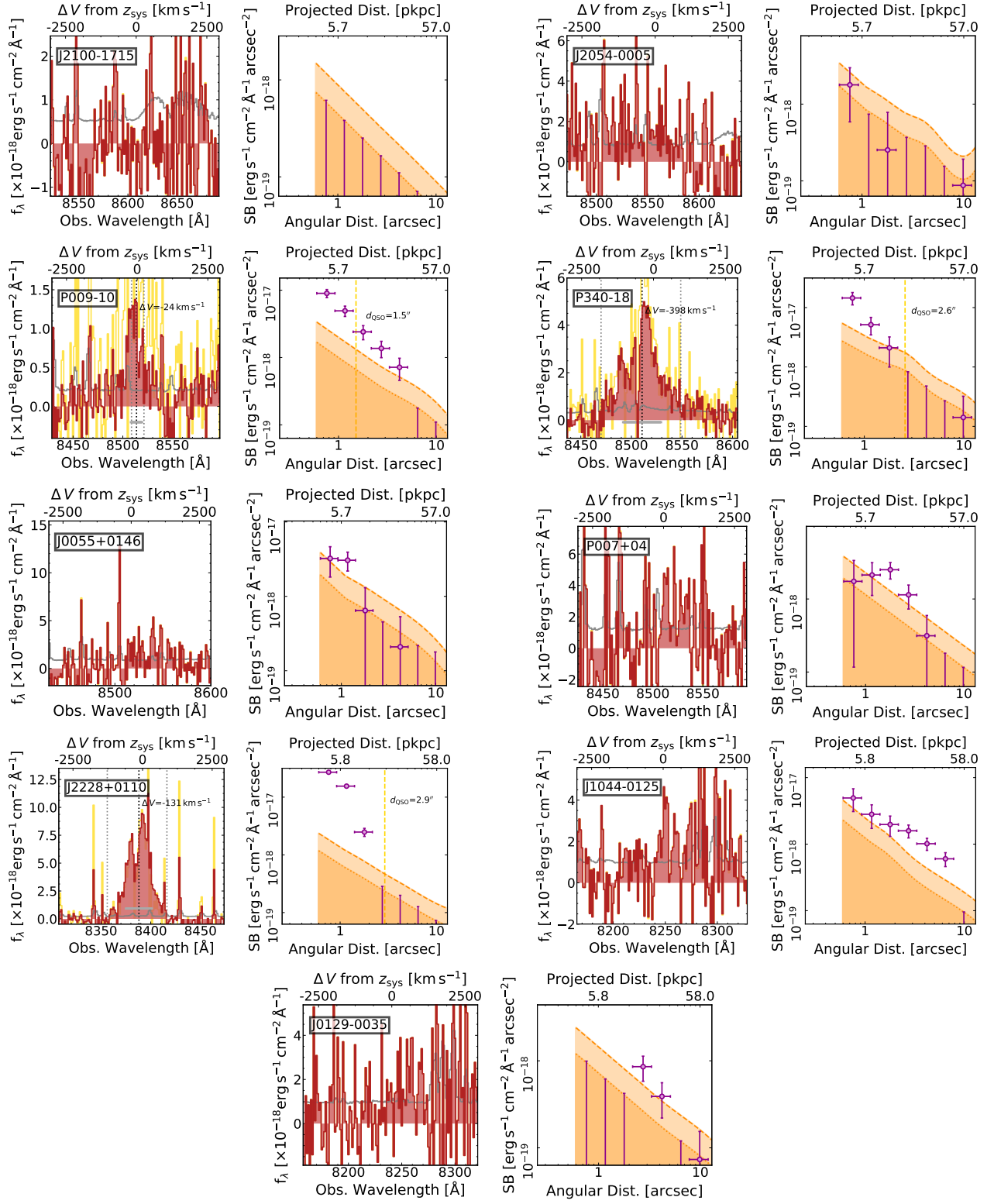**Figure 3.** continued.

**Table 2.** Summary of $MASK_{x,y,\lambda}$ properties of identified nebulae.

| ID | $\lambda_{min}^{mask}-\lambda_{max}^{mask}$ | $d_{Max}^{mask}$ | $d_{QSO}^{mask}$ | $A_{Halo}^{mask}$ |
|---|---|---|---|---|
| | (Å) | ($''$/pkpc) | ($''$/pkpc) | (arcsec$^2$) |
| J0305−3150 | 9255.0–9265.0 | 3.1/16.8 | 2.5/13.5 | 1.8 |
| P323+12 | 9182.5–9248.8 | 4.6/24.7 | 3.7/20.2 | 8.6 |
| P231−20 | 9200.0–9253.8 | 5.1/27.6 | 3.1/16.8 | 7.8 |
| P036+03 | 9150.0–9178.8 | 3.6/19.4 | 1.8/ 9.9 | 2.8 |
| J2318−3113 | ⋯ | ⋯ | ⋯ | ⋯ |
| P183+05 | ⋯ | ⋯ | ⋯ | ⋯ |
| J0210−0456 | ⋯ | ⋯ | ⋯ | ⋯ |
| J2329−0301 | 9003.8–9036.3 | 4.0/22.3 | 2.0/11.2 | 6.9 |
| J1152+0055 | ⋯ | ⋯ | ⋯ | ⋯ |
| J2211−3206 | ⋯ | ⋯ | ⋯ | ⋯ |
| J0142−3327 | ⋯ | ⋯ | ⋯ | ⋯ |
| J0100+2802 | ⋯ | ⋯ | ⋯ | ⋯ |
| J1030+0524 | 8870.0–8897.5 | 6.1/34.0 | 3.7/20.7 | 10.3 |
| P308−21 | 8781.3–8826.3 | 7.7/43.2 | 4.9/27.4 | 18.2 |
| P065−26 | 8701.3–8756.3 | 4.4/24.7 | 2.7/15.0 | 7.2 |
| P359−06 | 8700.0–8745.0 | 3.0/16.9 | 1.6/ 9.1 | 2.7 |
| J2229+1457 | ⋯ | ⋯ | ⋯ | ⋯ |
| P217−16 | ⋯ | ⋯ | ⋯ | ⋯ |
| J2219+0102 | ⋯ | ⋯ | ⋯ | ⋯ |
| J2318−3029 | ⋯ | ⋯ | ⋯ | ⋯ |
| J1509−1749 | ⋯ | ⋯ | ⋯ | ⋯ |
| J2216−0016 | ⋯ | ⋯ | ⋯ | ⋯ |
| J2100−1715 | ⋯ | ⋯ | ⋯ | ⋯ |
| J2054−0005 | ⋯ | ⋯ | ⋯ | ⋯ |
| P340−18 | 8470.0–8548.8 | 3.2/18.4 | 2.6/14.6 | 3.0 |
| J0055+0146 | ⋯ | ⋯ | ⋯ | ⋯ |
| P009−10 | 8508.8–8521.3 | 2.7/15.4 | 1.5/ 8.6 | 1.4 |
| P007+04 | ⋯ | ⋯ | ⋯ | ⋯ |
| J2228+0110 | 8356.3–8416.3 | 5.2/29.7 | 2.8/16.0 | 10.2 |
| J1044+0125 | ⋯ | ⋯ | ⋯ | ⋯ |
| J0129−0035 | ⋯ | ⋯ | ⋯ | ⋯ |

NOTE—For each detected nebula we report the spectral range where significant emission was detected ($\lambda_{min}^{mask}$–$\lambda_{max}^{mask}$), and, projected on the sky, its maximum extent ($d_{Max}^{mask}$), the distance between the quasar and the furthest significant voxel ($d_{QSO}^{mask}$), and the total area covered by the mask ($A_{Halo}^{mask}$, see section 4 for further details).

the relatively low spectral resolution of MUSE, the moments are estimated in a non–parametric way by flux–weighting each voxel. In other words, no assumption was made about the 3D shape of the line emitting region.

## 5. RESULTS AND DISCUSSION

The analysis of the fields of the 31 quasars that constitute the *REQUIEM* survey revealed the presence of extended Lyα emission around ∼39% of the sample (12 out of 31 targets, 11/23 considering only our *core sample*). At the face value, this detection rate is lower than the 100% reported for $z \sim 3$ quasars by Borisova et al. (2016) and Arrigoni Battaia et al. (2019a). However, only ∼ 50% of the Arrigoni Battaia et al. (2019a) would be detected if their surface brightness limit are rescaled to compensate for the effects of the cosmological dimming (a factor of ∼ 10× from $z \sim 3$ to $z \sim 6$). These nebulae show a variety of morphologies and properties, spanning a factor of 25 in luminosity (from $8 \times 10^{42}$ to $2 \times 10^{44}$ erg s$^{-1}$), have FWHM ranging from ∼ 300 to ∼ 1700 km s$^{-1}$, and maximum sizes from ∼ 8 to ∼ 27 pkpc. In the following, we investigate the origin of this emission, relate it to the properties of the central powering source, and compare with lower redshift samples.

### 5.1. *Extended Halos and Quasar Host–Galaxies*

For all but three quasars in our sample (i.e., J1030+0524, J2228+0110, and P340−18) sensitive mm–observations of the [C II] 158 $\mu$m emission line and of the underlying far–infrared continuum were collected (see Decarli et al. 2018; Venemans et al. 2018; and references therein). These measurements give us the possibility to directly test for connections between the properties of quasar host–galaxies and the extended Lyα halos where they reside.

#### 5.1.1. *Velocity shifts with respect to the systemic redshifts*

We first estimate the velocity difference ($\Delta V_{sys}$) between the flux–weighted centroid of the extended emission and the precise systemic redshift of the quasar host–galaxies provided by the [C II] 158 $\mu$m line. If no measurement of the [C II] 158 $\mu$m emission line is available in the literature (see Table 1) we consider systemic redshifts from the quasar broad Lyα or Mg II emission lines (including the empirical correction for Mg II-based systemic redshifts from Shen et al. 2016). The velocity difference is defined as:

$$\Delta V_{sys} = \frac{c\,(z_{Ly\alpha} - z_{sys})}{1 + z_{sys}} \qquad (3)$$

where $c$ is the speed of light. This means that a positive $\Delta V_{sys}$ corresponds to a halo shifted redward of the systemic redshift.

All the detected halos have velocity shifts between $\Delta V_{sys} = -500$ km s$^{-1}$ and $+500$ km s$^{-1}$, with an average (median) $\langle \Delta V_{sys} \rangle = (+71 \pm 31)$ km s$^{-1}$ ($+54$ km s$^{-1}$). This value agrees with $\langle \Delta V_{sys} \rangle = (+69 \pm 36)$ km s$^{-1}$ (with a median of $+112$ km s$^{-1}$) calculated taking only [C II] 158 $\mu$m redshifts into account (see the left–hand panel of Figure 5). These small velocity differences hint at a strong connection between the extended halos and $z \sim 6$ quasar host–galaxies.
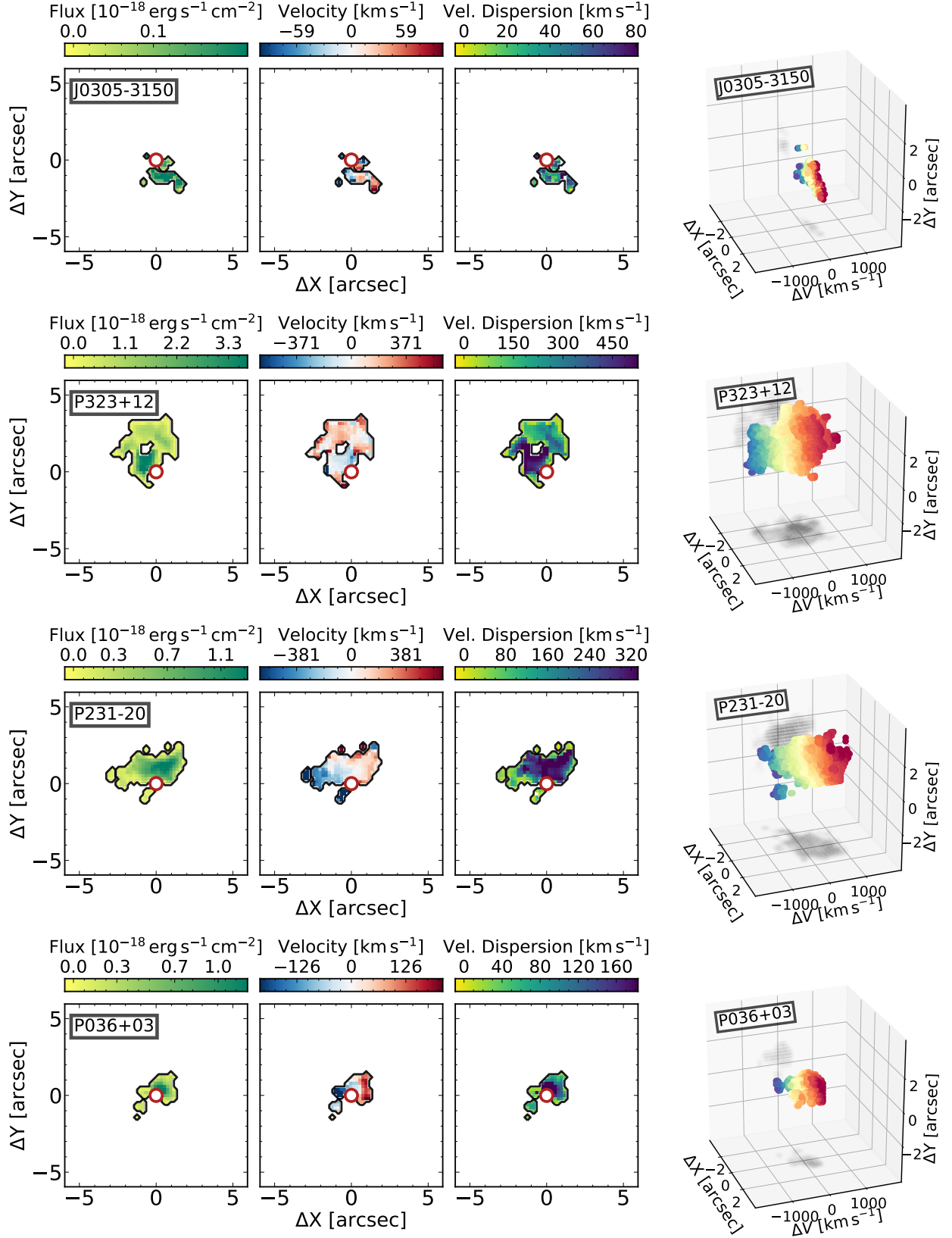
**Figure 4.** Spatially resolved kinematics of the halos detected in our sample. From left to right: integrated flux (zeroth–moment), velocity–field with respect to the flux–weighted centroid of the line emission (first–moment), and velocity dispersion (second–moment). These maps were obtained as described in subsection 4.3. Note that the maps are not corrected for the finite spectral resolution of MUSE. In the wavelength range explored by our sample, this washes away any information with $\sigma \lesssim 35\,\mathrm{km\,s^{-1}}$. The right–most column shows the 3D visualization of each nebula. Here $\Delta X$ goes from East to West, $\Delta Y$ from South to North, and $\Delta V$ from blue to red with respect to the centroid of the extended emission.
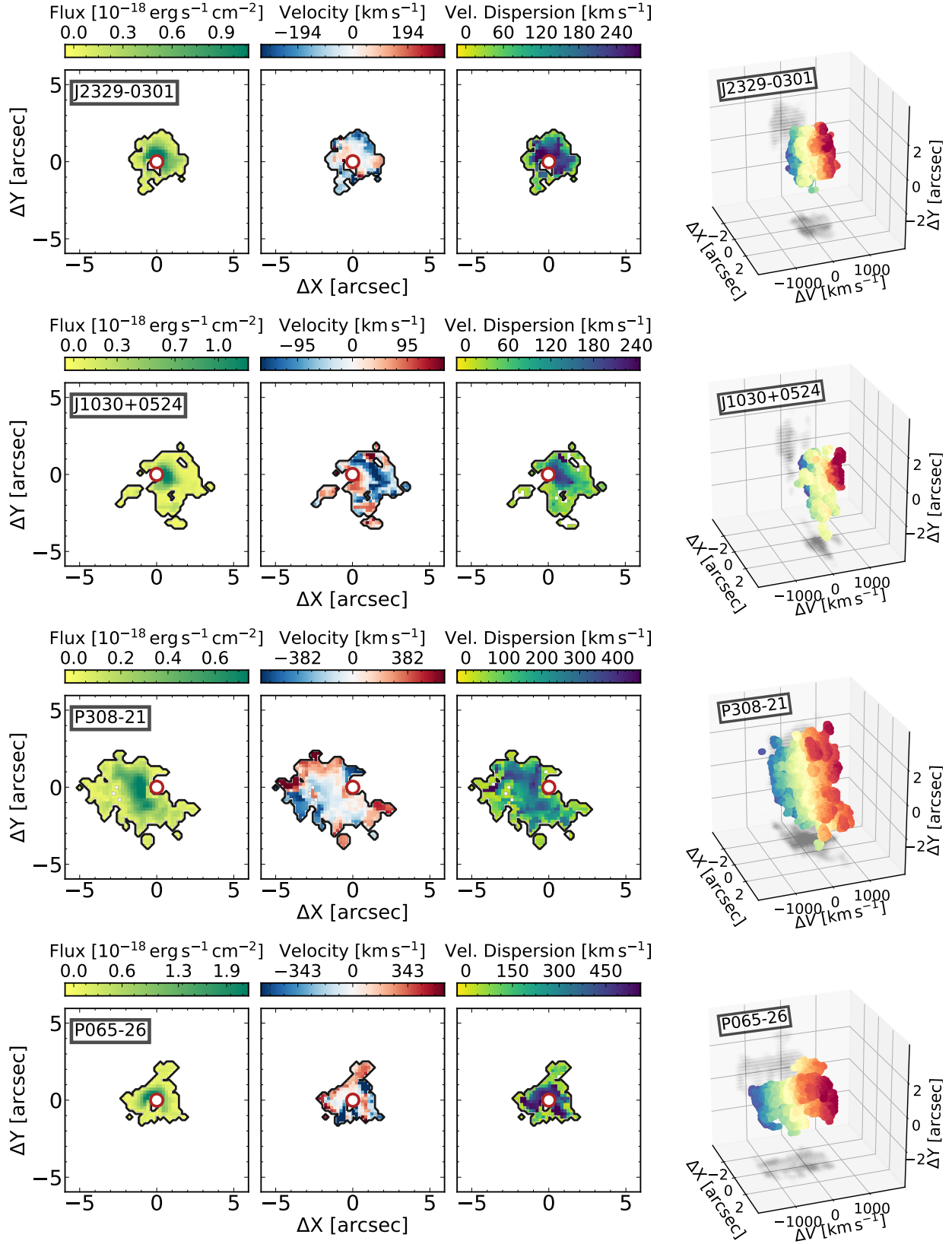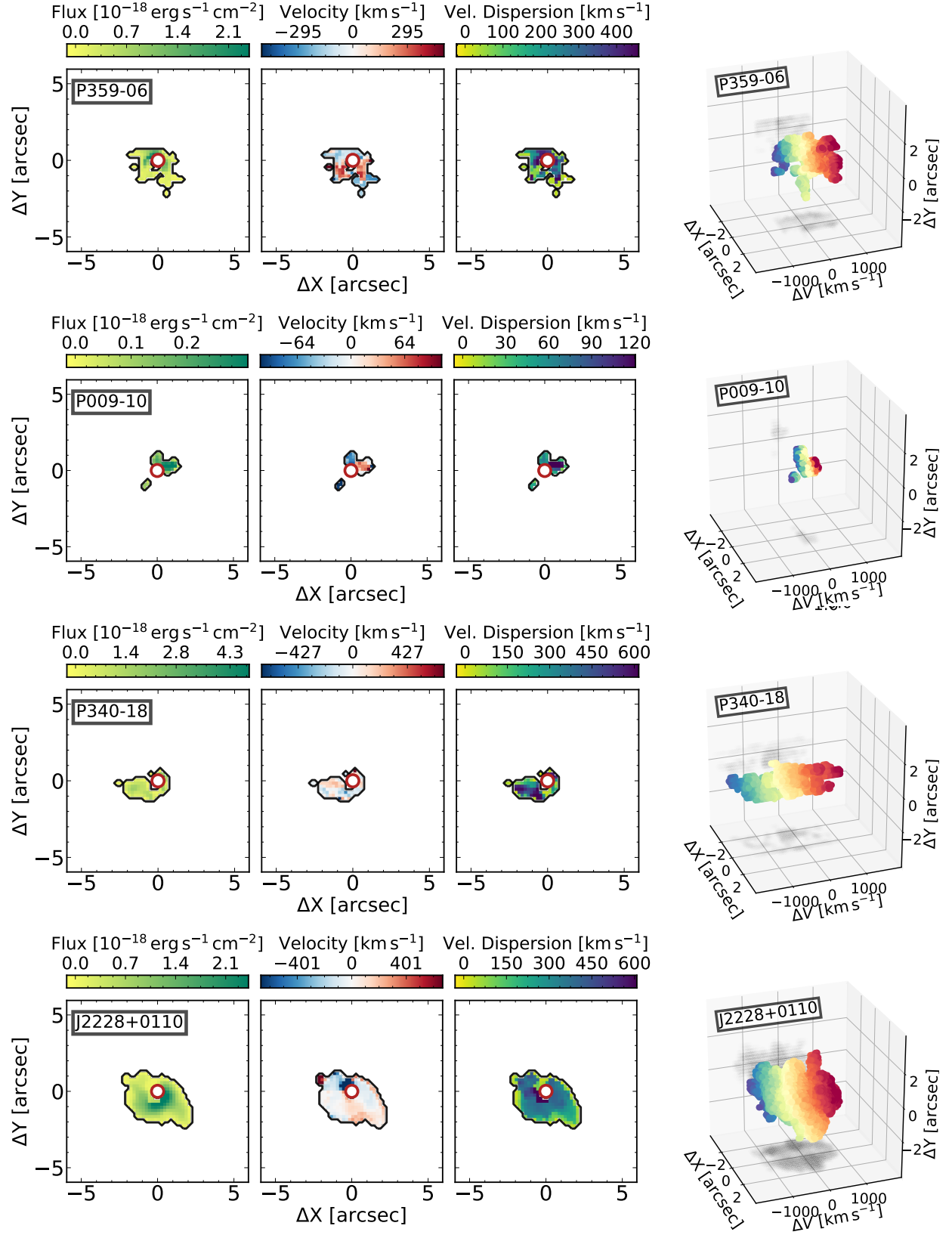
FARINA ET AL.



**Figure 4.** continued.

**Figure 4.** continued.

**Table 3.** Spectral properties of the extended emission.

| ID | $\lambda_{\mathrm{c,Ly}\alpha}$ | $z_{\mathrm{Ly}\alpha}$ | $\mathrm{FWHM}_{\mathrm{Ly}\alpha}$ | $\mathrm{F}_{\mathrm{Ly}\alpha}$ | $\mathrm{L}_{\mathrm{Ly}\alpha}$ |
|---|---|---|---|---|---|
| | (Å) | | $(\mathrm{km\,s}^{-1})$ | $(10^{-17}\,\mathrm{erg\,s}^{-1}\,\mathrm{cm}^{-2})$ | $(10^{43}\,\mathrm{erg\,s}^{-1})$ |
| J0305−3150 | 9259.9±1.0 | 6.6171±0.0008 | 325± 85 | 1.6±0.4 | 0.8±0.2 |
| P323+12 | 9217.2±2.2 | 6.5819±0.0018 | 1385±145 | 40.5±1.2 | 20.1±0.6 |
| P231−20 | 9228.3±1.9 | 6.5911±0.0016 | 1180± 85 | 22.2±0.6 | 11.0±0.3 |
| P036+03 | 9167.5±1.6 | 6.5411±0.0013 | 695± 90 | 7.8±0.4 | 3.8±0.2 |
| J2318−3113 | ⋯ | ⋯ | ⋯ | <0.4 | <0.2 |
| P183+05 | ⋯ | ⋯ | ⋯ | <1.2 | <0.6 |
| J0210−0456 | ⋯ | ⋯ | ⋯ | <0.5 | <0.2 |
| J2329−0301 | 9018.8±1.7 | 6.4188±0.0014 | 830± 60 | 11.0±0.3 | 5.1±0.1 |
| J1152+0055 | ⋯ | ⋯ | ⋯ | <2.1 | <0.9 |
| J2211−3206 | ⋯ | ⋯ | ⋯ | <0.9 | <0.4 |
| J0142−3327 | ⋯ | ⋯ | ⋯ | <0.6 | <0.3 |
| J0100+2802 | ⋯ | ⋯ | ⋯ | <1.0 | <0.5 |
| J1030+0524 | 8880.3±1.5 | 6.3048±0.0012 | 590±120 | 5.6±0.7 | 2.5±0.3 |
| P308−21 | 8803.2±1.7 | 6.2414±0.0014 | 1020± 60 | 20.3±0.7 | 8.8±0.3 |
| P065−26 | 8729.8±2.3 | 6.1810±0.0019 | 1675± 90 | 15.4±0.6 | 6.6±0.2 |
| P359−06 | 8722.8±1.9 | 6.1753±0.0016 | 1160±330 | 7.8±0.4 | 3.3±0.2 |
| J2229+1457 | ⋯ | ⋯ | ⋯ | <0.4 | <0.2 |
| P217−16 | ⋯ | ⋯ | ⋯ | <0.3 | <0.1 |
| J2219+0102 | ⋯ | ⋯ | ⋯ | <0.5 | <0.2 |
| J2318−3029 | ⋯ | ⋯ | ⋯ | <0.3 | <0.1 |
| J1509−1749 | ⋯ | ⋯ | ⋯ | <0.4 | <0.2 |
| J2216−0016 | ⋯ | ⋯ | ⋯ | <0.5 | <0.2 |
| J2100−1715 | ⋯ | ⋯ | ⋯ | <0.2 | <0.1 |
| J2054−0005 | ⋯ | ⋯ | ⋯ | <0.3 | <0.1 |
| P340−18 | 8510.5±2.5 | 6.0007±0.0020 | 1320±155 | 18.8±0.8 | 7.5±0.3 |
| J0055+0146 | ⋯ | ⋯ | ⋯ | <0.3 | <0.1 |
| P009−10 | 8513.8±1.2 | 6.0033±0.0010 | 395± 60 | 2.3±0.2 | 0.9±0.1 |
| P007+04 | ⋯ | ⋯ | ⋯ | <0.5 | <0.2 |
| J2228+0110 | 8388.0±1.7 | 5.8999±0.0014 | 940± 65 | 20.3±0.4 | 7.8±0.1 |
| J1044+0125 | ⋯ | ⋯ | ⋯ | <0.3 | <0.1 |
| J0129−0035 | ⋯ | ⋯ | ⋯ | <0.3 | <0.1 |

NOTE—The reported central wavelengths ($\lambda_{\mathrm{c,Ly}\alpha}$) and FWHMs ($\mathrm{FWHM}_{\mathrm{Ly}\alpha}$) are derived from the spectrum of the nebular emission extracted from the collapsed $\mathrm{MASK}_{\mathrm{x,y,\lambda}}$ as described in subsection 4.1. The total fluxes ($\mathrm{F}_{\mathrm{Ly}\alpha}$) are instead derived from spectra extracted over a circular aperture of radius $d_{\mathrm{QSO}}^{\mathrm{mask}}$. In the cases of non–detections, 3−$\sigma$ limits on fluxes are reported.

Much larger shifts are reported for Lyα nebulosities around intermediate redshift quasars. For instance, Borisova et al. (2016) measured a median shift of $1821\,\mathrm{km\,s^{-1}}$ in a sample of bright $3 \lesssim z \lesssim 4$ quasars. Similarly, in their sample of 61 $z \sim 3$ quasars, Arrigoni Battaia et al. (2019a) reported a large shift between Lyα halos and their best estimates of the quasar systemic redshifts, with a median of $782\,\mathrm{km\,s^{-1}}$. We argue that the discrepancy between intermediate and high redshift halos is related to the large intrinsic uncertainties in the C IV–based systemic redshifts used in Borisova et al. and in Arrigoni Battaia et al. (of the order of $\sim 400\,\mathrm{km\,s^{-1}}$, e.g., Richards et al. 2002; Shen et al. 2016). Indeed, the median shift for the sample of Arrigoni Battaia et al. (2019a) reduces to $144\,\mathrm{km\,s^{-1}}$ when the peak of the broad Lyα line of the $z \sim 3$ quasars themselves is used as a tracer of the systemic redshift. This matches the median shift between the halo and the [C II] $158\,\mu$m redshifts observed in the *REQUIEM* sample.

### 5.1.2. *FWHM of the extended emission*

The right–hand panel of Figure 5 presents the distribution of FWHM of the detected halos with respect to the [C II] $158\,\mu$m lines (FWHM$_{[CII]}$). FWHM$_{Ly\alpha}$ appears to be consistently a factor $> 2\times$ larger than FWHM$_{[CII]}$. This is indeed expected. (Sub–)arcsecond investigation of [C II] $158\,\mu$m emission lines reveled that $z \sim 6$ quasar host–galaxies are compact objects with size of a few kiloparsecs or less (e.g. Wang et al. 2013; Decarli et al. 2018; Venemans et al. 2019; Neeleman et al. 2019), while the extended emission is detected at scales of dozens of kiloparsecs (see Table 2). *Zoom–in* simulations of massive $z > 6$ dark–matter halos hosting quasars show that the deep potential well of stellar component dominates the kinematics in the central regions, while dark matter prevails at $\gtrsim 10$ pkpc (e.g., Dubois et al. 2012; Costa et al. 2015), giving rise to the difference between the velocities of the dense gas component traced by the [C II] $158\,\mu$m and of the cool gas responsible for the Lyα emission. A direct interpretation of this result is, however, not trivial. The resonant nature of the Lyα line and the turbulent motion of the gas due to interactions and feedback effects are likely to contribute to the broadening of the line emission. Moreover, one can speculate that the presence of cool streams, often invoked to replenish the central galaxy with gas, could contribute to the larger observed FWHM (Di Matteo et al. 2012, 2017; Feng et al. 2014). A more detailed investigation of these different possibilities will be provided in Costa et al. (in prep.).

### 5.1.3. *The SFR of the quasar host–galaxies*

It is tempting to explore the possibility that the intense starbursts observed at mm–wavelengths directly influence the powering of the extended Lyα emission. Theoretically, SFR–based Lyα luminosities (L$_{Ly\alpha}^{SFR}$) are expected to follow the linear relation:

$$\frac{\mathrm{L}_{Ly\alpha}^{SFR}}{10^{42}\,\mathrm{erg\,s^{-1}}} = 1.62\frac{\mathrm{SFR}}{\mathrm{M_\odot\,yr^{-1}}}, \qquad (4)$$

for which we assume the Hα calibration relation (e.g., Kennicutt & Evans 2012) and the case B recombination Lyα–to–Hα line ratio. Star formation rates can be derived either from the [C II] $158\,\mu$m emission line or from rest frame far–infrared dust continuum luminosity of the quasar hosts. [C II] $158\,\mu$m estimates, however, depend on the (unknown) dust metallicity, especially in the case of compact starbursts (e.g., De Looze et al. 2014). The dust continuum, on the other hand, can be used to estimate SFRs more directly by assuming that the dust is heated by star formation (i.e., considering that the quasar has a negligible contribution to the observed emission Leipski et al. 2014) and that the dust spectral energy distribution is well parameterized by a modified blackbody with a (typical) temperature of T$_{dust}$ = 47 K and a spectral index of $\beta = 1.6$ (Beelen et al. 2006; Barnett et al. 2015). Conveniently, we detected the rest frame far–infrared dust continuum significantly for all quasars in our sample except J2228+0110. In the following, we will thus consider SFRs based on the dust continuum from Venemans et al. (2018, and references therein). We stress that in high–$z$ quasar host–galaxies, SFRs derived from [C II] $158\,\mu$m and from far–infrared continuum correlate, albeit with a large scatter (see discussion in, e.g., Decarli et al. 2018; Venemans et al. 2018).

Figure 6 shows that Lyα luminosities of the extended emission are broadly independent of the SFRs of the quasar host–galaxies and are typically well below the expectation based on Equation 4 (shown as a green dashed line). The resonant nature of the Lyα line with the large mass in dust present in the host–galaxies (M$_{dust}$ = $10^7 - 10^9$ M$_\odot$, Venemans et al. 2018) are possible processes responsible for the suppression of the Lyα emission (e.g. Kunth et al. 1998; Verhamme et al. 2006; Gronwall et al. 2007; Atek et al. 2008; Sobral, & Matthee 2019; see also Mechtley et al. 2012 for a study of the host galaxy of the $z \sim 6.4$ quasar J1148+5251). The cumulative effect can be quantified by the so–called Lyα escape fraction ($f_{esc,Ly\alpha}$, e.g., Kennicutt & Evans 2012). The median value of $f_{esc,Ly\alpha}$ estimated for our sample is $\lesssim 1\%$. This is an order of magnitude lower than typically reported for $z \sim 6$ LAEs (e.g., Ono et al. 2010; Hayes et al. 2011) but consistent with the most massive, highly star–forming galaxies observed in the 3D–*HST*/CANDELS survey (Oyarzún et al. 2017). However, this value should be considered with some caution. The precise estimate of $f_{esc,Ly\alpha}$ is strongly affected by different properties of the host galaxy (e.g., neutral hydrogen column density, neutral fraction, geometry, gas–to–dust ratio, etc., see Draine 2011; Hennawi & Prochaska 2013; and references therein) and by the *patchiness* of the
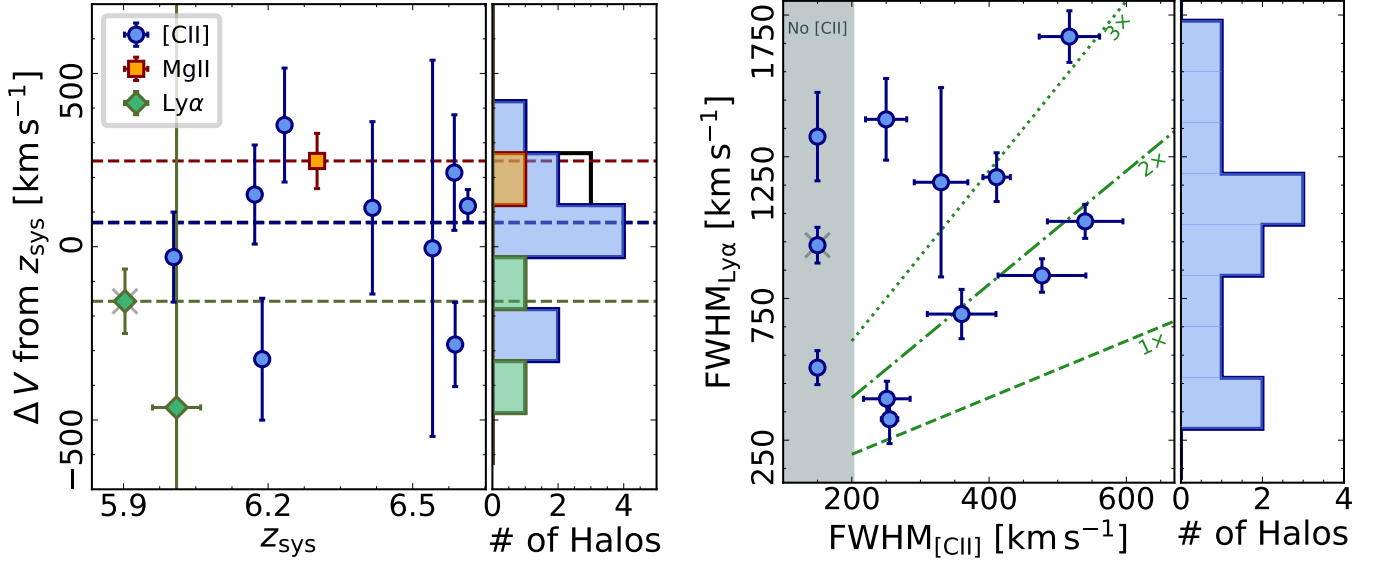
**Figure 5.** *Left Panel* — Velocity difference between the flux–weighted centroid of the nebular emission and the systemic redshift of the quasar (see Equation 3). Different symbols indicate different emission lines used to derive the quasar redshifts (i,e, blue points for [C II] 158 $\mu$m, orange squares for Mg II, and green diamonds for Ly$\alpha$, see Table 1 for details). Horizontal dashed lines indicate the weighted average velocity difference of the different lines. The error–weighted average shift calculated for the entire sample is $\langle \Delta V_{sys} \rangle = (+71 \pm 31)$ km s$^{-1}$. This is shown as a black dashed line that overlaps with the average estimated from the [C II] 158 $\mu$m redshifts only. The histograms on the left–hand side of this panel display the distribution of the shifts color–coded as on the right–hand side. *Right Panel* — Comparison between the FWHM of the detected extended Ly$\alpha$ emission (FWHM$_{Ly\alpha}$) and of the [C II] 158 $\mu$m line arising from the quasar's host–galaxy (FWHM$_{C[II]}$). To guide the eye, green lines mark FWHM$_{Ly\alpha}$ that are 1, 2, and 3$\times$ wider than FWHM$_{C[II]}$. The wide distribution of the FWHM$_{Ly\alpha}$ (ranging from $\sim 250$ km s$^{-1}$ to $\sim 1750$ km s$^{-1}$) is apparent in the histogram on the left–hand side of this panel. In both panels, gray crosses mark targets not part of our *core sample* (see section 2).

dust cocoon (e.g., Casey et al. 2014). In addition, other mechanisms could contribute to the observed Ly$\alpha$ emission, in particular the presence of the strong radiation field generated by the quasar (e.g., Cantalupo et al. 2005; see also subsection 5.3).

### 5.2. *The kinematics of the gas*

In Figure 4 we presented the two dimensional flux–weighted maps of the velocity centroid and dispersion distribution of the extended Ly$\alpha$ emission (see subsection 4.3 for details). In this section, we investigate these resolved kinematics maps in order to identify signatures of ordered motion, in/outflows, rotations, etc. We remind the reader that these maps were computed in a non–parametric way in the regions identified by MASK$_{x,y,\lambda}$, and that velocity shifts are relative to velocity peaks in the extended emission and not to the quasar's systemic redshift.

#### 5.2.1. *Velocity fields*

The relatively low signal–to–noise of the first moment maps (see Figure 4) makes hard to infer the potential presence of ordered motion in the gas. In addition, due to the resonant nature of the Ly$\alpha$ line, the signature of coherent motion could be hindered by radiative transfer effects (e.g., Cantalupo et al. 2005). Indeed, the majority of the halos iden-

tified in the *REQUIEM* survey do not show evidence of rotation, as it was reported in extended Ly$\alpha$ halos at $z \sim 3 - 4$ (Borisova et al. 2016; Arrigoni Battaia et al. 2019a).

A noticeable exception is the nebular emission around the quasar P231$-$20. A velocity gradient can be seen ranging from $-200$ to $+800$ km s$^{-1}$ East to West (see Figure 7). Intriguingly, two [C II] 158 $\mu$m–bright companions located within $\lesssim 14$ kpc from the quasar host galaxy have been discovered (Decarli et al. 2017; Neeleman et al. 2019). Both the velocity shear and the presence of a rich environment are reminiscent of the enormous Ly$\alpha$ nebular emission observed around the quasar SDSS J1020+1040 at $z = 3.2$ by Arrigoni Battaia et al. (2018a) (albeit on a smaller scale). This system is considered a prototype to investigate the feasibility of inspiraling accretion onto a massive galaxy at $z \sim 3$. Indeed, simulations predict that baryons assemble in rotational structures, gaining angular momentum from their dark matters halos (e.g., Hoyle 1951; Fall, & Efstathiou 1980; Mo et al. 1998) and from accretion streams (e.g., Chen et al. 2003; Kereš et al. 2009; Kereš, & Hernquist 2009; Brook et al. 2011; Stewart et al. 2017). In this scenario the cool accreting gas should be able to shape the central galaxy, delivering both fuel for star formation and angular momentum to the central regions (e.g., Sales et al. 2012; Bouché et al. 2013). High res-
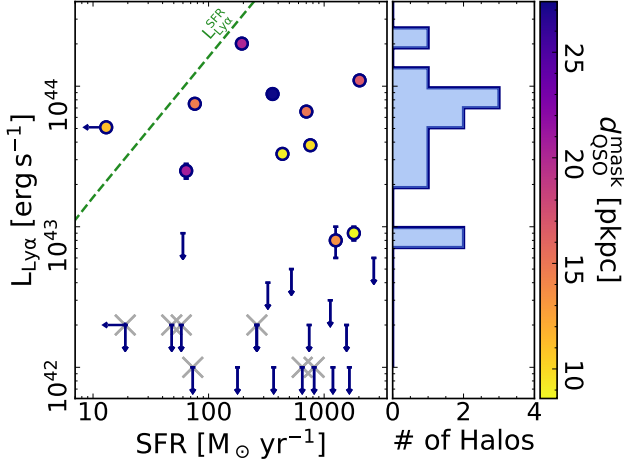
**Figure 6.** Total Lyα luminosity of the extended halos (L$_{\mathrm{Ly}\alpha}$, see Table 3) versus star formation rate derived from the dust continuum emission of the quasar host–galaxies (SFR). 3–σ upper–limits on L$_{\mathrm{Ly}\alpha}$ and on SFR are shown as downward and leftward arrows, respectively. Different colors show the value of $d_{\mathrm{QSO}}^{\mathrm{mask}}$ (see Table 2). The green dashed line indicates the unobscured Lyα emission expected from UV photons generated in intense starbursts, such as detected at mm–wavelengths (Equation 4). Most of the detected halos have L$_{\mathrm{Ly}\alpha}$ below this theoretical prediction. Gray crosses represent quasars that are not part of our *core sample* (see section 2).

olution ($\sim 0\rlap{.}''35$) observations of the [C II] 158 $\mu$m emission of the quasar host galaxy of P231$-$20 does not show a strong signature of rotation (Neeleman et al. 2019). This supports the idea that the system recently underwent a merger event with the close companion galaxy (located at a separation of 9 kpc and $-135\,\mathrm{km\,s^{-1}}$, Decarli et al. 2017; Neeleman et al. 2019) that perturbed the gas distribution.

If one assumes that the gas in the extended halo of P231$-$20 is (at first order) gravitationally bound, it is possible to approximate the dynamical mass of the system as $M_{\mathrm{dyn}} = 1.16 \times 10^{5}\, v_{\mathrm{circ}}\, d$ where $d$ is the diameter of the nebular emission in pkpc and $v_{\mathrm{circ}}$ its circular velocity in $\mathrm{km\,s^{-1}}$. Given that the gas shows ordered motion, $v_{\mathrm{circ}}$ can be expressed as $v_{\mathrm{circ}} = 0.75\,\mathrm{FWHM}_{\mathrm{Ly}\alpha}/\sin i$, with the (unknown) inclination typically considered to be $i = 55°$. This gives us a dynamical mass of $M_{\mathrm{dyn}} \sim 1.5 \times 10^{13}\,\mathrm{M_\odot}$. Albeit the large uncertainties associated with this measurement, the estimated dynamical mass is remarkably similar to the mass predicted for the Lyα emission around the $z = 2.28$ radio–quiet quasar UM287 (Cantalupo et al. 2014)[5]. Martin et al.

---

[5] Estimates of the cool gas mass are strongly dependent on the assumed physical conditions of the gas. Combining photoionization models with sensitive searches for He II and C IV extended emission around UM287 Arrigoni Battaia et al. (2015b) derived extreme gas clumping factors (and thus higher densities) and much lower mass of cool gas present in this nebula: $M_{\mathrm{cool}} \lesssim 6.5 \times 10^{10}\,\mathrm{M_\odot}$.

(2015, 2019) interpreted this emission, which extends out to $\sim$500 kpc, as a large proto–galactic disc. Deeper MUSE observations are however necessary to fully capture the complex kinematics of this system.

The low incidence of clearly rotating structures in our sample is broadly in agreement with results by Dubois et al. (2012) who re–simulated two massive (0.5 and $2.5\times10^{12}\,\mathrm{M_\odot}$) $z \sim 6$ halos. They show that a significant fraction of the gas in the halo can fall almost radially towards the center. The reduced angular momentum inside the virial radius (mostly due to the isotropic distribution of the 0 and to gravitational instabilities and mergers, see also Prieto et al. 2015) allows for efficient funnelling of gas to the central regions of the halos, potentially sustaining the rapid growth of the first supermassive black holes.

### 5.2.2. *Velocity dispersion*

The second–moment maps presented in Figure 4 show that the detected extended Lyα halos have average flux–weighted velocity dispersions ($\langle\sigma_{\mathrm{Ly}\alpha}\rangle$) spanning from $\langle\sigma_{\mathrm{Ly}\alpha}\rangle \sim 30\,\mathrm{km\,s^{-1}}$ to $460\,\mathrm{km\,s^{-1}}$ with an average of $320\pm120\,\mathrm{km\,s^{-1}}$. Note that these values have been corrected for the limited spectral resolution of MUSE according to: $\left(\sigma_{\mathrm{Ly}\alpha}^{\mathrm{corr}}\right)^2 = \left(\sigma_{\mathrm{Ly}\alpha}^{\mathrm{meas.}}\right)^2 - \left(\sigma_{\mathrm{Res.}}^{\lambda}\right)^2$, where $\sigma_{\mathrm{Res.}}^{\lambda} \sim 35\,\mathrm{km\,s^{-1}}$ at the wavelengths explored in our sample. The relatively quiescent $\langle\sigma_{\mathrm{Ly}\alpha}\rangle$ values are consistent with measurements reported by Borisova et al. (2016) and Arrigoni Battaia et al. (2019a) around bright $z \sim 3 - 4$ quasars.

At $z \sim 3.7$ Borisova et al. (2016) reported a larger velocity dispersion ($\langle\sigma_{\mathrm{Ly}\alpha}\rangle > 400\,\mathrm{km\,s^{-1}}$) for a halo around a radio–loud quasar than for halos around radio–quiet quasars. In the *REQUIEM* sample there is one radio–loud quasar, J2228+0110. It shows a flux–weighted velocity dispersion of $(350 \pm 90)\,\mathrm{km\,s^{-1}}$, in agreement with the rest of our (radio–quiet) sample. This dispersion is consistent with Arrigoni Battaia et al. (2019a), who derived similar kinematics for nebulae around radio–loud and radio–quiet quasars at $z \sim 3.2$ [6]

Ginolfi et al. (2018) suggested that the high velocity dispersions observed for the Lyα extended emission around the broad–absorption line quasar J1605$-$0112 at $z = 4.9$ could be linked to an outflow of material escaping the central black hole. Our sample contains only one broad–absorption line quasar (J2216$-$0016) that is 2.9 mag fainter than J1605$-$0112. For this object we do not detect the presence of any significant extended emission. Given the generally quiescent motion of the nebulae in our sample, it is unlikely we are probing fast outflows driven by the quasar (ex-

---

[6] It is worth noting that the radio–loud quasars in both our and Arrigoni Battaia et al. samples are few magnitudes fainter than the one sampled by Borisova et al. (2016).
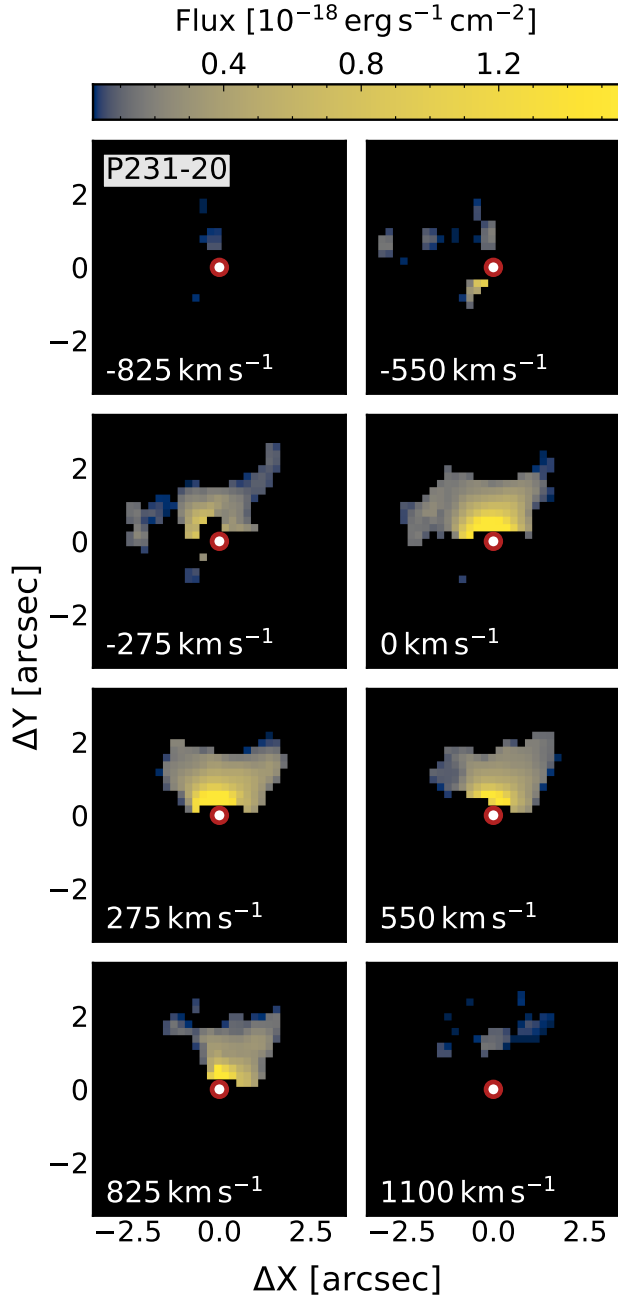
Flux [$10^{-18}$ erg s$^{-1}$ cm$^{-2}$]



**Figure 7.** Velocity field of the extended Ly$\alpha$ nebular emission detected around the quasar P231−20 convolved with a 3D Gaussian kernel with $\sigma_{\rm spat} = 0\farcs2$ in the spatial and $\sigma_{\rm spec} = 2.50\,\text{Å}$ in the spectral direction. Zero velocity is set to the [C II] 158 $\mu$m redshift of the quasar ($z_{\rm sys} = 6.5864 \pm 0.0005$, while in Figure 4 velocity differences are relative to the flux–weighted centroid of the extended emission). The red circle in the center of each image marks the location of the quasar. Only voxels that are part of $\text{MASK}_{\rm x,y,\lambda}$ are shown. $\Delta X$ goes from East to West, $\Delta Y$ from South to North. The bulk of the emission is redshifted with respect to the quasar's systemic redshift, and the nebula shows a velocity gradient going from East to West.

pected to be of the order of $\gtrsim 1000\,\text{km s}^{-1}$, e.g., Tremonti et al. 2007; Villar-Martín 2007; Greene et al. 2012). Nonetheless, we cannot exclude this scenario for the halos associated with the quasars P065−26 and P340−18, where the observed gas velocities are of the order FWHM $\gtrsim 1500\,\text{km s}^{-1}$. Simulations of luminous ($>$ few $\times 10^{46}\,\text{erg s}^{-1}$) quasars indeed predict AGN–driven winds with such large velocities, however these could happen at different scales, from less than 1 kpc to several tens (e.g., Costa et al. 2015; Bieri et al. 2017). However, given the current spatial resolution of our data, we are not sensitive to the presence of extreme kinematics on scales $\lesssim 5$ kpc (where the such an emission would be diluted by the flux of the central AGN).

*Is the gas gravitationally bound to the halo?* Recent observations (both in absorption and in emission) of the gas in the circum–galactic medium of quasars have revealed velocity dispersions consistent with the gravitational motion within dark matter halos with masses $\text{M}_{\rm DM} \gtrsim 10^{12.5}\,\text{M}_\odot$ (e.g., Prochaska, & Hennawi 2009; Lau et al. 2018; Arrigoni Battaia et al. 2019a). These are typical masses of halos hosting quasars, derived from strong quasar–quasar and quasar–galaxy clustering observed out to $z \sim 4$ (e.g., Shen et al. 2007; White et al. 2012; Eftekharzadeh et al. 2015; García-Vergara et al. 2017; Timlin et al. 2018). At $z \sim 6$, however, such a direct measurement still eludes us. Nevertheless, we can gain some insight by comparing the number density of bright quasars and massive dark matter halos (e.g., Shankar et al. 2010), under the assumption that there is a correlation between the luminosity (mass) of a quasar and the mass of the dark matter halo it is embed in (see e.g., Volonteri et al. 2011). By integrating the Kashikawa et al. (2015) luminosity function at $z = 6.3$ (i.e., the average redshift of our survey), we can expect a number density of $\phi\,(\text{M}_{1450} < -25.25) = 2.5 \times 10^{-9}\,\text{Mpc}^{-3}$ for quasars brighter than $\text{M}_{1450} = -25.25$ mag[7]. If we assume a high duty cycle of $f_{\rm duty} = 0.9$ (as predicted by Shankar et al. 2010), we can infer that the integral of the halo mass function from Behroozi et al. (2013) matches the integral of the luminosity function for masses $\text{M}_{\rm DM} \sim 10^{12.8}\,\text{M}_\odot$.

We can now compare this value to the masses derived from the velocity dispersions observed in the detected halos. Indeed, if we assume an NFW (Navarro, Frenk, & White 1997) density profile and the concentration–mass relation presented in Dutton & Macciò (2014)[8], the 1D root–mean–square ve-

---

[7] Note that at these redshifts the quasar luminosity function is not well constrained. For instance, using the luminosity function inferred from a sample of 52 SDSS quasars from Jiang et al. (2016), the number density of $z = 6.3$ quasars is $\phi\,(\text{M}_{1450} < -25.25) = 2.6 \times 10^{-10}\,\text{Mpc}^{-3}$

[8] The Planck cosmology (Planck Collaboration et al. 2014) used in Dutton & Macciò (2014) is different from the one considered in this paper. However, effects of this discrepancy are negligible in the context of our calculations.
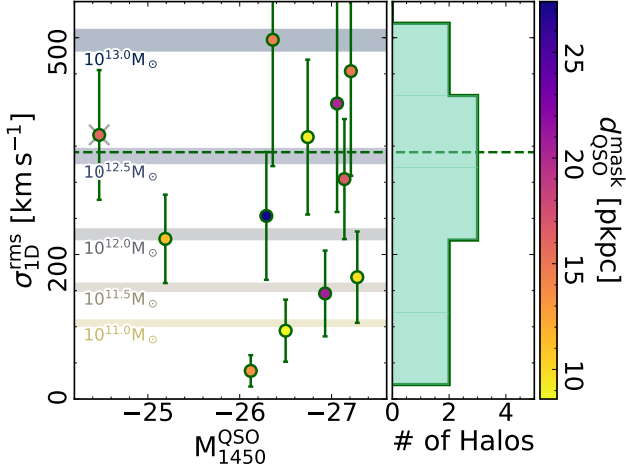
**Figure 8.** 1D root–mean–square velocity dispersion measured in each detected nebulosity ($\sigma_{1D}^{rms}$) versus the monochromatic luminosity of the quasars ($M_{1450}^{QSO}$). Points are color–coded by the size of the recovered halo ($d_{QSO}^{mask}$). Horizontal bands are velocity dispersions expected for NFW dark matter halos with masses ranging from $10^{11}$ to $10^{13}$ M$_\odot$. Lower and upper limits of each band correspond to estimates at $z = 5.9$ and $z = 6.6$, respectively. Despite the large scatter, the average velocity dispersion of the nebulae (plotted as a green dashed line) is consistent with values expected in a $z \sim 6$ dark matter halo of $M_{DM} \sim 10^{12.5}$ M$_\odot$.

locity dispersion ($\sigma_{1D}^{rms}$) can be directly related with the maximum circular velocity ($V_{circ}^{Max}$) as: $\sigma_{1D} = V_{circ}^{Max}/\sqrt{2}$ (Tormen et al. 1997). The average $\sigma_{1D}^{rms}$ in the *REQUIEM* sample is $\langle\sigma_{1D}^{rms}\rangle = (340 \pm 125)\,\mathrm{km\,s^{-1}}$, consistent with the gravitational motion in a $M_{DM} \sim 10^{12.5}$ M$_\odot$ halo at $z = 6$ (see Figure 8). Although most of the detected nebulae are associated with quasars confined to a narrow luminosity range (i.e., between $M_{1450} \sim -26\,\mathrm{mag}$ and $-27.5\,\mathrm{mag}$), no clear dependency between the velocity dispersion of the nebulae and $M_{1450}$ is observed (see Figure 8). This suggests that the mechanisms responsible for the broadening of the Ly$\alpha$ line do not depend on the rest–frame UV emission of the central super–massive black hole.

## 5.3. *The powering mechanism(s) of the extended halos*

The currently favored mechanism to explain the extended emission observed around quasars is *Ly$\alpha$ fluorescence*, i.e., the recombination emission following photoionization of cool ($T \sim 10^4$ K) gas by the strong quasar radiation field (e.g., Hennawi & Prochaska 2013; Arrigoni Battaia et al. 2016, 2019a; Cantalupo 2017). In general, if we assume that quasars are surrounded by a population of cool spherical gas clouds, we can directly infer the surface brightness of the fluorescence emission in two limiting regimes:

*(i)* The gas in the clouds is optically–thick (i.e., with $N_{HI} \gg 10^{17.2}\,\mathrm{cm^{-2}}$). In this case it is able to self–

shield from the quasar's radiation and the Ly$\alpha$ emission originates from a thin, highly ionized envelope around each individual cloud;

*(ii)* The gas is optically thin (i.e., with $N_{HI} \ll 10^{17.2}\,\mathrm{cm^{-2}}$) and it is maintained in a highly ionized state by the quasar radiation. In this case, the Ly$\alpha$ emission originates from the entire volume of each cloud.

In the following we will exploit the formalism presented in Hennawi & Prochaska (2013) to gain insight into the physical status of the gas surrounding the first quasars.

### 5.3.1. *Optically thick scenario*

If the gas is optically thick, the Ly$\alpha$ surface brightness of the extended emission is expected to be proportional to the flux of ionizing photons coming from the central AGN ($\Phi$), to the covering fraction of optically thick clouds ($f_C^{thick}$), and to the fraction of incident photons converted into Ly$\alpha$ by the cloud's envelope ($\eta_{thick}$, see also Hennawi et al. 2015; Farina et al. 2017; Cantalupo 2017):

$$\mathrm{SB}_{Ly\alpha}^{thick} = \frac{\eta_{thick}h\nu_{Ly\alpha}}{4\pi\left(1+z\right)^4}f_C^{thick}\Phi\left(\frac{R}{\sqrt{3}}\right), \qquad (5)$$

where we considered the cool gas clouds to be spatially uniformly distributed in a spherical halo of radius $R$. $\Phi$ can be expressed as a function of the luminosity of the quasar as:

$$\Phi\left(r\right) = \int_{\nu_{LL}}^{\infty}\frac{F_\nu}{h\nu}d\nu = \frac{L_{\nu_{LL}}}{4\pi r^2}\int_{\nu_{LL}}^{\infty}\frac{1}{h\nu}\left(\frac{\nu}{\nu_{LL}}\right)^{\alpha_{UV}}d\nu, \qquad (6)$$

where we considered that, blueward of the Lyman limit ($\nu_{LL}$) the quasar spectral energy distribution has the form $L_\nu = L_{\nu_{LL}}\left(\nu/\nu_{LL}\right)^{\alpha_{UV}}$ with $\alpha_{UV} = -1.7$. The luminosity at the Lyman edge ($L_{\nu_{LL}}$) can be directly derived from $M_{1450}$ as: $M_{912} = M_{1450} + 0.33$ (see Lusso et al. 2015). Considering $\eta_{thick} = 0.66$, we can thus write:

$$\frac{\mathrm{SB}_{Ly\alpha}^{thick}}{10^{-17}\mathrm{erg\,s^{-1}\,cm^{-2}\,arcsec^{-2}}} = 21.0\left(\frac{1+z}{1+6.2}\right)^{-4}\times$$
$$\times\left(\frac{f_C^{thick}}{0.5}\right)\left(\frac{R}{20\,\mathrm{pkpc}}\right)^{-2}\left(\frac{L_{\nu_{LL}}}{10^{31}\,\mathrm{erg\,s^{-1}\,Hz^{-1}}}\right). \qquad (7)$$

Considering that our *core sample* has an average luminosity at the Lyman edge of $\langle L_{\nu_{LL}}\rangle = 2 \times 10^{31}\,\mathrm{erg\,s^{-1}\,Hz}$, the optically thick scenario predicts a surface brightness of $\mathrm{SB}_{Ly\alpha}^{thick} \sim 40 \times 10^{-17}\,\mathrm{erg\,s^{-1}\,cm^{-2}\,arcsec^{-2}}$, i.e. $\gtrsim 2$ orders of magnitude higher than observed (see Figure 9). Despite the presence of unknowns such as the geometry of the quasar emission or the covering fraction of optically thick clouds (that may be of the order of 60% within a projected distance of 200 pkpc from $z \sim 2 - 3$ quasars, e.g. Prochaska et al. 2013a), this discrepancy points to a different scenario

for the origin of the extended Ly$\alpha$ emission. The optically thick regime is also disfavored by the absence of a clear correlation between $\mathrm{SB_{Ly\alpha}}$ and $L_{\nu_{\mathrm{LL}}}$ (and thus $\mathrm{M_{1450}}$) as expected from Equation 7 (see Figure 9).

### 5.3.2. *Optically thin scenario*

If the quasar radiation is sufficiently intense to keep the gas highly ionized (i.e. if the neutral fraction $x_{\mathrm{HI}} = n_{\mathrm{HI}}/n_{\mathrm{H}} \ll 1$), the expected average surface brightness arising from these optically thin clouds is independent of the quasar luminosity and can be expressed as:

$$\frac{\mathrm{SB_{Ly\alpha}^{thin}}}{10^{-19}\,\mathrm{erg\,s^{-1}\,cm^{-2}\,arcsec^{-2}}} = 3.6 \left( \frac{1+z}{1+6.2} \right)^{-4} \times$$
$$\times \left( \frac{f_{\mathrm{C}}^{\mathrm{thin}}}{0.5} \right) \left( \frac{n_{\mathrm{H}}}{1\,\mathrm{cm^{-3}}} \right) \left( \frac{N_{\mathrm{H}}}{10^{20.5}\,\mathrm{cm^{-2}}} \right), \quad (8)$$

where $f_{\mathrm{C}}^{\mathrm{thin}}$ is the covering fraction of optically thin clouds, and $n_{\mathrm{H}}$ and $N_{\mathrm{H}}$ are the cloud's hydrogen volume and column densities, respectively (see Osterbrock, & Ferland 2006; Gould & Weinberg 1996; Hennawi & Prochaska 2013 for further details). Assuming photoionization equilibrium allows us to express the neutral column density averaged over the area of the halo ($\langle N_{\mathrm{HI}} \rangle$) in terms of $L_{\nu_{\mathrm{LL}}}$ and $L_{\mathrm{Ly\alpha}}$:

$$\frac{\langle N_{\mathrm{HI}} \rangle}{10^{17.2}\,\mathrm{cm^{-2}}} = 0.1 \left( \frac{L_{\mathrm{Ly\alpha}}}{10^{44}\,\mathrm{erg\,s^{-1}}} \right) \times$$
$$\times \left( \frac{L_{\nu_{\mathrm{LL}}}}{10^{31}\,\mathrm{erg\,s^{-1}\,Hz^{-1}}} \right)^{-1}. \quad (9)$$

Given the observed luminosities of the nebulae in our core sample ($L_{\mathrm{Ly\alpha}} \lesssim 10^{44}\,\mathrm{erg\,s^{-1}}$, see Table 3) we obtain $\langle N_{\mathrm{HI}} \rangle \ll 10^{17.2}\,\mathrm{cm^{-2}}$, consistent with the optically thin regime. However, we stress that $\langle N_{\mathrm{HI}} \rangle$ is obtained by averaging over the whole area of the halo. So, while $\langle N_{\mathrm{HI}} \rangle \gg 10^{17.2}\,\mathrm{cm^{-2}}$ definitively determines the clouds to be optically thick, a small value of $\langle N_{\mathrm{HI}} \rangle$ does not provide the same clear result, since individual clouds may still be optically thick while being surrounded by a thinner medium.

Under the assumption that the clouds are optically thin, it is of interest to use Equation 8 to derive constraints on the gas volume density ($n_{\mathrm{H}}$). Studies of absorption systems associated with gas surrounding $z \sim 2$ quasars suggest that $N_{\mathrm{H}}$ is almost constant within an impact parameter 200 pkpc at a median value of $N_{\mathrm{H}} = 10^{20.5}\,\mathrm{cm^{-2}}$ (e.g. Lau et al. 2016). If $z \sim 6$ quasars are embedded in halos with similar hydrogen column densities, our observations imply $n_{\mathrm{H}} > 1\,\mathrm{cm^{-3}}$. Intriguingly, similarly high gas densities have been invoked to explain the Ly$\alpha$ emission in giant nebulae discovered around $z \sim 2 - 3$ quasars (Cantalupo et al. 2014; Hennawi et al. 2015; Arrigoni Battaia et al. 2015b, 2018a; Cai et al. 2018).

### 5.3.3. *Other possibilities*

In addition, other mechanisms have been proposed to explain the presence of extended Ly$\alpha$ nebulae including gravitational cooling radiation (e.g., Haiman et al. 2000; Fardal et al. 2001; Furlanetto et al. 2005; Dijkstra, & Loeb 2009), shocks powered by outflows (e.g., Taniguchi, & Shioya 2000; Mori et al. 2004), or resonant scattering of Ly$\alpha$ photons (e.g. Gould & Weinberg 1996; Dijkstra, & Loeb 2008).

However, Ly$\alpha$ emission coefficients for collisional excitation are exponentially dependent on the temperature (Osterbrock, & Ferland 2006). The concurrence of a very narrow density and temperature range for all the gas in every observed Ly$\alpha$ nebula would thus be necessary to validate this. Instead, recombination radiation has a much weaker dependence on temperature (Osterbrock, & Ferland 2006), providing a more natural explanation for the Ly$\alpha$ extended emission in the presence of a strong ionizing flux (e.g., Borisova et al. 2016). In addition, the relatively quiescent motion of the gas in the detected halos (see subsection 5.2) is not easily reconciled with shock–powered emission (see also discussion in Arrigoni Battaia et al. 2019a).

On the other hand, resonant scattering of Ly$\alpha$ photons from the central AGNs and from young stars in the host galaxies can provide a relevant contribution to the emission, if the gas is optically thick at the Ly$\alpha$ transition ($N_{\mathrm{HI}} \gtrsim 10^{14}\,\mathrm{cm^{-2}}$). This was proposed as the main process powering the extended Ly$\alpha$ emission detected around $3 \lesssim z \lesssim 6$ Ly$\alpha$ emitters by Wisotzki et al. (2016). Hennawi & Prochaska (2013) showed that the surface brightness of extended Ly$\alpha$ emission produced via resonant scattering by neutral gas in the CGM ($\mathrm{SB_{Ly\alpha}^{scatt.}}$) is expected to be directly proportional to the flux of ionizing photons emitted close to the Ly$\alpha$ resonance ($L_{\nu_{\mathrm{Ly\alpha}}}$). Given that the peak of the Ly$\alpha$ line of $z \sim 6$ quasars is typically absorbed by neutral hydrogen, there is no direct way to test for the presence of such a correlation in the *REQUIEM* survey. In any case, Arrigoni Battaia et al. (2019a) reported the lack of significant correlation between the surface brightness of Ly$\alpha$ halos and the luminosity of the peak of the Ly$\alpha$ line of $z \sim 3$ quasars.

We stress that all the aforementioned mechanisms can be in place at the same time and contribute at different levels to the observed emission. Additional factors can also modulate the total luminosity of the halos. For instance, the presence of dust on scales larger than 20 kpc (e.g. Roussel et al. 2010; Ménard et al. 2010) can destroy Ly$\alpha$ photons, and/or the variability of the quasar emission (e.g., MacLeod et al. 2012; Yang et al. 2019) can be faster than the response of the halo (with a strong dependence on $n_{\mathrm{H}}$) and wash out some of the expected correlations. Future observations of non–resonant lines such as He II or H$\alpha$ will be instrumental in disentangling different emission mechanisms (e.g. Arrigoni Battaia et al. 2015b; Leibler et al. 2018; Cantalupo et al.

2019). This is particularly challenging at $z > 6$, where only space–based observations will have the sensitivity necessary to provide additional information about the gas surrounding the first quasars.

### 5.4. *Lyα nebulae and galaxy overdensities*

Several giant Lyα nebulae extending on scales $\gg 100$ kpc have recently been reported in the literature (Cantalupo et al. 2014; Hennawi et al. 2015; Cai et al. 2018; Arrigoni Battaia et al. 2018a, 2019b; Lusso et al. 2019). The incidence of such large nebulae has been estimated to be of the order of few percent at $z \sim 2 - 3$ (Hennawi & Prochaska 2013; Arrigoni Battaia et al. 2016, 2019a). A larger sample of $z \gtrsim 6$ quasars is necessary to assess if this low occurrence holds at high redshifts. In any case, all $z < 4$ giant nebulae appear to be invariably associated with overdensities of AGN and galaxies, suggesting a connection between proto–cluster structures and extremely extended emission (e.g., Hennawi et al. 2015; Arrigoni Battaia et al. 2018b). We can qualitatively test this scenario at $z > 6$, by searching for peculiarities in the nebulae associated with quasars for which deep ALMA observations have revealed the presence of bright [C II] 158 $\mu$m companions (i.e., J0305−3150, P231−20, P308−21, and J2100−1715; see section 2 and Decarli et al. 2017; Willott et al. 2017; Venemans et al. 2019). J2100−1715 has a [C II] 158 $\mu$m companion located at a separation of $\sim 60$ kpc (Decarli et al. 2017; Neeleman et al. 2019) but does not show the presence of any significant extended Lyα emission. J0305−3150, although located in an overdensity with three [C II] 158 $\mu$m and one LAE emitter (Farina et al. 2017; Venemans et al. 2019), shows a really faint halo. Finally, P231−20 and P308−21 host among the brightest and most extended halos in the *REQUIEM* survey and both are in the middle of gravitational interactions with their companions (Decarli et al. 2019; Neeleman et al. 2019)[9]. The variety of the Lyα emission observed in this (small) sample of quasars with companions suggests that at $z > 6$, bright and extended Lyα halos may be associated with ongoing merger events. If this is the case, P323+12, that exhibits the brightest nebular emission in our sample, is likely to be in a gravitational interaction. Mazzucchelli et al. (2017) presented low resolution *NOEMA* observations on the [C II] 158 $\mu$m emission line of this source, without detecting a merger. However testing the merger scenario requires a higher sensitivity and better spatial resolution, for example with *ALMA* or *NOEMA*.

### 5.5. *The average surface–brightness profile*

In this section we will infer the average surface brightness profile of the Lyα emission around quasars in the *REQUIEM* survey and we will compare its shape with lower redshift studies. To avoid selection effects, we will focus only on our *core sample*. We remind the reader that this consists of 23 radio–quiet quasars at an average redshift of $\langle z \rangle = 6.27$ and with an average absolute magnitude of $\langle M_{1450} \rangle = -27.1$ mag (see section 2). As a lower redshift comparison we will use the study performed by Arrigoni Battaia et al. (2019a) on a sample of 61 quasars at $3.03 < z < 3.46$ (with an average of $\langle z \rangle = 3.21$) and with magnitudes in the range $-28.3$ mag $< M_{1450} < -25.6$ mag (with an average close to our sample: $\langle M_{1450} \rangle = -27.3$ mag).

The extended nebulae detected in the *REQUIEM* survey appear to have complex morphologies and clear asymmetries (see Figure 2). We proceeded following the standard approach in the literature and we obtained the surface brightness profiles averaging over circular apertures centered on the location of the quasars. As explained in subsection 4.2, single profiles were extracted from pseudo–narrow band images created by collapsing the datacubes over 30 Å centered at the location of the Lyα line, redshifted to the quasar's systemic redshift. To create the stacked profile, we first correct these profiles for cosmological dimming (i.e., by a factor $(1 + z)^4$) and then we average over them with equal weights. This prevents the introduction of biases towards deeper exposures and/or brighter objects. We also create the stacked profile only using the sub–sample of quasars for which an extended emission has been detected with significance. The results of this procedure are plotted in Figure 10, where the average surface brightness profile obtained for all quasars is shown as orange triangles and the one from quasars embedded in halos as purple circles. For comparison, the average profile from Arrigoni Battaia et al. (2019a) is displayed as a cyan solid line.

In order to extract information from the stacked profiles, we perform a fit with an exponential function: $(1 + z)^4 \, \mathrm{SB}_{\mathrm{Ly}\alpha}(r) = C \exp(-r/r_h)$, where $C$ is the normalization and $r_h$ is the scale length of the profile. The resulting parameters are $C = (3.0 \pm 0.4) \times 10^{-14} \, \mathrm{erg \, s^{-1} \, cm^{-2} \, arcsec^{-2}}$ and $r_h = (9.4 \pm 0.8)$ kpc for the full sample and $C = (5.6 \pm 0.8) \times 10^{-14} \, \mathrm{erg \, s^{-1} \, cm^{-2} \, arcsec^{-2}}$ and $r_h = (6.4 \pm 0.3)$ kpc for the stack quasars with detected halos. As expected, while the two profile match within the errors, the latter appears slightly more concentrated due to the stronger signal in the central $\sim 20$ kpc. In the following, we will keep showing both profiles, however in the discussion we will focus solely on the one that includes all quasars as it is more representative of the full high–$z$ quasar population.

The scale length derived for $z \sim 6.2$ quasars is a factor of $\sim 5\times$ smaller than the $r_h = (15.5 \times 0.5)$ kpc measured for $z \sim 3.2$ radio–quiet quasars by Arrigoni Battaia et al.

---

[9] We note that for all these quasars MUSE observations have been gathered with integration times $> 3\times$ longer than the median of our sample (see Table 1).
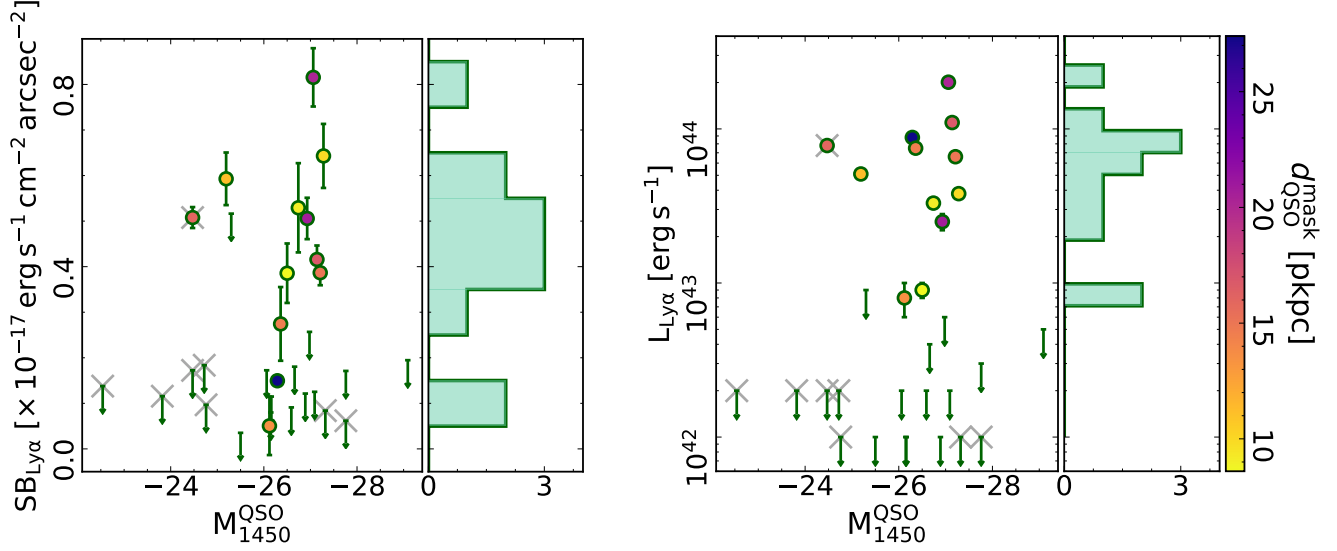
**Figure 9.** *Left Panel* — Average surface brightness versus $M_{1450}$. $3-\sigma$ upper–limits for non–detected nebulae are shown as downward arrows. The colormap of the points is the same as in Figure 6. For consistency with subsection 4.2, here the average $SB_{Ly\alpha}$ is calculated using a circular aperture of radius $d_{QSO}^{mask}$ (or 20 pkpc if the halo was not detected) on pseudo–narrow–band images obtained collapsing the datacube between $\pm 500 \, \text{km} \, \text{s}^{-1}$ relative to the quasar's systemic redshift. Targets not part of our *core sample* are marked with gray crosses (see section 2). *Right Panel* — Same as the left panel but with the total Ly$\alpha$ luminosity of the extended halo as $y$–axis.

(2019a), suggesting that extended halos are more compact at higher redshift. Coincidentally, a similar scale length was reported for the extended emission around $z > 5$ Ly$\alpha$ emitters in the *Hubble* Ultra Deep Field ($r_h = 3.8 \pm 1.3$ kpc, Leclercq et al. 2017). However, we should note that, given the relative apparent emission of the quasars and the factor $\sim 8\times$ in sensitivity due to redshift dimming, our observations are more sensitive to regions closer to the quasar while Arrigoni Battaia et al. (2019a) is sensitive to more extended emission. If we take the expansion of the Universe into account, the difference between the $z \sim 6.2$ and the $z \sim 3.2$ profiles is less exacerbated and halos appear to be intrinsically brighter moving to higher redshifts (see Figure 10). A strong evolution of the average properties of the extended emission with cosmic time was reported by Arrigoni Battaia et al. (2019a) based on a comparison between their sample at $z \sim 3.2$ and the results obtained from a narrow–band survey of bright radio–quiet quasars at $z \sim 2.2$ (Arrigoni Battaia et al. 2016). The authors reinforce their results by splitting their sample into $z \sim 3.1$ and $z \sim 3.3$ sub–samples and showing that the evolutionary trend remains consistent. In the following, we will test their evolutionary prediction out to the redshifts provided by the *REQUIEM* survey. For the sake of simplicity, we will consider that dark matter halos hosting quasars are hosted by massive halos with $M_{DM} = 10^{12.5} \, \text{M}_\odot$ independent of their redshift. In Figure 11 we show the average surface brightness profiles at $z = 6.28$, $3.34$, and $3.11$ normalized by the virial radius: $R_{vir}(z) = [3M_{DM}/4\pi\rho_c(z)]^{\frac{1}{3}}$ with $\rho_c(z)$ the critical density of the Universe at the each

given redshift. For the considered halo, the virial radius thus increases of a factor $\sim 1.7\times$ from $z = 6.28$ to $z = 3.21$. At both these redshifts, the emitting gas appears to be located well within $R_{vir}$, with an emission that is slightly brighter (but consistent within the scatter) in the inner part of $z \sim 6$ halos. If we model the profiles with an exponential function: $(1 + z)^4 \, SB_{Ly\alpha}(r) = C_h \exp(-x/x_h)$ with $C_h$ and $x_h$ as free parameters and $x = r/R_{vir}$, we obtain: $C_h = (3.0 \pm 0.4) \times 10^{-14} \, \text{erg} \, \text{s}^{-1} \, \text{cm}^{-2} \, \text{arcsec}^{-2}$ and $x_h = (0.15 \pm 0.01)$ for the full quasar sample and $C_h = (5.6 \pm 0.8) \times 10^{-14} \, \text{erg} \, \text{s}^{-1} \, \text{cm}^{-2} \, \text{arcsec}^{-2}$ and $x_h = (0.13 \pm 0.01)$ kpc for the sub–sample of detected halos. This value matches the values $x_h = 0.16$ and $x_h = 0.15$ reported by Arrigoni Battaia et al. (2019a) at $z \sim 3.34$ and $z \sim 3.11$, respectively. For a comparison, in Figure 11 we also show the expected average profile of the extended emission if the increase of the normalization observed between $z \sim 3.11$ and $z \sim 3.34$ would keep its pace linearly with redshift up to $z \sim 6.28$. The observed profile consistently lies below this prediction. This suggests a scenario where the (average properties of the) extended Ly$\alpha$ emission mirrors the cosmic evolution of the dark matter halos they reside in (see also subsection 5.2).

Intriguingly, hydrodynamical cosmological simulations show that high–$z$ galaxies in dark matter halos of $M_{DM} \gtrsim 10^{12} \, \text{M}_\odot$ are mainly fed by cool gas streams (co–existing with a hot, shocked medium) down to redshift $z \sim 2 - 3$. Below this "critical" redshift, these cool streams are not able to balance the virial shock–heating and are suppressed
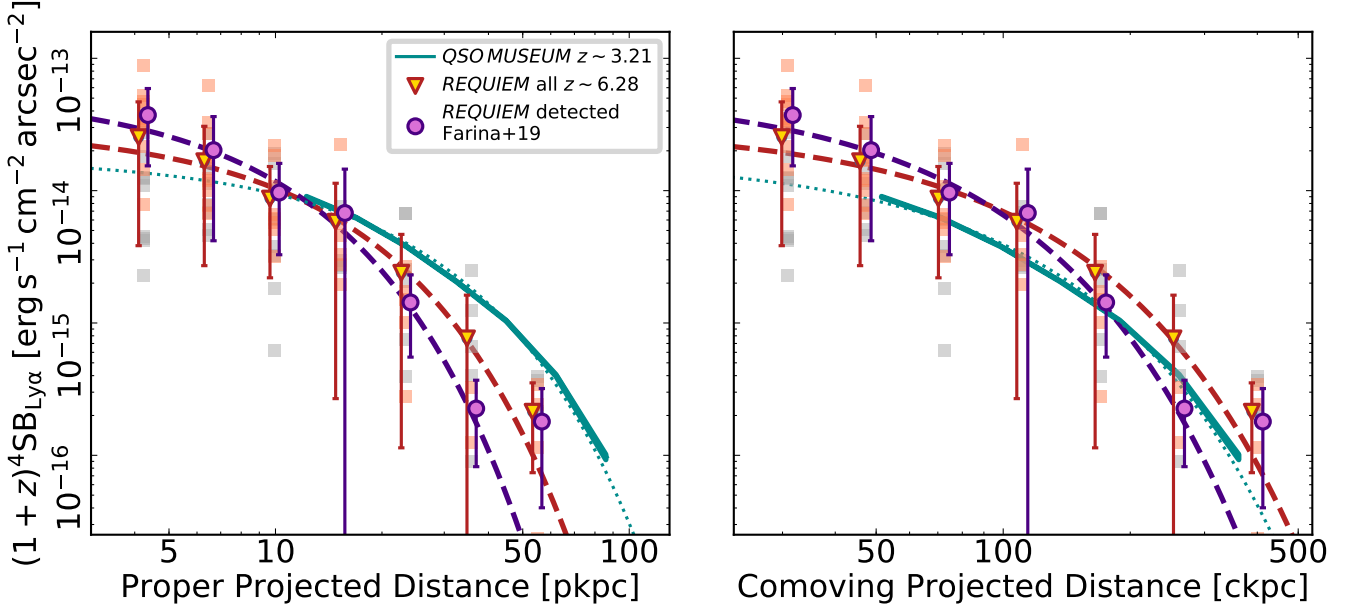
**Figure 10.** Average Lyα surface brightness profile of the *core sample* of our *REQUIEM* survey. *Left Panel —* We show the individual circularly–averaged profiles extracted around each quasar as orange squares for detected halos and gray squares for non–detections. Sum–averaged profiles considering all quasars (orange triangles) or only significantly detected halos (purple circles) are also shown, together with their respective best exponential fit (orange and purple dashed lines). Data–points have been slightly shifted along the $x$–axis for the sake of clarity. The average surface brightness profile of the extended emission around the 61 quasars investigated by Arrigoni Battaia et al. (2019a) is plotted as a solid blue line, together with the exponential best fit (dotted line). Note that all measurements are corrected for the $(1 + z)^4$ factor to compensate for cosmological dimming. *Right Panel —* Same as the left panel but in comoving units.

(e.g., Dekel, & Birnboim 2006; Dekel et al. 2009, 2019). This theoretical picture would naturally explain the observed evolution of the surface brightness profile. Under the assumption that the emission arises from optically thin clouds of gas, the surface brightness is expected to scale as: $\mathrm{SB_{Ly\alpha}} \propto (1 + z)^4 f_C^{\mathrm{thin}} n_H N_H$ and $N_H$ is proportional to the total mass in cool gas $M_{\mathrm{cool}}$ (see subsection 5.3 and Hennawi & Prochaska 2013; Arrigoni Battaia et al. 2019a). Thus, the small variation in Lyα surface brightness reported between $z \sim 6$ and $z \sim 3$ suggests that cool streams are able to replenish the CGM with gas, permitting $M_{\mathrm{cool}}$ to keep pace with $M_{\mathrm{DM}}$. The consequent heating of massive halos at $z \lesssim 3$ may be responsible for the drop of cool gas in the CGM and, thus, of the average Lyα emission. However, this picture clashes with the large amount of cool gas revealed by absorption studies of the CGM around $0.5 \lesssim z \lesssim 2$ quasars (e.g., Bowen et al. 2006; Farina et al. 2013, 2014; Prochaska et al. 2014; Johnson et al. 2015). In addition, we are cautious about the interpretation of the low surface brightness level provided by Arrigoni Battaia et al. (2016). Indeed, this study is based on narrow–band imaging that could led on an underestimate of the total nebular emission (see Discussion in Borisova et al. 2016). Future IFS observations of the Lyα emission of $z \sim 2$ quasars are necessary to confirm the rapid

evolution of the CGM observed between $z \sim 3$ and $z \sim 2$ after a much stable behavior at higher redshift.

### 5.6. *Extended emission and quasar near zones*

Near the end of the cosmic reionization epoch, the large fraction of neutral hydrogen present in the Universe suppresses virtually all the emission blueward of the Lyα line (e.g., Gunn & Peterson 1965). However, the intense radiation of luminous quasars is able to ionize the surrounding gas, creating bubbles of enhanced transmission in their immediate vicinity, called quasars proximity zones (e.g., Cen, & Haiman 2000; Madau, & Rees 2000; Haiman, & Cen 2001). The size of these ionized regions is given by:

$$R_{\mathrm{p}} = \left( \frac{3 \dot{N}_{\mathrm{ion}} t_{\mathrm{QSO}}}{4\pi n_H x_{\mathrm{HI}}} \right)^{\frac{1}{3}}, \qquad (10)$$

where $\dot{N}_{\mathrm{ion}}$ is the emission rate of the ionizing photons and $t_{\mathrm{QSO}}$ is the age of the quasars. For $t_{\mathrm{QSO}} \gtrsim 10^6$ yr, proximity zones can reach sizes of a few proper megaparsecs (Fan et al. 2006; Carilli et al. 2010; Venemans et al. 2015). These scales are much larger than the one probed by the extended Lyα emission around quasars (typically $\lesssim 100$ kpc). Thus, proximity zones are expected to be sensitive to the status of the IGM more than to the quasar's CGM (e.g., Fan et al. 2006). However, it has been shown that the dependence of Equa-
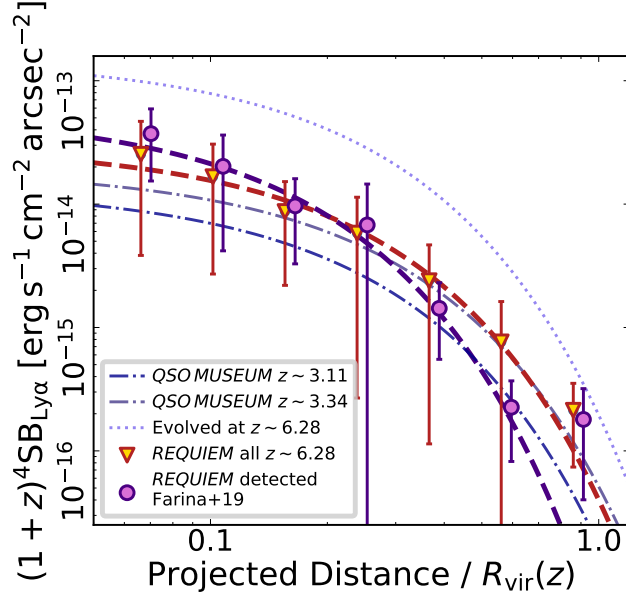
**Figure 11.** Average surface brightness profiles of the extended emission around quasars with the radius normalized to the virial radius $R_{vir}(z)$ of a $10^{12.5}\,M_{\odot}$ dark matter halo located at different redshifts. The color code of the data–points for the *REQUIEM* survey are the same as in Figure 10. The exponential fit of the surface brightness profiles of the halos investigated by Arrigoni Battaia et al. (2019a) split in two sub–samples with median redshifts $z = 3.11$ and $z = 3.34$ are plotted as dash–dotted lines. The dotted purple line shows the expected profile if the evolutionary trend observed between $z = 3.11$ and $z = 3.34$ is extrapolated linearly in redshift to a value of $z \sim 6.28$.

tion 10 on $\dot{N}_{\mathrm{ion}}$ could be removed by re–scaling the size of the near zones by a factor proportional to the absolute magnitude of the quasar: $R_{\mathrm{p}}^{\mathrm{corr}} = R_{\mathrm{p}} \times 10^{-0.4(-27.0-M_{1450})/2.35}$ (e.g., Bolton, & Haehnelt 2007; Eilers et al. 2017). The size of these corrected near zones ($R_{\mathrm{p}}^{\mathrm{corr}}$) is thus sensitive to $t_{\mathrm{QSO}}$ if the surrounding gas has not yet reached the ionization equilibrium (i.e., for quasar ages $t_{\mathrm{QSO}} \lesssim 10^5$ yr, see Eilers et al. 2018 and Davies et al. 2019b for further details). Eilers et al. (2017, 2018) discovered the existence of quasars with exceptionally small proximity zones implying that these objects have been shining for $t_{\mathrm{QSO}} \lesssim 10^5$ yr. Interestingly, this value is comparable to the light crossing time given the size of the nebulae observed in our survey: $t_{\mathrm{cross}} = d_{\mathrm{QSO}}/c \sim 3 \times 10^4$ yr for $d_{\mathrm{QSO}} = 10$ pkpc. This suggests that if a quasar in our sample has a peculiarly small $R_{\mathrm{p}}^{\mathrm{corr}}$, then its extended emission should also be small or not–existent. We remind the reader that the recombination time scales as $t_{\mathrm{rec}} = 1/n_e \alpha_A$ where the electron density can be calculated as $n_e = n_{\mathrm{H}}(1 + Y/2X)$ (assuming that all helium is doubly ionized) and the case A recombination coefficient evaluated at $T = 10^5$ K is $\alpha_A = 4.2 \times 10^{-13}$ cm$^{-3}$ s$^{-1}$ (Osterbrock, & Ferland 2006). Thus, for the volume densi-

ties inferred in subsection 5.3, we obtain values of $t_{\mathrm{rec}}$ much longer than a Hubble time. This means that intermittent quasar activity could lead to the presence of an extended Ly$\alpha$ halo even for a quasar at the beginning of an active phase.

Our targets overlap with the Eilers et al. (2017) sample in five quasars: J0100+2802, J2329−0301, J1030+0524, J2229+1457, and J2054−0005, three of which are young quasar candidates: J2229+1457 [$R_{\mathrm{p}}^{\mathrm{corr}} = (1.07 \pm 0.33)$ pMpc], J2216−0016 [$R_{\mathrm{p}}^{\mathrm{corr}} = (2.19 \pm 0.49)$ pMpc], and J0100+2802 [$R_{\mathrm{p}}^{\mathrm{corr}} = (3.18 \pm 0.06)$ pMpc]. It is alluring that none of these quasars show an extended Ly$\alpha$ halo. Deeper MUSE observations complemented with sensitive NIR spectroscopy aimed to confirm the true nature of these small zones (e.g., Eilers et al. 2018) will provide new information on the nature of this class of objects (Eilers et al. in prep.).

### 5.7. *Is the halo around P323+12 lensed?*

The procedure to find and remove low–redshift contaminants described in section 4 revealed the presence of a galaxy located within the bright halo detected in association with the quasar P323+12, i.e. at RA$_{\mathrm{J2000}}$=21:32:33.22 and Dec.$_{\mathrm{J2000}}$=+12:17:56.8 (see Figure 12). This galaxy is spatially resolved in deep near–infrared imaging collected with *LBT*/LUCI2+ARGOS (see Appendix C). The detection of the Ca H&K $\lambda\lambda 3969,3934$ (hereafter Ca HK, see Figure 12) in the galaxy spectrum determined its redshift at $z_{\mathrm{gal}} = 0.711 \pm 0.001$. In the following we check the possibility that this galaxy could act as a lens and thus enhance the total luminosity observed for this halo.

The expected radius of the Einstein ring ($\theta_{\mathrm{E}}$) can be estimated by assuming the potential well of the galaxy is well described by a singular isothermal sphere (SIS). This allows us to directly relate $\theta_{\mathrm{E}}$ to the velocity dispersion of the SIS ($\sigma_{\mathrm{SIS}}$), to the angular diameter distance between the halo and the lens ($D_{\mathrm{LH}}$), and to the angular diameter distance between the halo and the observer ($D_{\mathrm{H}}$, e.g, Narayan & Schneider 1990; Peacock 1999; Chieregato et al. 2007):

$$\theta_{\mathrm{E}} = 4\pi \left(\frac{\sigma_{\mathrm{SIS}}}{c}\right)^2 \frac{D_{\mathrm{LH}}}{D_{\mathrm{H}}} \qquad (11)$$

Given the relatively low $S/N$ per pixel and spectral resolution (i.e. $R = \lambda/\Delta\lambda \sim 2700$ at $\sim 6800$ Å) of the spectrum in our data, we assume that $\sigma_{\mathrm{SIS}} = \sigma_{\star}$ (i.e. the velocity dispersion of the galaxy) and we infer $\sigma_{\star}$ from the Faber–Jackson relation (Faber & Jackson 1976). Using the updated relation from Nigoche-Netro et al. (2010), a galaxy with an $r$–band absolute magnitude of $M_r = -20.44$ mag has a $\sigma_{\star} = 100$ km s$^{-1}$. Plugging these values in Equation 11, we obtain $\theta_{\mathrm{E}} \sim 0''.2$. This is well below the current spatial resolution of our MUSE observations (see Table 1) and thus our measurements are not significantly biased by lensing.
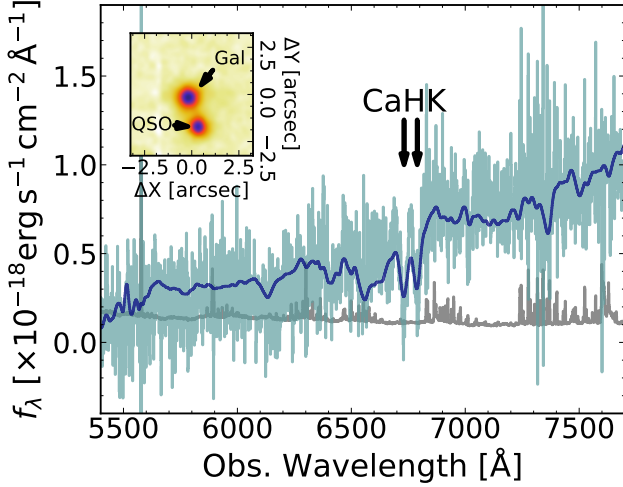
**Figure 12.** Spectrum of the foreground galaxy located $1.''57$ North North–East of the optical position of the quasar P323+12 (light blue). The elliptical galaxy template from Mannucci et al. (2001) redshifted to $z_{gal} = 0.711$ and rescaled to the flux observed in the Pan-STARRS $i$–band $i_{PS1, gal} = 23.29$ mag is shown as a dark blue line (see subsection 5.7 for details). The inset plots the location of the galaxy with respect to the quasar in the pseudo–broad–band image obtained by collapsing the MUSE cube between 8200Å and 9200Å.

Given the estimated size of the Einstein ring, the new AO system *GALACSI* on *MUSE* (Stuik et al. 2006) should be able to resolve it. Future high spatial resolution observations of this system will allow us to investigate the extended halo of a $z \sim 6.6$ quasar in unprecedented detail.

## 6. SUMMARY AND CONCLUSIONS

We conducted a sensitive search for extended Ly$\alpha$ emission around a sample of 31 $5.7 < z < 6.6$ quasars spanning absolute magnitudes from $M_{1450} = -22.5$ mag to $M_{1450} = -29.1$ mag. This ongoing *VLT*/MUSE effort represents the first statistical study of the circum–galactic medium of quasars during the epoch of reionization (see Figure 13). After subtracting the contribution of the central AGN, we unveil the presence of significant extended Ly$\alpha$ emission around 12 targets. The detected nebulosities extend out to $\sim 30$ kpc from the quasars and show a variety of morphologies and physical properties. The study of these systems reveal that:

(i) The flux–weighted centroid of the extended emission well aligns with the systemic redshift of the quasar host–galaxies traced by the [C II] 158 $\mu$m line with an average shift of $\langle \Delta V_{sys} \rangle = (69 \pm 36)$ km s$^{-1}$.

(ii) The luminosities of the halos appear to be independent of the amount of star formation in the host galaxy and of the UV luminosity of the central AGN.

(iii) The velocity dispersion of the gas in the halos is consistent with gravitational motion in dark matter halos of $M_{DM} \lesssim 10^{13}$ M$_\odot$ at $z \sim 6$.

(iv) For most of our objects, we do not find clear evidence of rotation or ordered motion. However, the extended emission around the quasar P231+20 shows indications of a rotational pattern.

(v) The surface brightness of the detected halos is consistent with the emission expected from optically thin clouds illuminated by the quasars. However, this requires high volume densities of the order $n_H \gtrsim 1$ cm$^{-3}$.

(vi) The average surface brightness profile of the halos is well fit by an exponential curve. After correcting for redshift dimming and scaling distances by the virial radius of a halo of $10^{12.5}$ M$_\odot$, we observe no strong evolution of the profile between $z \sim 3$ and $z \sim 6$. This is consistent with a scenario in which cold mode accretion is surely in place in massive halos hosting quasars at $z > 3$.

(vii) The four targets that have peculiarly small near zones ($R_p^{corr} \lesssim 3$ pMpc) do not show evidences for extended emission. This is consistent with a scenario where these quasars that have been shining for less than $\sim 10^5$ yr.

We can ask ourselves if the reservoirs of cool gas observed around the first quasars are sufficient to sustain the enormous star formation rates of the host galaxies (with depletion time of $t_{dep} \sim 10 - 100$ Myr) and fast growth of the central supermassive black holes. The little evolution in the characteristics of the extended Ly$\alpha$ halos observed between $z \sim 6$ and $z \sim 3$ suggests that the emitting clouds retain similar properties within this redshift range. In this idealized model and assuming a spherical distribution for the clouds, the total mass in cool gas can be calculated as:

$$M_{cool} = \pi R f_c N_H \frac{m_p}{X}. \quad (12)$$

Given that the extended emissions occur on scales of $10 - 30$ pkpc, we can roughly estimate $M_{cool} \gtrsim 10^9$ M$_\odot$ around the first quasars. In general, hydrodynamical cosmological simulation are necessary to follow the complex journey of this gas from the IGM down to the host galaxy. However, given the observed kinematics, we can assume that the angular momentum has little impact in the accretion process and consider the free–fall time ($t_{ff} = \sqrt{3\pi/32\,G\,\rho} \sim 50$ Myr) as the minimum time–scale over which gas inflows. This implies that, potentially, the rate of gas supply (of the order of $\dot{M}_{cool} \sim 10 - 100$ M$_\odot$ yr$^{-1}$) is compatible with the SFR estimated for the quasar host galaxies. Further investigations of
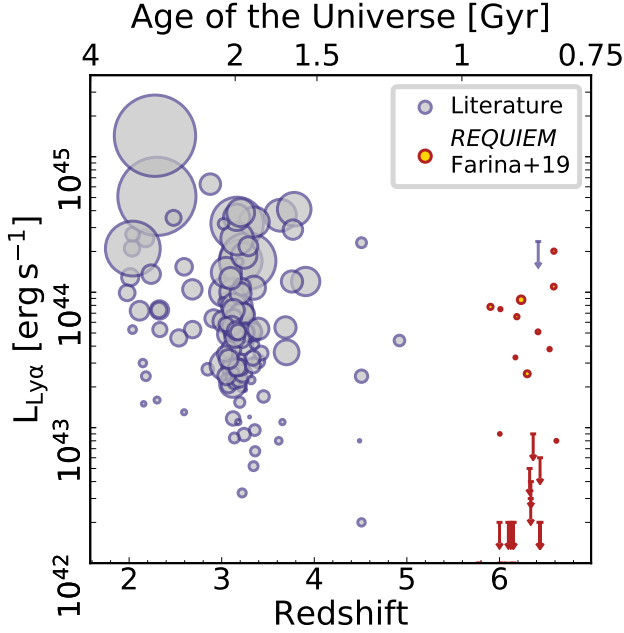
FARINA ET AL.



**Figure 13.** Redshift vs. total luminosity of all extended Lyα nebulae associated with QSOs known to date. Gray and orange points are data from the literature and from the *REQUIEM* survey, respectively. The size of the point is proportional to the area (in pkpc$^2$) covered by each halo. Downward arrows are 3–σ upper limits estimated integrating the nominal surface brightness limits over circular apertures with radius 20 pkpc. All values are uniformed to the concordance cosmology used in this paper. However, effects of different sensitivities and observing technique are not taken into account.

the detected nebulae are necessary to fully capture the physical status of the emitting material, however our *REQUIEM* survey suggest that the halos of the first quasars contain sufficient fuel to maintain the observed high–rate of gas consumption.

*Facilities:* ESO–*VLT*/MUSE & *LBT*/LUCI2+ARGOS
*Software:* This research made use of ASTROPY, a community–developed core PYTHON package for Astronomy (Astropy Collaboration et al. 2013) and of IRAF[11].

<center>REFERENCES</center>

Ageorges, N., Seifert, W., Jütte, M., et al. 2010, Proc. SPIE, 7735, 77351L

Alam, S. M. K., & Miralda-Escudé, J. 2002, ApJ, 568, 576

Atek, H., Kunth, D., Hayes, M., et al. 2008, A&A, 488, 491

Arrigoni Battaia, F., Yang, Y., Hennawi, J. F., et al. 2015, ApJ, 804, 26

Arrigoni Battaia, F., Hennawi, J. F., Prochaska, J. X., et al. 2015, ApJ, 809, 163

Arrigoni Battaia, F., Hennawi, J. F., Cantalupo, S., & Prochaska, J. X. 2016, ApJ, 829, 3

Arrigoni Battaia, F., Prochaska, J. X., Hennawi, J. F., et al. 2018, MNRAS, 473, 3907

Arrigoni Battaia, F., Chen, C.-C., Fumagalli, M., et al. 2018, A&A, 620, A202

Arrigoni Battaia, F., Hennawi, J. F., Prochaska, J. X., et al. 2019, MNRAS, 482, 3162

Arrigoni Battaia, F., Obreja, A., Prochaska, J. X., et al. 2019, arXiv e-prints, arXiv:1909.00829

Astropy Collaboration, Robitaille, T. P., Tollerud, E. J., et al. 2013, A&A, 558, A33

Bacon, R., Accardo, M., Adjali, L., et al. 2010, Proc. SPIE, 7735, 773508

Bacon, R., Brinchmann, J., Richard, J., et al. 2015, A&A, 575, A75

Bahcall, J. N., & Spitzer, L. 1969, ApJL, 156, L63

Balmaverde, B., Gilli, R., Mignoli, M., et al. 2017, A&A, 606, A23.

Bañados, E., Decarli, R., Walter, F., et al. 2015, ApJL, 805, L8

Bañados, E., Venemans, B. P., Morganson, E., et al. 2015, ApJ, 804, 118

Bañados, E., Venemans, B. P., Decarli, R., et al. 2016, ApJS, 227, 11

Bañados, E., Venemans, B. P., Mazzucchelli, C., et al. 2018, Nature, 553, 473

Bañados, E., Rauch, M., Decarli, R., et al. 2019, arXiv:1903.06186

Barnett, R., Warren, S. J., Banerji, M., et al. 2015, A&A, 575, A31

Beelen, A., Cox, P., Benford, D. J., et al. 2006, ApJ, 642, 694

Behroozi, P. S., Wechsler, R. H., & Conroy, C. 2013, ApJ, 770, 57

Bieri, R., Dubois, Y., Rosdahl, J., et al. 2017, MNRAS, 464, 1854

Bolton, J. S., & Haehnelt, M. G. 2007, MNRAS, 374, 493Willott2013

Borisova, E., Cantalupo, S., Lilly, S. J., et al. 2016, arXiv:1605.01422

Bouché, N., Murphy, M. T., Kacprzak, G. G., et al. 2013, Science, 341, 50

Bowen, D. V., Hennawi, J. F., Ménard, B., et al. 2006, ApJL, 645, L105

Brook, C. B., Governato, F., Roškar, R., et al. 2011, MNRAS, 415, 1051

Cai, Z., Fan, X., Yang, Y., et al. 2017, ApJ, 837, 71

Cai, Z., Hamden, E., Matuszewski, M., et al. 2018, ApJ, 861, L3

Cantalupo, S., Porciani, C., Lilly, S. J., et al. 2005, ApJ, 628, 61

Cantalupo, S., Arrigoni-Battaia, F., Prochaska, J. X., Hennawi, J. F., & Madau, P. 2014, Nature, 506, 63

Cantalupo, S. 2017, Gas Accretion onto Galaxies, 430, 195

Cantalupo, S., Pezzulli, G., Lilly, S. J., et al. 2019, MNRAS, 483, 5188

Cardelli, J. A., Clayton, G. C., & Mathis, J. S. 1989, ApJ, 345, 245

Carilli, C. L., Wang, R., Fan, X., et al. 2010, ApJ, 714, 834

Casey, C. M., Scoville, N. Z., Sanders, D. B., et al. 2014, ApJ, 796, 95

Cen, R., & Haiman, Z. 2000, ApJL, 542, L75

Chambers, K. C., Magnier, E. A., Metcalfe, N., et al. 2016, arXiv:1612.05560

Chen, D. N., Jing, Y. P., & Yoshikaw, K. 2003, ApJ, 597, 35

Chen, H.-W., & Tinker, J. L. 2008, ApJ, 687, 745

Chen, H.-W., Helsby, J. E., Gauthier, J.-R., et al. 2010, ApJ, 714, 1521

Chen, H.-W., Wild, V., Tinker, J. L., et al. 2010, ApJL, 724, L176

Chieregato, M., Miranda, M., & Jetzer, P. 2007, A&A, 474, 777

Christensen, L., Jahnke, K., Wisotzki, L., & Sánchez, S. F. 2006, A&A, 459, 717

Churchill, C. W., Nielsen, N. M., Kacprzak, G. G., et al. 2013, ApJL, 763, L42

Costa, T., Sijacki, D., Trenti, M., et al. 2014, MNRAS, 439, 2146

Connor, T., et al. 2019, submitted

Costa, T., Sijacki, D., Trenti, M., et al. 2014, MNRAS, 439, 2146

Costa, T., Sijacki, D., & Haehnelt, M. G. 2015, MNRAS, 448, L30

Cutri, R. M., Skrutskie, M. F., van Dyk, S., et al. 2003, The IRSA 2MASS All-Sky Point Source Catalog

Davies, F. B., Hennawi, J. F., & Eilers, A.-C. 2019, arXiv:1906.10130

Davies, F. B., Hennawi, J. F., & Eilers, A.-C. 2019, arXiv:1903.12346

Davis, S. W., & Laor, A. 2011, ApJ, 728, 98

Decarli, R., Dotti, M., Bañados, E., et al. 2019, arXiv e-prints, arXiv:1906.05308

Decarli, R., Walter, F., Venemans, B. P., et al. 2018, ApJ, 854, 97

Decarli, R., Walter, F., Venemans, B. P., et al. 2017, Nature, 545, 457

Decarli, R., Walter, F., Yang, Y., et al. 2012, ApJ, 756, 150

Decarli, R., Treves, A., & Falomo, R. 2009, MNRAS, 396, L31

De Rosa, G., Decarli, R., Walter, F., et al. 2011, ApJ, 739, 56

De Rosa, G., Venemans, B. P., Decarli, R., et al. 2014, ApJ, 790, 145

De Looze, I., Cormier, D., Lebouteiller, V., et al. 2014, A&A, 568, A62

Dekel, A., & Birnboim, Y. 2006, MNRAS, 368, 2

Dekel, A., Birnboim, Y., Engel, G., et al. 2009, Nature, 457, 451

Dekel, A., Lapiner, S., & Dubois, Y. 2019, arXiv e-prints, arXiv:1904.08431

Di Matteo, T., Khandai, N., DeGraf, C., et al. 2012, ApJL, 745, L29

Di Matteo, T., Croft, R. A. C., Feng, Y., Waters, D., & Wilkins, S. 2017, MNRAS, 467, 4243

Dijkstra, M., & Loeb, A. 2008, MNRAS, 386, Willott2013492

Dijkstra, M., & Loeb, A. 2009, MNRAS, 400, 1109

Drake, A. B., Farina, E. P., Neeleman, M., et al. 2019, arXiv e-prints, arXiv:1906.07197

Draine, B. T. 2011, Physics of the Interstellar and Intergalactic Medium by Bruce T. Draine. Princeton University Press

Dubois, Y., Pichon, C., Haehnelt, M., et al. 2012, MNRAS, 423, 3616

Dutton A. A., Macciò A. V., 2014, MNRAS, 441, 3359

Eilers, A.-C., Davies, F. B., Hennawi, J. F., et al. 2017, ApJ, 840, 24

Eilers, A.-C., Hennawi, J. F., & Davies, F. B. 2018, ApJ, 867, 30

Efstathiou, G., & Rees, M. J. 1988, MNRAS, 230, 5p

Eftekharzadeh, S., Myers, A. D., White, M., et al. 2015, MNRAS, 453, 2779

Faber, S. M., & Jackson, R. E. 1976, ApJ, 204, 668

Fall, S. M., & Efstathiou, G. 1980, MNRAS, 193, 189

Fan, X., Narayanan, V. K., Lupton, R. H., et al. 2001, AJ, 122, 2833.

Fan, X., Strauss, M. A., Schneider, D. P., et al. 2003, AJ, 125, 1649

Fan, X., Strauss, M. A., Becker, R. H., et al. 2006, AJ, 132, 117

Fanidakis, N., Macciò, A. V., Baugh, C. M., et al. 2013, MNRAS, 436, 315

Fasano, G., & Franceschini, A. 1987, MNRAS, 225, 155

Fardal, M. A., Katz, N., Gardner, J. P., et al. 2001, ApJ, 562, 605

Farina, E. P., Falomo, R., Decarli, R., et al. 2013, MNRAS, 429, 1267

Farina, E. P., Falomo, R., Scarpa, R., et al. 2014, MNRAS, 441, 886

Farina, E. P., Venemans, B. P., Decarli, R., et al. 2017, ApJ, 848, 78

Farina, E. P., Georgiev, I. Y., Decarli, R., et al. 2018, MNRAS, 476, 1835

Feng, Y., Di Matteo, T., Croft, R., & Khandai, N. 2014, MNRAS, 440, 1865

Fitzpatrick, E. L. 1999, PASP, 111, 63

Flewelling, H. A., Magnier, E. A., Chambers, K. C., et al. 2016, arXiv:1612.05243

Fumagalli, M., Prochaska, J. X., Kasen, D., et al. 2011, MNRAS, 418, 1796

Fumagalli, M., Cantalupo, S., Dekel, A., et al. 2016, MNRAS, 462, 1978

Furlanetto, S. R., Schaye, J., Springel, V., et al. 2005, ApJ, 622, 7

García-Vergara, C., Hennawi, J. F., Barrientos, L. F., & Rix, H.-W. 2017, ApJ, 848, 7

Gauthier, J.-R., Chen, H.-W., & Tinker, J. L. 2010, ApJ, 716, 1263

Georgiev, I. Y., Neumayer, N., Gässler, W., et al. 2019, MNRAS, 484, 3356

Ginolfi, M., Maiolino, R., Carniani, S., et al. 2018, MNRAS, 476, 2421

Goto, T., Utsumi, Y., Furusawa, H., Miyazaki, S., & Komiyama, Y. 2009, MNRAS, 400, 843

Goto, T., Utsumi, Y., Walsh, J. R., et al. 2012, MNRAS, 421, L77

Goto, T., Utsumi, Y., Kikuta, S., et al. 2017, MNRAS, 470, L117

Gould, A., & Weinberg, D. H. 1996, ApJ, 468, 462

Greene, J. E., Zakamska, N. L., & Smith, P. S. 2012, ApJ, 746, 86

Gronwall, C., Ciardullo, R., Hickey, T., et al. 2007, ApJ, 667, 79

Gunn, J. E., & Peterson, B. A. 1965, ApJ, 142, 1633

Habouzit, M., Volonteri, M., Somerville, R. S., et al. 2018, arXiv e-prints, arXiv:1810.11535

Haiman, Z., Spaans, M., & Quataert, E. 2000, ApJL, 537, L5

Haiman, Z., & Cen, R. 2001, The Physics of Galaxy Formation, 101

Haiman, Z., & Rees, M. J. 2001, ApJ, 556, 87

Hayes, M., Schaerer, D., Östlin, G., et al. 2011, ApJ, 730, 8

Hennawi, J. F., Prochaska, J. X., Burles, S., et al. 2006, ApJ, 651, 61

Heckman, T. M., Miley, G. K., Lehnert, M. D., & van Breugel, W. 1991, ApJ, 370, 78

Heckman, T. M., Lehnert, M. D., Miley, G. K., & van Breugel, W. 1991, ApJ, 381, 373

Hennawi, J. F., & Prochaska, J. X. 2007, ApJ, 655, 735

Hennawi, J. F., & Prochaska, J. X. 2013, ApJ, 766, 58

Hennawi, J. F., Prochaska, J. X., Cantalupo, S., & Arrigoni-Battaia, F. 2015, Science, 348, 779

Herenz, E. C., Wisotzki, L., Roth, M., et al. 2015, A&A, 576, A115

Hill J. M. & Salinari P., 2004, Proc. SPIE, 5489, 603

Hill J. M., Green R. F., Ashby D. S., et al. 2012, Proc. SPIE, 8444, 84441A

Hoyle, F. 1951, Problems of Cosmical Aerodynamics, 195

Husband, K., Bremer, M. N., Stanway, E. R., et al. 2015, MNRAS, 452, 2388

Izumi, T., Onoue, M., Shirakata, H., et al. 2018, PASJ, 70, 36.

Johnson, S. D., Chen, H.-W., & Mulchaey, J. S. 2015, MNRAS, 452, 2553

Jiang, L., McGreer, I. D., Fan, X., et al. 2016, ApJ, 833, 222.

Johnson, S. D., Chen, H.-W., & Mulchaey, J. S. 2015, MNRAS, 452, 2553

Kashikawa, N., Ishizaki, Y., Willott, C. J., et al. 2015, ApJ, 798, 28

Kellermann, K. I., Sramek, R., Schmidt, M., Shaffer, D. B., & Green, R. 1989, AJ, 98, 1195

Kennicutt, R. C., & Evans, N. J. 2012, ARA&A, 50, 531

Kereš, D., Katz, N., Weinberg, D. H., et al. 2005, MNRAS, 363, 2

Kereš, D., Katz, N., Fardal, M., et al. 2009, MNRAS, 395, 160

Kereš, D., & Hernquist, L. 2009, ApJL, 700, L1

Kim, Y., & Im, M. 2019, ApJ, 879, 117

Kunth, D., Mas-Hesse, J. M., Terlevich, E., et al. 1998, A&A, 334, 11

Lang, D., Hogg, D. W., Mierle, K., et al. 2010, AJ, 139, 1782

Lau, M. W., Prochaska, J. X., & Hennawi, J. F. 2016, ApJS, 226, 25

Lau, M. W., Prochaska, J. X., & Hennawi, J. F. 2018, ApJ, 857, 126

Leclercq, F., Bacon, R., Wisotzki, L., et al. 2017, A&A, 608, A8

Leibler, C. N., Cantalupo, S., Holden, B. P., et al. 2018, MNRAS, 480, 2094

Leipski, C., Meisenheimer, K., Walter, F., et al. 2014, ApJ, 785, 154

Li, Y., Hernquist, L., Robertson, B., et al. 2007, ApJ, 665, 187

Lusso, E., Worseck, G., Hennawi, J. F., et al. 2015, MNRAS, 449, 4204

Lusso, E., Fumagalli, M., Fossati, M., et al. 2019, MNRAS, 485, L62

Lyman, T. 1906, ApJ, 23, 181

MacLeod, C. L., Ivezić, Ž., Sesar, B., et al. 2012, ApJ, 753, 106

Madau, P., & Rees, M. J. 2000, ApJL, 542, L69

Mannucci, F., Basile, F., Poggianti, B. M., et al. 2001, MNRAS, 326, 745.

Martin, D. C., Chang, D., Matuszewski, M., et al. 2014, ApJ, 786, 106

Martin, D. C., Matuszewski, M., Morrissey, P., et al. 2015, Nature, 524, 192

Martin, D. C., O'Sullivan, D., Matuszewski, M., et al. 2019, Nature Astronomy, 356

Matsuoka, Y., Onoue, M., Kashikawa, N., et al. 2016, ApJ, 828, 26

Matsuoka, Y., Onoue, M., Kashikawa, N., et al. 2018, PASJ, 70, S35

Mayer, L., & Bonoli, S. 2019, Reports on Progress in Physics, 82, 016901

Mazzucchelli, C., Bañados, E., Venemans, B. P., et al. 2017, ApJ, 849, 91

Mazzucchelli, C., Decarli, R., Farina, E. P., et al. 2019, arXiv e-prints, arXiv:1907.02607

Mechtley, M., Windhorst, R. A., Ryan, R. E., et al. 2012, ApJL, 756, L38

Ménard, B., Scranton, R., Fukugita, M., & Richards, G. 2010, MNRAS, 405, 1025

Millikan, R. A. 1920, ApJ, 52, 47

Mo, H. J., Mao, S., & White, S. D. M. 1998, MNRAS, 295, 319

Momose, R., Goto, T., Utsumi, Y., et al. 2018, arXiv:1809.10916

Morselli, L., Mignoli, M., Gilli, R., et al. 2014, A&A, 568, A1

Mori, M., Umemura, M., & Ferrara, A. 2004, ApJL, 613, L97

Morrissey, P., Matuszewski, M., Martin, C., et al. 2012, Proc. SPIE, 844613

Morrissey, P., Matuszewski, M., Martin, D. C., et al. 2018, ApJ, 864, 93

Mortlock, D. J., Warren, S. J., Venemans, B. P., et al. 2011, Nature, 474, 616

Narayan, R., & Schneider, P. 1990, MNRAS, 243, 192

Navarro J. F., Frenk C. S., White S. D. M., 1997, ApJ, 490, 493

Neeleman, M., Bañados, E., Walter, F., et al. 2019, arXiv e-prints, arXiv:1907.02536

Nielsen, N. M., Churchill, C. W., Kacprzak, G. G., et al. 2013, ApJ, 776, 114

Nielsen, N. M., Churchill, C. W., & Kacprzak, G. G. 2013, ApJ, 776, 115

Nigoche-Netro, A., Aguerri, J. A. L., Lagos, P., et al. 2010, A&A, 516, A96

North, P. L., Courbin, F., Eigenbrod, A., & Chelouche, D. 2012, A&A, 542, A91

Osterbrock, D. E., & Ferland, G. J. 2006, Astrophysics of gaseous nebulae and active galactic nuclei

Ono, Y., Ouchi, M., Shimasaku, K., et al. 2010, ApJ, 724, 1524

Ota, K., Venemans, B. P., Taniguchi, Y., et al. 2018, ApJ, 856, 109

Oyarzún, G. A., Blanc, G. A., González, V., et al. 2017, ApJ, 843, 133

Peacock, J. A. 1999, Cosmological Physics

Peng, C. Y., Ho, L. C., Impey, C. D., & Rix, H.-W. 2010, AJ, 139, 2097

Peng, C. Y., Ho, L. C., Impey, C. D., & Rix, H.-W. 2011, Astrophysics Source Code Library, ascl:1104.010

Planck Collaboration, et al. 2014, A&A, 571, A16

Pons, E., McMahon, R. G., Simcoe, R. A., et al. 2019, MNRAS, 484, 5142

Prieto, J., Jimenez, R., Haiman, Z., et al. 2015, MNRAS, 452, 784

Prochaska, J. X., & Hennawi, J. F. 2009, ApJ, 690, 1558

Prochaska, J. X., Hennawi, J. F., Lee, K.-G., et al. 2013, ApJ, 776, 136

Prochaska, J. X., Hennawi, J. F., & Simcoe, R. A. 2013, ApJL, 762, L19

Prochaska, J. X., Lau, M. W., & Hennawi, J. F. 2014, ApJ, 796, 140

Reed, S. L., McMahon, R. G., Martini, P., et al. 2017, MNRAS, 468, 4702

Reed, S. L., Banerji, M., Becker, G. D., et al. 2019, arXiv:1901.07456

Rabien, S., Ageorges, N., Barl, L., et al. 2010, Proc. SPIE, 7736, 77360E-77360E-12

Rabien, S., Angel, R., Barl, L., et al. 2019, A&A, 621, A4

Rees, M. J. 1988, MNRAS, 231, 91p

Richards, G. T., Vanden Berk, D. E., Reichard, T. A., et al. 2002, AJ, 124, 1

Roche, N., Humphrey, A., & Binette, L. 2014, MNRAS, 443, 3795

Roussel, H., Wilson, C. D., Vigroux, L., et al. 2010, A&A, 518, L66

Sales, L. V., Navarro, J. F., Theuns, T., et al. 2012, MNRAS, 423, 1544

Salpeter, E. E. 1964, ApJ, 140, 796

Schlafly, E. F., & Finkbeiner, D. P. 2011, ApJ, 737, 103

Seifert, W., Appenzeller, I., Baumeister, H., et al. 2003, Proc. SPIE, 4841, 962

Sérsic, J. L. 1963, Boletin de la Asociacion Argentina de Astronomia La Plata Argentina, 6, 41

Shankar, F., Crocce, M., Miralda-Escudé, J., Fosalba, P., & Weinberg, D. H. 2010, ApJ, 718, 231

Shen, Y., Strauss, M. A., Oguri, M., et al. 2007, AJ, 133, 2222

Shen, Y., Brandt, W. N., Richards, G. T., et al. 2016, ApJ, 831, 7

Shen, Y., Wu, J., Jiang, L., et al. 2019, ApJ, 873, 35

Shao, Y., Wang, R., Carilli, C. L., et al. 2019, ApJ, 876, 99

Sijacki, D., Springel, V., & Haehnelt, M. G. 2009, MNRAS, 400, 100

Sobral, D., & Matthee, J. 2019, A&A, 623, A157

Soltan, A. 1982, MNRAS, 200, 115

Soto, K. T., Lilly, S. J., Bacon, R., Richard, J., & Conseil, S. 2016, MNRAS, 458, 3210

Steidel, C. C., Dickinson, M., & Persson, S. E. 1994, ApJL, 437, L75

Stewart, K. R., Maller, A. H., Oñorbe, J., et al. 2017, ApJ, 843, 47

Straatman, C. M. S., Labbé, I., Spitler, L. R., et al. 2014, ApJL, 783, L14

Straatman, C. M. S., Spitler, L. R., Quadri, R. F., et al. 2016, ApJ, 830, 51

Stuik, R., Bacon, R., Conzelmann, R., et al. 2006, NewAR, 49, 618

Tanaka, T., & Haiman, Z. 2009, ApJ, 696, 1798

Taniguchi, Y., & Shioya, Y. 2000, ApJL, 532, L13

Timlin, J. D., Ross, N. P., Richards, G. T., et al. 2018, ApJ, 859, 20

Tody, D. 1986, Proc. SPIE, 627, 733

Tody, D. 1993, Astronomical Data Analysis Software and Systems II, 52, 173

Tormen, G., Bouchet, F. R., & White, S. D. M. 1997, MNRAS, 286, 865

Tremonti, C. A., Moustakas, J., & Diamond-Stanic, A. M. 2007, ApJL, 663, L77

Tumlinson, J., Peeples, M. S., & Werk, J. K. 2017, ARA&A, 55, 389

van de Voort, F., Schaye, J., Altay, G., et al. 2012, MNRAS, 421, 2809

Venemans, B. P., McMahon, R. G., Walter, F., et al. 2012, ApJL, 751, L25

Venemans, B. P., Findlay, J. R., Sutherland, W. J., et al. 2013, ApJ, 779, 24

Venemans, B. P., Bañados, E., Decarli, R., et al. 2015, ApJL, 801, L11

Venemans, B. P., Walter, F., Zschaechner, L., et al. 2016, ApJ, 816, 37

Venemans, B. P., Decarli, R., Walter, F., et al. 2018, ApJ, 866, 159

Venemans, B., Neeleman, M., Walter, F., et al. 2019, arXiv e-prints , arXiv:1903.09202.

Verhamme, A., Schaerer, D., & Maselli, A. 2006, A&A, 460, 397

Villar-Martín, M. 2007, NewAR, 51, 194

Volonteri, M., & Rees, M. J. 2005, ApJ, 633, 624

Volonteri, M., & Rees, M. J. 2006, ApJ, 650, 669

Volonteri, M. 2010, A&A Rv, 18, 279

Volonteri, M., Natarajan, P., & Gültekin, K. 2011, ApJ, 737, 50

Volonteri, M. 2012, Science, 337, 544

Walter, F., Riechers, D., Cox, P., et al. 2009, Nature, 457, 699

Wang, R., Wagg, J., Carilli, C. L., et al. 2013, ApJ, 773, 44

Wang, R., Wu, X.-B., Neri, R., et al. 2016, ApJ, 830, 53

Wang, F., Yang, J., Fan, X., et al. 2018, arXiv e-prints, arXiv:1810.11926

Wang, F., Wang, R., Fan, X., et al. 2019, ApJ, 880, 2

Wang, R., Shao, Y., Carilli, C. L., et al. 2019, arXiv e-prints, arXiv:1904.07749

Weilbacher, P. M., Streicher, O., Urrutia, T., et al. 2012, Proc. SPIE, 8451, 84510B

Weilbacher, P. M., Streicher, O., Urrutia, T., et al. 2014, Astronomical Data Analysis Software and Systems XXIII, 485, 451

Werk, J. K., Prochaska, J. X., Cantalupo, S., et al. 2016, ApJ, 833, 54

White, S. D. M., & Rees, M. J. 1978, MNRAS, 183, 341

White, M., Myers, A. D., Ross, N. P., et al. 2012, MNRAS, 424, 933

Willott, C. J., Delorme, P., Omont, A., et al. 2007, AJ, 134, 2435

Willott, C. J., Delorme, P., Reylé, C., et al. 2010, AJ, 139, 906

Willott, C. J., Chet, S., Bergeron, J., & Hutchings, J. B. 2011, AJ, 142, 186

Willott, C. J., Omont, A., & Bergeron, J. 2013, ApJ, 770, 13

Willott, C. J., Bergeron, J., & Omont, A. 2015, ApJ, 801, 123

Willott, C. J., Bergeron, J., & Omont, A. 2017, ApJ, 850, 108

Wisotzki, L., Bacon, R., Blaizot, J., et al. 2016, A&A, 587, A98

Wu, X.-B., Wang, F., Fan, X., et al. 2015, Nature, 518, 512

Yang, J., Venemans, B., Wang, F., et al. 2019, ApJ, 880, 153

Yang, J., Wang, F., Fan, X., et al. 2019, AJ, 157, 236

Yang, Q., Shen, Y., Chen, Y.-C., et al. 2019, arXiv e-prints, arXiv:1904.10912

Yoo, J., & Miralda-Escudé, J. 2004, ApJL, 614, L25

Zeimann, G. R., White, R. L., Becker, R. H., et al. 2011, ApJ, 736, 57

APPENDIX

## A. ATLAS OF THE QUASARS PART OF THE *REQUIEM* SURVEY

In Figure 14 we show the RGB postage stamps of the quasar vicinity created by combining three $2000\,\mathrm{km\,s^{-1}}$ wide pseudo–narrow–band images: one located $16000\,\mathrm{km\,s^{-1}}$ blueward, one $5000\,\mathrm{km\,s^{-1}}$ redward, and one at the redshifted Ly$\alpha$ wavelength. The spectra of the quasars extracted over apertures with a radius two times larger than the seeing are also shown.
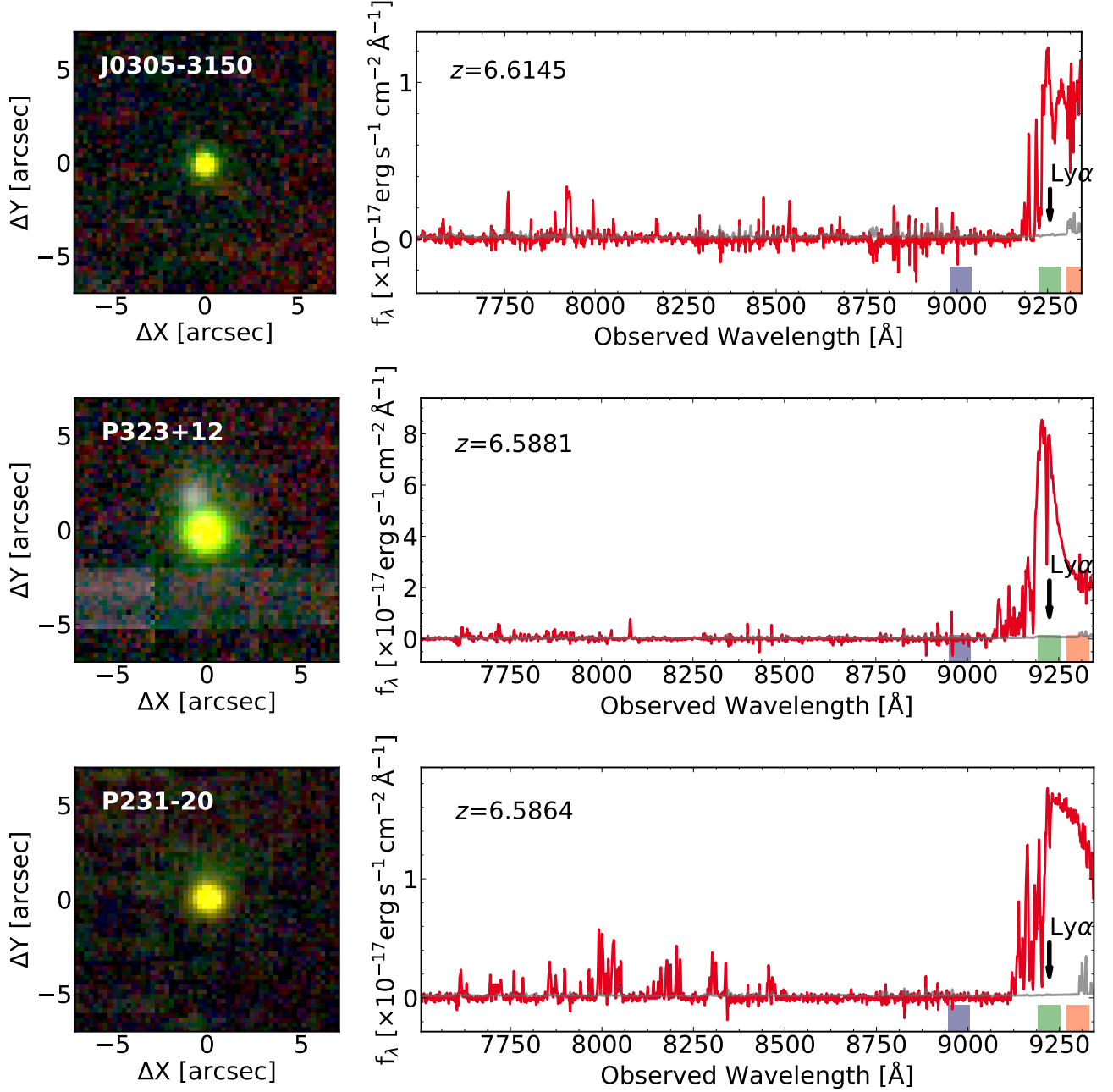


**Figure 14.** RGB images (left) and spectra (right) of the high–redshift quasars targeted in the *REQUIEM* survey (ordered by decreasing redshift). The wavelength ranges used to create the RGB images are highlighted with red, green, and blue boxes in the right panels. The wavelength of the Ly$\alpha$ line redshifted at $z_\mathrm{sys}$ is marked with a black arrow.
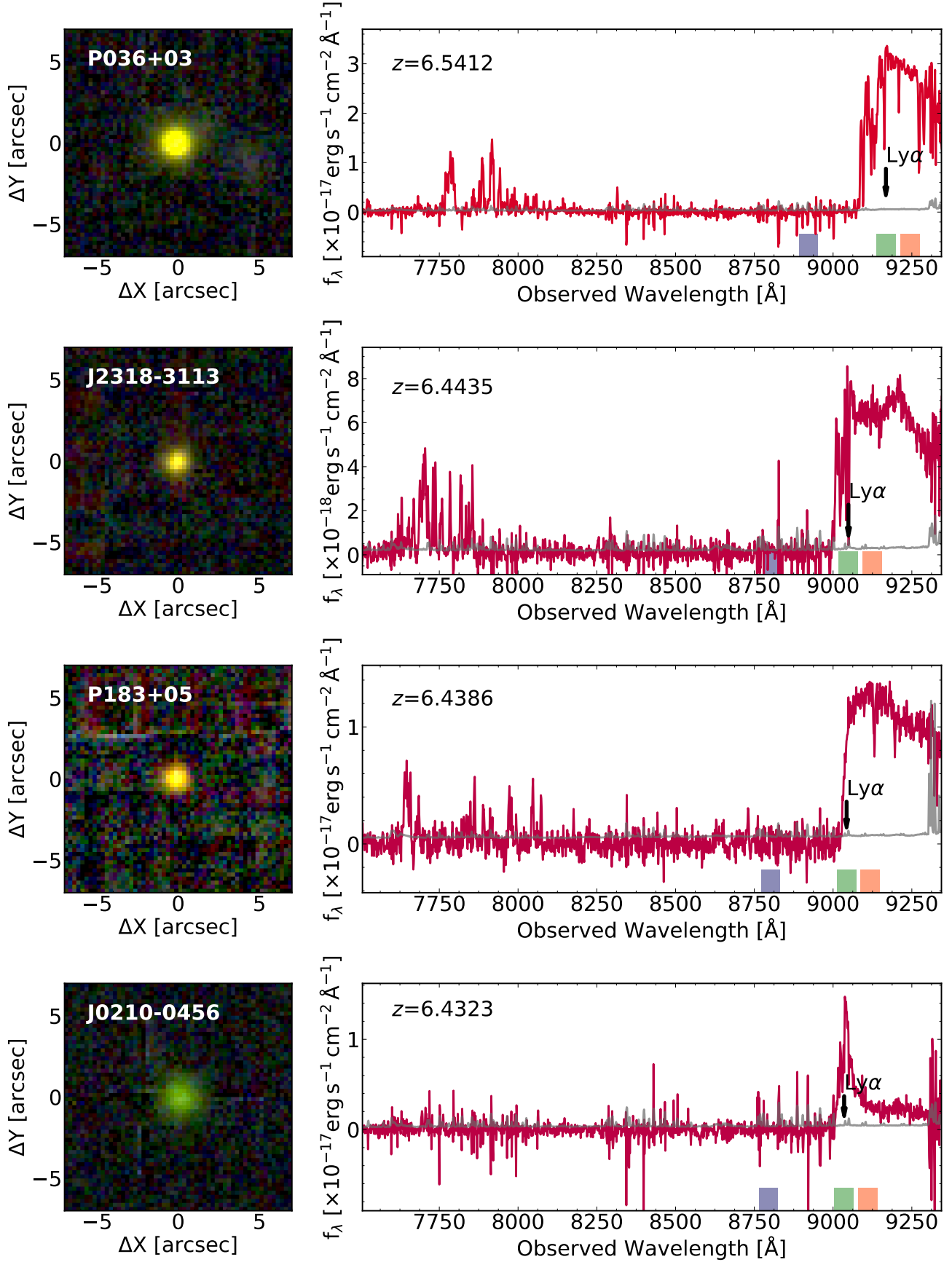
**Figure 14.** continued.
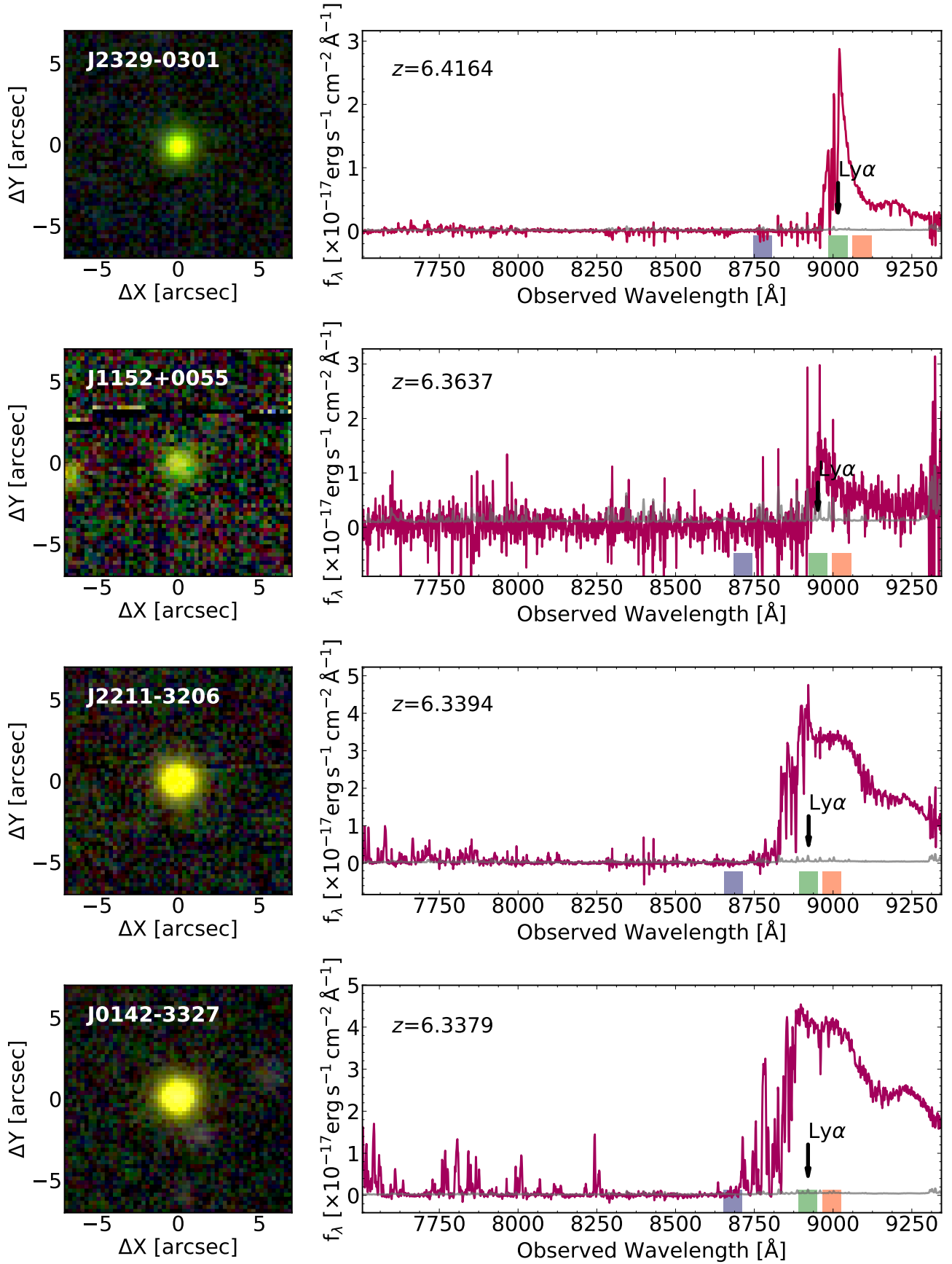
**Figure 14.** continued.
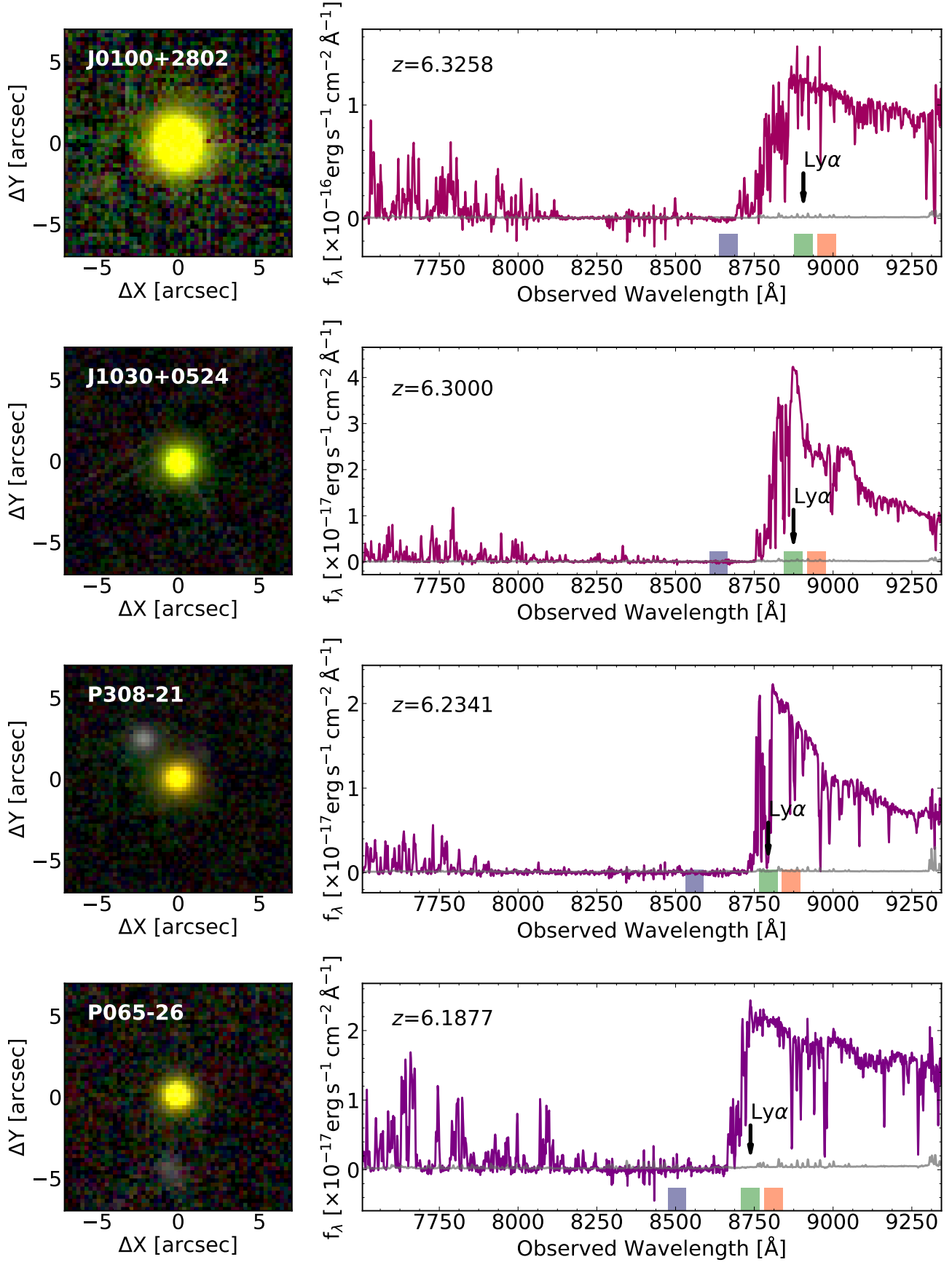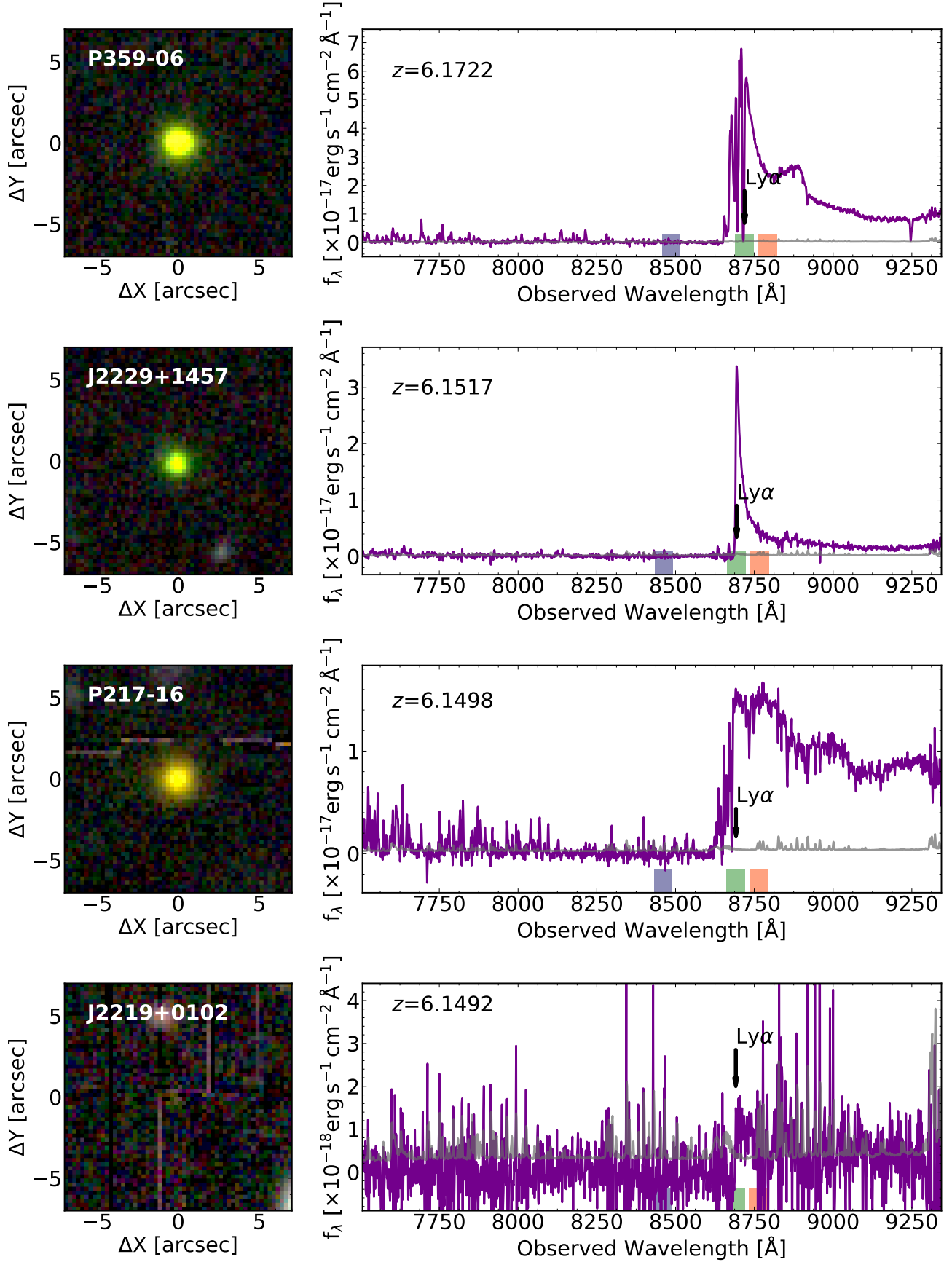
FARINA ET AL.



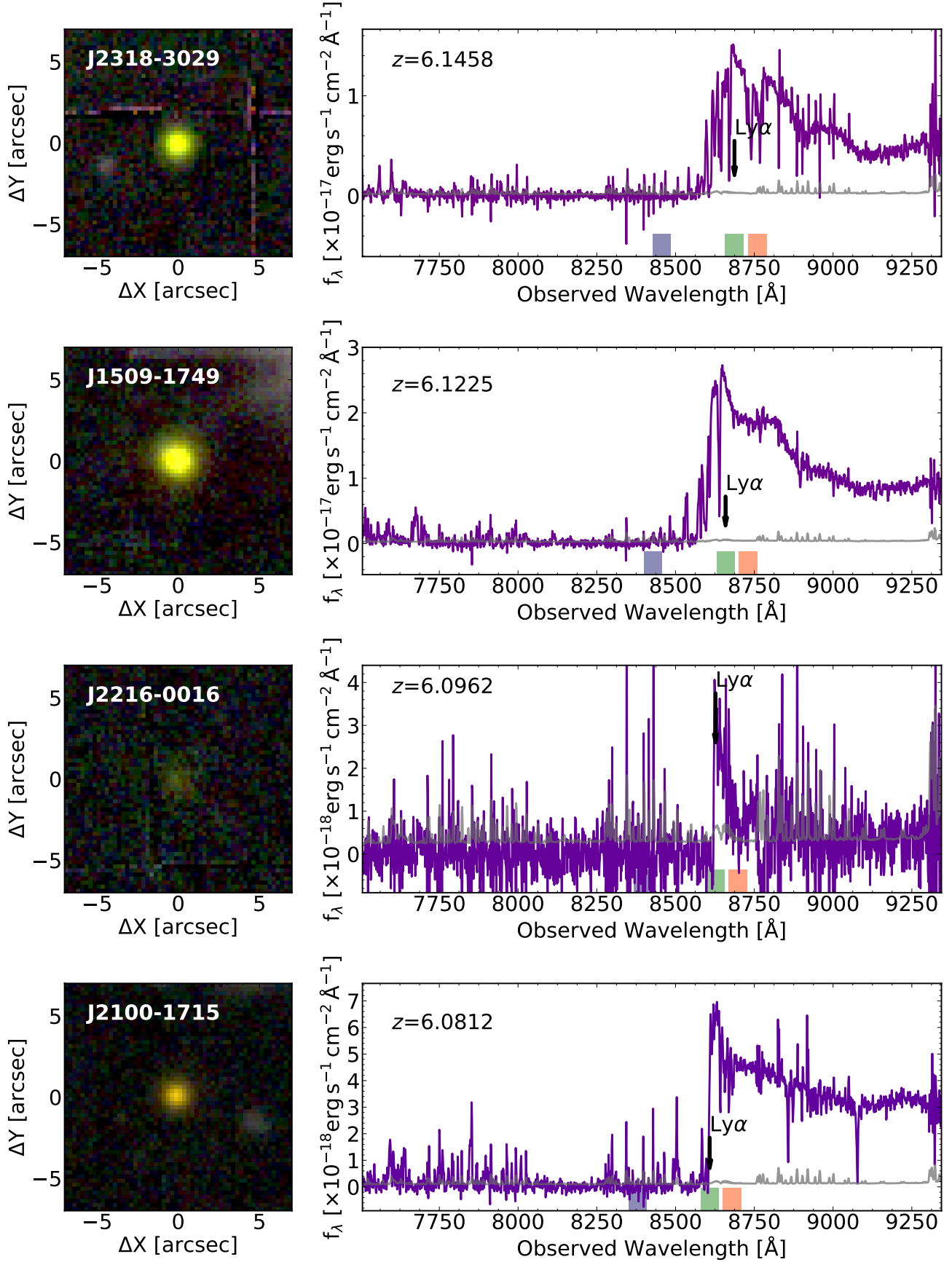**Figure 14.** continued.

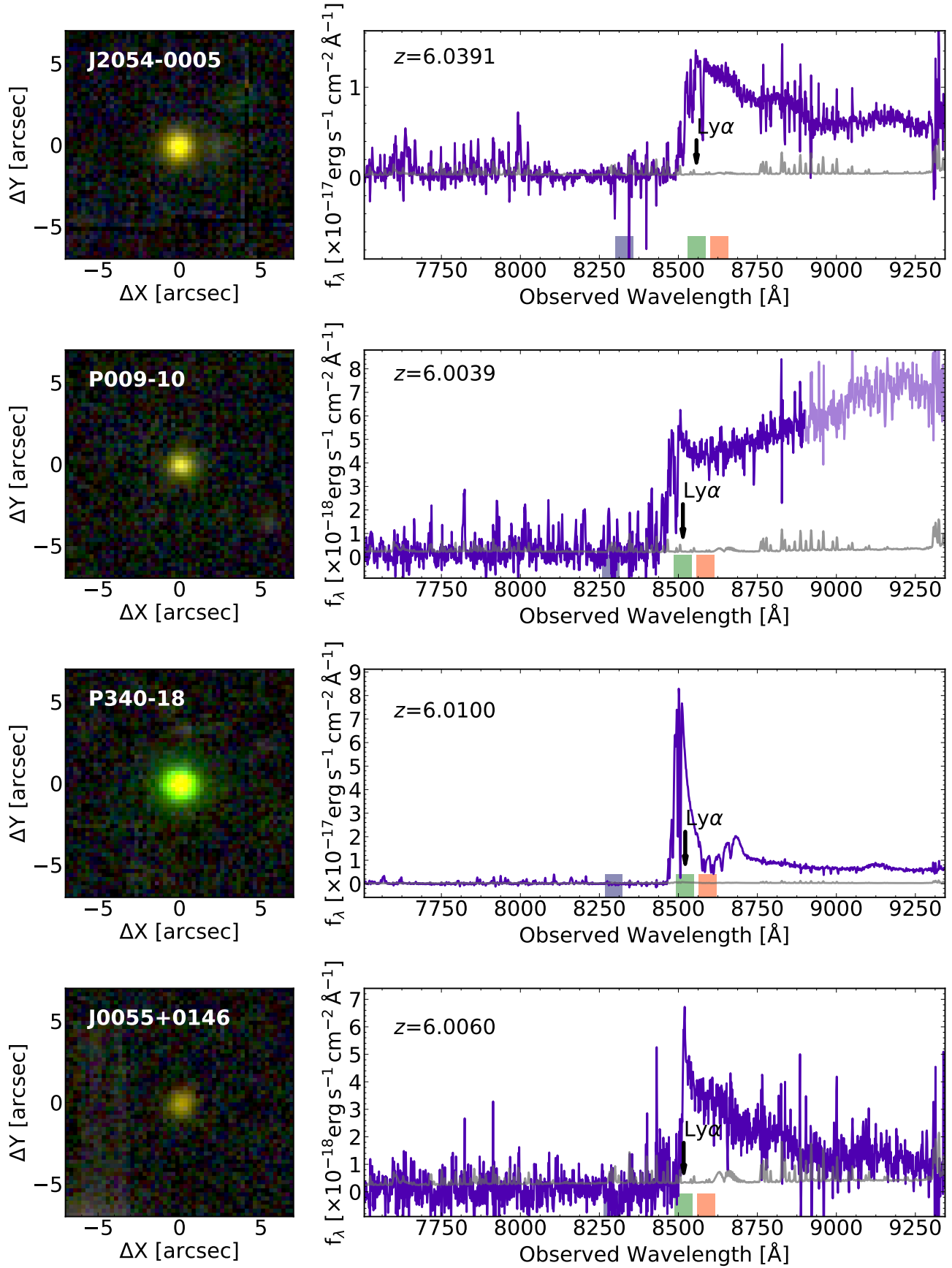**Figure 14.** continued.

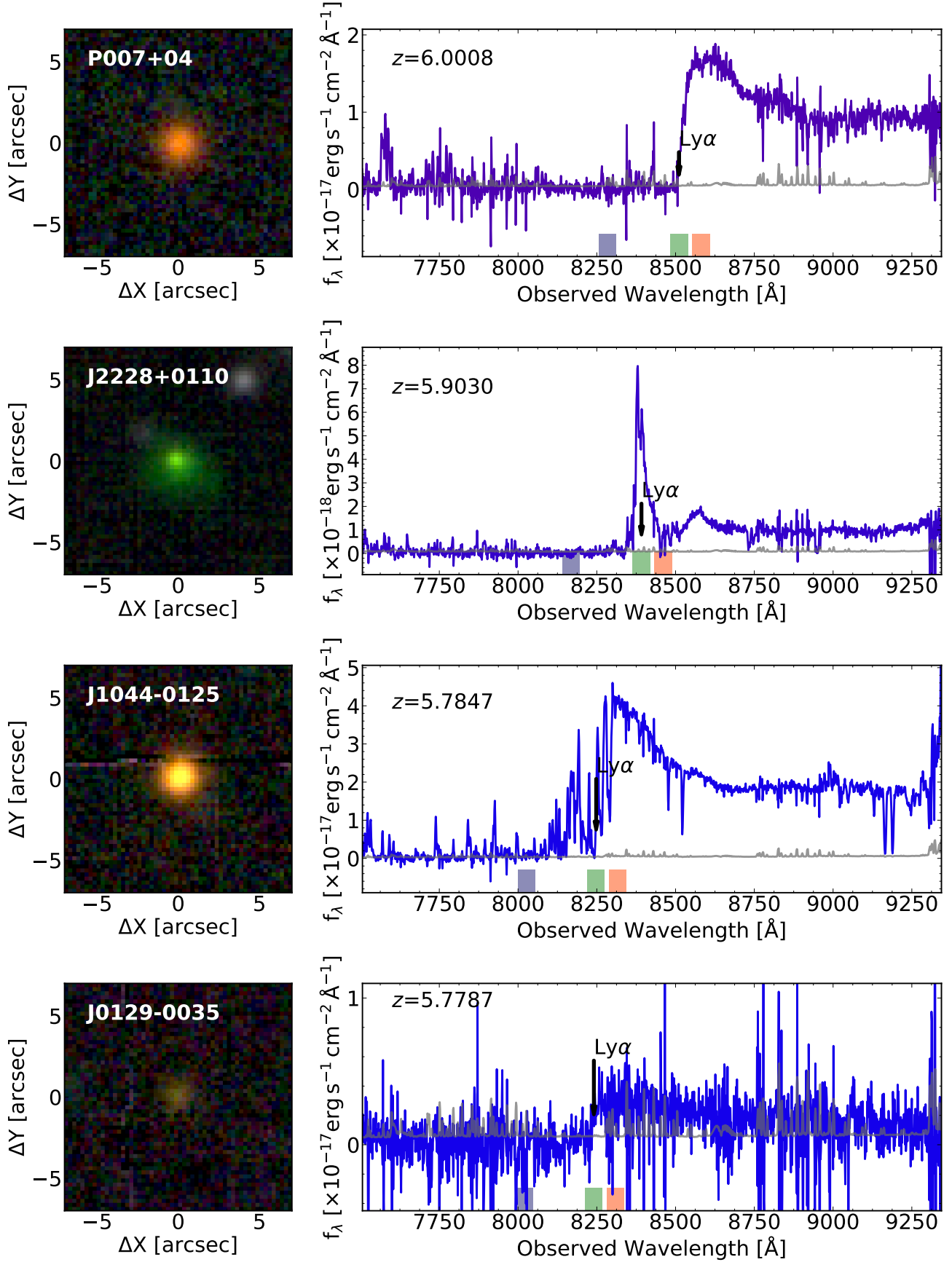Figure 14. continued.

**Figure 14.** continued.

**Figure 14.** continued.

## B. THE SPECTRUM OF P009−10

The spectrum of P009−10 plotted in Figure 14 shows a deviation from the typical blue slope of quasars at $\lambda > 8700$ Å. This behavior appears to be independent from the spectrophotometric star used for flux calibration and from the frames used to correct for flat field. We argue that this is most probably due to imperfect illumination correction due to the rapid variation of the sky conditions occurred during the observation of the target during the night of August 3rd, 2018. This is supported by the strong variation on the background in the red side of different MUSE IFUs. However, given that the Ly$\alpha$ line is redshifted at $\lambda \sim 8500$ Å, this has no impact on the current analysis.

## C. ANALYSIS OF THE *LBT*/LUCI2 + ARGOS IMAGES OF P323+12

High–resolution $Ks$–band images of the quasar P323+12 have been collected with the Large Binocular Telescope (*LBT*, Hill & Salinari 2004; Hill et al. 2012) high with the Advanced Rayleigh guided Ground layer adaptive Optics System (ARGOS; Rabien et al. 2010, 2019) coupled with LUCI 2 (i.e., *LBT* Utility Camera in the Infrared; Seifert et al. 2003; Ageorges et al. 2010). Data where collected on 25$^{\text{th}}$ October 2017 during an ARGOS commissioning run. The total time on targets was 660 s, divided in 263 individual 2.51 s exposures. The data reduction has been performed with standard IRAF routines following the procedure described in Farina et al. (2018) and Georgiev et al. (2019). We registered the image to the WCS using the ASTROMETRY.NET software (Lang et al. 2010). The absolute flux calibration was achieved by matching sources with the 2MASS catalogue (Cutri et al. 2003) and considering a Vega to AB conversion in the $K_s$–band of $m_{AB} - m_{Vega} = 1.85$ mag. Uncertainty in the zeropoint is of the order of 0.1 mag. During the observations, the DIMM seeing was $1''.34$ in the optical. The three green light (532 nm) lasers focused at 12 km used by ARGOS to correct for the ground layer turbulence, allowed us to enhance the $Ks$–band image quality to $0''.27$ (FWHM of an unresolved source) of the entire LUCI 2 field–of–view. The 5–$\sigma$ detection limit for a point source (estimated from the RMS of the sky counts integrated over the radius of an unresolved source) is $Ks_{\text{lim}} = 23.9$ mag[12].

We exploit this data to look for the possible presence of multiple lensed images of the quasar generated by the presence of the $z = 0.711$ elliptical galaxy located $1''.6$ NNE from the quasar (see subsection 5.7). First, we construct a spatially variable PSF model and we evaluated it at the quasar location (for further details see Farina et al. 2018; Georgiev et al. 2019). Then, we use this model to subtract both the emission from both the quasar and the close–by galaxy using the GALFIT v3.0.5 package (Peng et al. 2010, 2011, see Figure 15). The galaxy emission is well represented by a Sérsic profile (Sérsic 1963) with magnitude $Ks_{\text{gal}} = (20.26 \pm 0.16)$ mag, effective radius $R_e = (1.1 \pm 0.3)$ arcsec, and Sérsic index $n = (4.9 \pm 2.1)$. The quasar is unresolved, with apparent magnitude $Ks_{\text{QSO}} = (19.33 \pm 0.11)$ mag (see Figure 15). This implies that the host–galaxy is either compact (with radius $< 1.5$ pkpc) or its emission is below a surface brightness of $\mu_{Ks,\text{host}} > 22.7$ mag arcsec$^{-1}$ 5–$\sigma$ limit over a 1 arcsec$^2$ aperture). These limits are slightly looser, but consistent with those obtained by Mechtley et al. (2012) on the host galaxy of the $z = 6.42$ quasar J1148+5251.

In the residual image we do not detect any source in the close proximity of the galaxy (down to a 2–$\sigma$ surface brightness limit of $\mu_{Ks,\text{lim}} > 23.7$ mag arcsec$^{-1}$ over an aperture of 1 arcsec$^2$) that could be interpreted as multiple images of the quasar. This supports our simple model presented in subsection 5.7 where we showed that the Einstein ring is expected to be smaller than the separation between the quasar and the galaxy (i.e., $< 1''.6$).

---

[12] The final image in FITS format is available at: https://github.com/EmAstro/LBT_ARGOS.
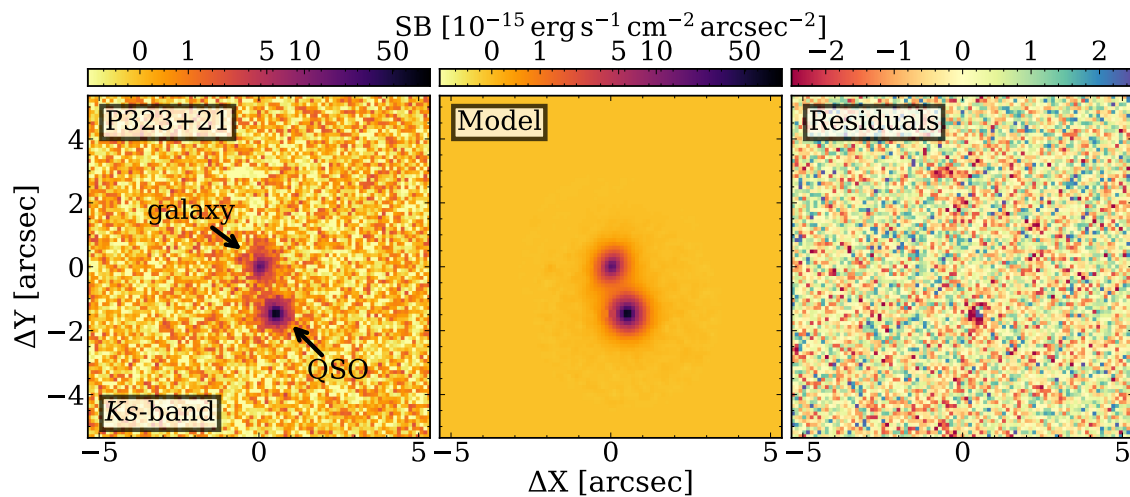
**Figure 15.** Results from the modelling of the quasar and close–by galaxy on the $Ks$–band images obtained with *LBT*/LUCI 2+ARGOS. Different panels show, from left to right: zoom–in on the $10'' \times 10''$ region centered on the galaxy; model of the quasar and galaxy emission; residuals after model subtraction (see Appendix C for details). In all panels, North is up and West is right.